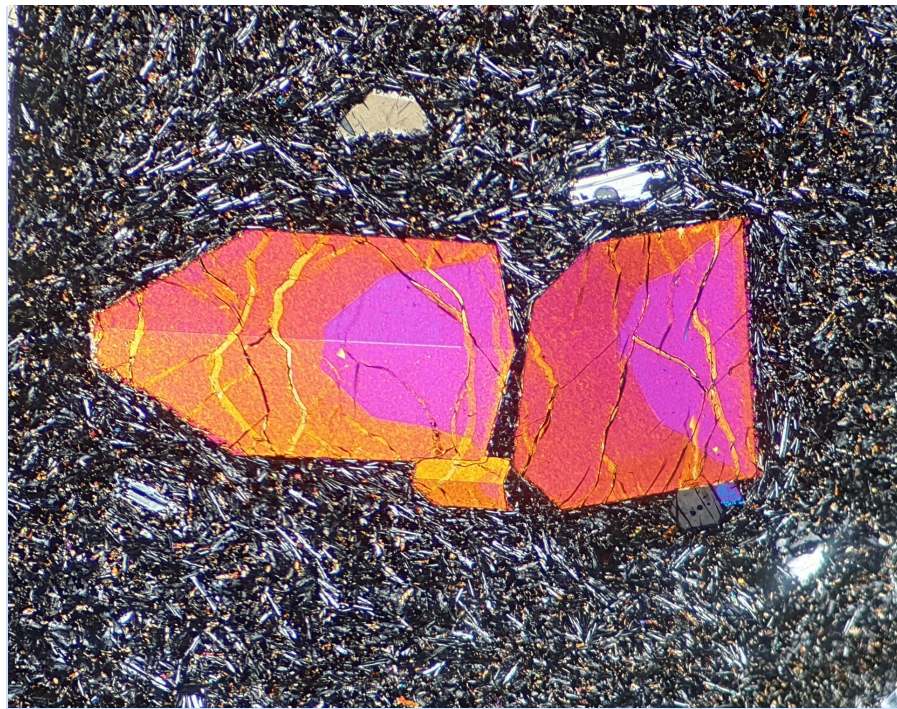


Studying magmatic systems through chemical analyses on clinopyroxene — a look into the history of the Teno ankaramites, Tenerife

Vendela Haag

Dissertations in Geology at Lund University,
Master's thesis, no 595
(45 hp/ECTS credits)



Department of Geology
Lund University
2020

Studying magmatic systems through chemical analyses on clinopyroxene — a look into the history of the Teno ankaramites, Tenerife

Master's thesis
Vendela Haag

Department of Geology
Lund University
2020

Contents

1 Introduction	9
2 Background	9
2.1 The Canary archipelago	9
2.1.1. Growth stages	10
2.1.2 Mass wasting events	10
2.1.3 Tenerife	10
2.1.4 Ankaramites and the Teno massif	11
2.2 Trace elements and elemental distribution	12
2.2.1 Trace element distribution	12
2.2.2 Trace element ratios and fractionation	13
2.3 Clinopyroxene as a recorder of magmatic processes	13
2.3.1 Major and minor elements in clinopyroxene	13
2.3.2 Trace elements in clinopyroxene—variation in partition coefficients	14
2.3.3 Literature values for partition coefficients (D) for clinopyroxene	14
2.3.4 Zoning types	14
2.3.5 Implications and previous studies regarding zoning	16
2.3.6 Magma recharge and mixing	17
3 Methods.....	18
3.1 Scanning electron microscope (SEM)	18
3.1.1 SEM: Sample preparation	18
3.2 Laser ablation inductively coupled plasma mass spectrometry (LA-ICP-MS)	18
3.2.1 LA-ICP-MS: Sample preparation	18
3.2.2 Evaluating LA-ICP-MS results	18
3.2.3 Chosen partition coefficients for evaluation	19
4 Results.....	19
4.1 Optical observations	19
4.2 Scanning electron microscopy (SEM-EDS)	21
4.2.1 Sector zoned crystals: A1a and A2b	22
4.2.2 Concentrically zoned crystals: A1b and A2a	22
4.2.3 Rims	22
4.2.4 Comparison of chemical compositions and substitution relationships	29
4.2.5 Inclusions and matrix crystals	30
4.3 Electron backscatter diffraction analyses (EBSD)	30
4.4 Laser ablation inductively coupled plasma mass spectrometry (LA-ICP-MS)	30
4.4.1 Sector zoned crystals: A1a and A2b	30
4.4.1.1 Relative partition coefficients between sectors	31
4.4.2 Concentrically zoned crystals: A1b and A2a	32
4.4.3 Rims	34
4.4.4 Liquid composition: Ratios and trends	34
4.4.5 Cr spikes	35
4.4.5.1 Sector zoned crystals: A1a and A2b	35
4.4.5.2 Concentrically zoned crystals: A1b and A2a	37
4.4.5.3 Cr spikes and liquid composition	37
4.4.5.4 Cr spikes and other elements	37
5 Discussion.....	39
5.1 General chemistry and substitution relationships	39
5.2 The chemical and crystallographic nature of the sector zoning	39
5.2.1 Differences in partition coefficients between sectors	41
5.3 Character of the concentric zoning and clues to the growth history	41
5.3.1 Origin of the A1b core	42
5.4 Chemical imprints from eruption and mass wasting events	43
5.5 Link between Cr spikes, magma recharge and the eruption event	44

Cover Picture: Three sector zoned clinopyroxene crystals in a matrix of plagioclase needles and flow texture.
Photo: Vendela Haag.

Contents, continuation

5.6 Plagioclase compositions inferring a Na-Ca substitution trend	46
5.7 Notes on growth rates	46
5.8 Chemical trends and melt evolution	46
5.9 Interpretations regarding magmatic history and open system processes	47
5.9.1 Origin and growth histories of the clinopyroxene crystals	47
5.9.2 Eruption event and rim formation	48
6 Conclusions	49
6.1 Recommended future research	50
7 Acknowledgments	50
8 References	50
Appendix A	53
Appendix B	55
Appendix C	56
Appendix D	60
Appendix E	62
Appendix F	91

Studying magmatic systems through chemical analyses on clinopyroxene — a look into the history of the Teno ankaramites, Tenerife

VENDELA HAAG

Haag, V., 2020: Studying magmatic systems through chemical analyses on clinopyroxene — a look into the history of the Teno ankaramites, Tenerife. *Dissertations in Geology at Lund University*, No. 595, 96 pp. 45 hp (45 ECTS credits).

Abstract: Clinopyroxenes have the ability to crystallize over and respond to a large range of temperatures, pressures and chemical compositions, and thus, they are ideal for studies regarding the history of magmatic systems. In this thesis, the chemistry and zoning of four clinopyroxene crystals from an ankaramite sample from the Teno massif, Tenerife, were analysed. The ankaramites in Teno massif were, according to previous studies, erupted following mass wasting events, and at least two mass wasting events have occurred in the history of the massif. The aim of the thesis was to link the chemistry and crystal features to possible processes affecting the magmatic system during their growth, to evaluate possible open system processes and eruption triggers related to the mass wasting events, and to gain an understanding for how clinopyroxenes can be used to study magmatic systems. The crystals were analysed using optical microscopy, scanning electron microscopy (SEM), and laser ablation inductively coupled plasma mass spectrometry (LA-ICP-MS).

The results show that the four clinopyroxene crystals can be divided into two groups: sector zoned crystals displaying different compositions in different faces of the crystal, and concentric zoned crystals. The widely different crystal features, with the concentric zoned crystals being inferred to have experienced a longer and more complex growth history, indicate that they belong to different generations or origins, indicating that magma mixing occurred in the system. On the other hand, the rims of all four crystals share enough similarities to be interpreted to have grown simultaneously, reflecting the eruption event. Furthermore, a band of deviant chemical composition is present inside the rim of all crystals, perhaps related to the mass wasting event and eruption trigger. Open system processes are inferred by Cr spikes in all four crystals, interpreted to represent events of recharge of primitive magma. These Cr spikes are located in the rims of the sector zoned crystals and in the interior of the concentric zoned crystals. If the mass wasting event is to be considered the eruption trigger, the location of the Cr spikes close to the rim in the sector zoned crystals points to the possibility that the magma recharge and the mass wasting event are related, most likely that the magma recharge destabilized the system and caused the mass wasting event to occur. However, further work needs to be done to confirm this hypothesis.

To acquire a better understanding for the magmatic history of these clinopyroxene crystals and the magmatic system in which they grew, more chemical analyses have to be made on a larger number of samples; preferably sampled systematically in order to know which ankaramite formation is being studied. Furthermore, geothermobarometry should be carried out in order to constrain the crystallization depth and temperature of the crystals and determine their respective origin.

Keywords: clinopyroxene, sector zoning, concentric zoning, mass wasting, magma recharge

Supervisor: Anders Scherstén

Subject: Bedrock geology

Vendela Haag, Department of Geology, Lund University, Sölvegatan 12, SE-223 62 Lund, Sweden. E-mail: vendela.haag@hotmail.com

Studie av magmatiska system genom kemiska analyser på klinopyroxen — en inblick i Tenoankaramiternas historia, Teneriffa

VENDELA HAAG

Haag, V., 2020: Studie av magmatiska system genom kemiska analyser på klinopyroxen — en inblick i Tenoankaramiternas historia, Teneriffa, Nr. 595, 96 sid. 45 hp.

Sammanfattning: Klinopyroxen har förmågan att kristallisera över ett stort intervall av temperatur, tryck och kemisk sammansättning; därför är de optimala för att studera historien för ett magmatiskt system. I den här uppsatsen analyserades fyra klinopyroxenkristaller i en ankaramit med fokus på kemi och zonerings. Ankaramitprovet härstammar från Tenomassivet, Teneriffa, och bildades troligtvis i ett utbrott som skedde till följd av massrörelse. Syftet med uppsatsen var att koppla kemi och zonerings till möjliga processer som kan ha påverkat det magmatiska systemet under klinopyroxenkristallernas kristallisation, att utvärdera eventuella processer relaterade till ett öppet system, utbrottstriggers och massrörelse, samt att få en förståelse för hur klinopyroxen kan användas för att studera magmatiska system. Kristallerna analyserades med optiskt mikroskop, svepelektronmikroskop (SEM) och laserablation-induktivt kopplad plasma-masspektrometri (LA-ICP-MS).

Resultaten visar att de fyra klinopyroxenkristallerna kan delas in i två grupper: sektorzonerade kristaller med olika kemisk sammansättning i olika facetter av kristallen, och koncentriskt zonerade kristaller. De olika zonerings typerna, samt hypotesen att de koncentriskt zonerade kristallerna har genomgått en längre och mer komplex kristallisation, indikerar att de tillhör olika generationer eller olika ursprung. Detta, i sin tur, indikerar att magmamixing har förekommit i systemet. Kristallernas kanter, däremot, är så pass lika att de troligtvis kristalliserade samtidigt och representerar själva utbrottet. Vidare, ett band med avvikande kemisk sammansättning var identifierat innanför kanten i alla kristaller, möjligen relaterat till massrörelserna och utbrottstriggern. Cr-spikar observerades i alla fyra kristaller och indikerar ett öppet system, då dessa troligen representerar tillskott av ny primitiv magma i systemet. Cr-spikarna observerades nära kanterna i de sektorzonerade kristallerna och närmre mitten i de koncentriskt zonerade kristallerna. Om massrörelsen betraktas som utbrottstriggern kan Cr-spikarna nära kanterna i de sektorzonerade kristallerna indikera en koppling mellan massrörelsen och tillskottet av primitiv magma. I detta fall är det mest troligt att tillskottet av magma destabiliserade systemet och orsakade massrörelsen. Det krävs dock mer analyser för att bekräfta denna hypotes.

För att få en bättre förståelse för kristallisationshistorien för dessa klinopyroxenkristaller och det magmatiska system som de kristalliserade i behöver fler kemiska analyser genomföras på en större mängd prov; gärna systematiskt provtagna så att det är säkert vilken ankaramitformation som studeras. Vidare skulle geotermobarometri kunna användas för att avgöra kristallernas kristallisationsdjup- och temperatur och därmed avgöra deras respektive ursprung.

Nyckelord: klinopyroxen, sektorzonering, koncentrisk zonerings, massrörelser, magmatillskott

Handledare: Anders Scherstén

Ämnesinriktning: Berggrundsgeologi

Vendela Haag, Geologiska institutionen, Lunds Universitet, Sölvegatan 12, 223 62 Lund, Sverige. E-post: vendela.haag@hotmail.com

1 Introduction

During the evolution of a magma body, large-scale events can be recorded as small-scale signatures in its chemistry. These signatures can subsequently be analysed and used to gain insight into the history of the system, and what factors controlled the magma body up until complete crystallization. Volcanic rocks can be the ideal target for these analyses due to the possible presence of phenocrysts that slowly grow and record events over an extended period of time. Additionally, when it comes to volcanology, these kinds of studies are particularly interesting because they involve the question of what triggered the eruption. For instance, previous studies have identified Cr spikes in the rims of clinopyroxene phenocrysts and linked them to events of magma recharge, which in turn can give information about the eruption trigger (Ubide et al., 2019). Clinopyroxene crystallise over a wide range of temperatures and pressures in magmatic systems (Putirka, 2008) and incorporates a number of indicative trace elements, which makes it a well suited mineral for constraining the history of the system.

The Teno massif on Tenerife, Canary Islands, has been affected by at least two major mass wasting events and subsequent ankaramite depositions. In this thesis, a sample from these ankaramites was used. The ankaramites are perceived to represent deep seated magmas in which crystals had time to grow, and is evidently characterized by large clinopyroxene phenocrysts suitable for this kind of study (Longpré et al., 2009)

The aim of this thesis is to analyse the zoning and chemistry of these clinopyroxene crystals and to gain insight into the processes affecting the system during their growth. Special interest is taken to potential signs of open system processes and possible eruption triggers, and the following questions will be addressed:

- *What is the type of zoning in these crystals, and what can the nature of the zoning convey about the system?*
- *Did the two mass wasting events create any impact on the chemistry of the clinopyroxene crystals?*
- *Are there signs of open system processes, specifically Cr spikes, and can they be related to the eruption trigger?*

The questions will be addressed by analysing the clinopyroxene crystals using optical microscopy, scanning electron microscopy and laser ablation inductively coupled plasma mass spectrometry.

2 Background

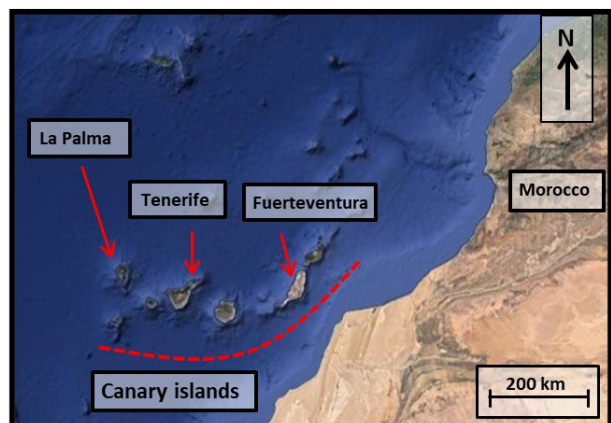
2.1 The Canary archipelago

Located 100 km from the western coast of Africa (fig 1), the Canary Islands archipelago consists of 7 major volcanic islands: Lanzarote, Fuerteventura, Gran Canaria, Tenerife, La Gomera, La Palma and El Hierro, with Fuerteventura being the oldest and La Palma and El Hierro the youngest. The islands, stretching from east to west over approximately 500 km, make up an

archipelago that formed over ca 60 million years (Carracedo & Troll, 2016).

A number of models have been proposed to explain the extensive volcanism resulting in the formation of this archipelago, including lithospheric fractures propagating from the Atlas fault (Anguita & Hernán, 1975, 2000), the “uplifted block hypothesis” (Araña & Ortiz, 1991) and the mantle-plume model. Additionally, Anguita & Hernán (2000) proposed a so called unifying model, taking into account all these three models. They suggested that the thermal anomaly is produced by a residue of an old plume, and that fractures formed due to extensional processes related to the Atlas Mountains brought magma up to the surface. However, the fractures have never been located (Carracedo & Troll, 2016); hence, the most favoured model is the mantle-plume model (Montelli, 2003; Wilson, 1963). The mantle-plume model suggests the presence of a thermal mantle anomaly, i.e. a hot spot, caused by a mantle plume bringing hot material from great depths. The thermal anomaly gives rise to localized volcanic activity and the creation of a volcanic island. As the tectonic plate moves over the hot spot region, the island is eventually cut off from the volcanism and a new island starts to form. However, in the case of the Canary Islands the older islands can still be volcanically active due to edge-driven mantle convection (King, 2007), moving hot plume material to the east and the northeast, reaching the older part of the Canary Islands.

Over time, as the tectonic plate continues to move in relation to the hot spot, several islands are formed in a line, creating an archipelago of differently aged islands. The Canary Islands, similar to the Hawaiian Islands, present meaningful opportunities to study the different stages of the formation of these islands. However, while the oldest Hawaiian island studied is only 5.1 million years old, Fuerteventura was formed more than 20 million years ago. This striking age difference is related to the subsidence rates for the islands. When an island cools its density increases which, in tandem with the fact that the island moves away from the hot spot swell, causes the island to sink



Imagery ©2020 NASA, TerraMetrics, Map data ©2020

Fig 1: The Canary Islands are located to the west of Africa, and consist of 7 major volcanic islands. Fuerteventura is the oldest island and La Palma and El Hierro (south of La Palma) are the youngest. Tenerife is located in the middle of this archipelago.

and eventually subside below sea level. This appears to happen at a faster rate in the Hawaiian archipelago than in the Canarian archipelago due to a number of factors. The oceanic crust beneath the Canary Islands is older than that below the Hawaiian Islands (>170 Ma vs. 95 Ma), and is therefore more rigid and thicker than the Hawaiian crust due to lower temperature and deposition of sediment from the African coast. It is also possible that the continental margin of Africa acts as a buoyancy anchor due to the lower density of the continental crust (Carracedo & Troll, 2016). Because of these reasons, the islands of the Canarian archipelago stays emerged for a longer period of time than the Hawaiian Islands, and are subjected to above sea level erosion for a longer time. The magma is also further differentiated due to longer lasting active volcanism, resulting in an abundance of more evolved magmas, e.g. phonolites, (e.g. Carracedo & Troll, 2016; Schmincke, 1969; Wiesmaier et al., 2012).

2.1.1 Growth stages

Due to the low subsidence and large age variation between the islands of the Canarian archipelago the different stages of island formation can be studied. Ocean islands have been suggested to experience certain stages during their growth, and the Hawaiian Islands are a closely studied example of this. Clague & Dalrymple (1987) presented four stages of ocean island growth in the Hawaiian archipelago, starting with a pre-shield stage characterized by submarine alkali volcanism, followed by the shield stage. In this stage, tholeiitic magmas are erupted and the products of this stage may constitute over 95% of the total volume of the volcano. The tholeiitic lavas are capped by more differentiated lavas and alkali basalt compositions in the alkali post-shield stage, after which there is a period of erosion. Finally, the island enters the alkali rejuvenation stage (Clague & Dalrymple, 1987).

The growth stages of the Canary Islands have been classified in a similar way; however, it is constricted to a shield stage and a post-erosive rejuvenation stage. The *shield stage* is the current stage of La Palma and El Hierro. It is usually characterized by high submarine volcanic activity, forming basaltic lava that builds up the island. As for the Hawaiian archipelago, the material formed during this stage represents the bulk of the island and can be formed in only a few million years. Within the shield stage, the *seamount stage* represents the time before the island reaches the sea surface. The seamount stage, however, is mostly inaccessible and can only be studied where it crops out due to deep erosion at Fuerteventura and La Palma. Volcanic shields tend to have a low and widespread morphology due to the low viscosity of the basaltic lava, resulting in the lava spreading laterally rather than vertically. Shield volcanoes are therefore exceptions to the typical single volcanic cone morphology, and may be made of several eruptive centres and vents (Carracedo & Troll, 2016).

As the shield stage is coming to an end, the island enters a period of volcanic inactivity lasting for a few million years. After this period of inactivity, the island enters the several million year long *post-erosive rejuvenation stage*. This is a period of lower volcanic

activity, generally with magmas that are more evolved or alkaline. This period may therefore be characterized by explosive eruptions due to the higher viscosity of the evolved magmas, also resulting in stratovolcanoes with higher volcanic edifices, such as Tenerife's Mount Teide.

At a late stage of the island's evolution, mass wasting, combined with erosion, works against the volcanism to reduce the size of the island, eventually eroding away topographical variations. An example of this is Fuerteventura, which today displays a much flatter topography than for example Tenerife (Carracedo & Troll, 2016).

2.1.2 Mass wasting events

An important process in the Canary Islands is that of mass wasting. Around 11 giant landslides have been identified throughout the islands' history, not counting those whose traces might have been erased or buried by other geological processes. There are several hypotheses as to why these giant landslides occur, and although they seem to be more frequent during periods of high eruption rates, as it leads to oversteepened slopes, it is also important to consider the effect of hydrothermal alteration and erosion. It has also been proposed that extensional forces due to dyke injection could be a reason for landslides, as well as magma injections causing destabilization of the edifice (Carracedo & Troll, 2016).

As will be discussed further in section 2.1.4, the giant landslides may also have an important impact on the nature of the volcanism and the volcanic products, as they may contribute to forming new pathways for the magma by affecting the local stress fields (Longpré et al., 2008).

2.1.3 Tenerife

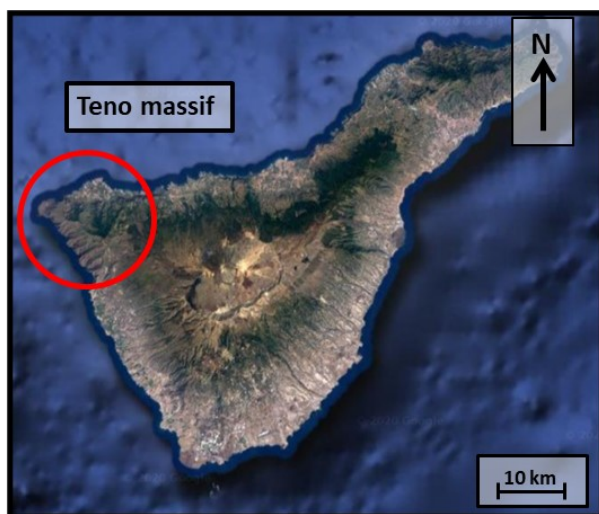
As well as being the most populated island of the Canary archipelago, Tenerife is also the largest and the highest in altitude. Three rift zones stretch to the south, northeast and northwest, giving the island the shape of a tetrahedron (fig 2). The highest point of the island, the summit of the stratovolcano Teide rising more than 3700 m above sea level, is a popular tourist attraction. If measuring from the ocean floor, the structure reaches a staggering 7000 m in height, putting it on the list of one of the highest volcanic structures on Earth. According to Guillou et al. (2004), the formation of Tenerife started 11.9 million years ago, which is earlier than the estimate of 11.29 million years previously presented by Thirlwall et al. (2000). The island was proposed by Carracedo et al. (1998) to currently be in the shield stage. However, this has been contested by several sources stating that Tenerife has gone through erosional phases which by definition would mean that the island is no longer in the shield stage (Leonhardt & Soffel, 2006; Ancochea et al., 1990; Thirlwall et al., 2000; Guillou et al., 2004). It is more likely that the island is in the rejuvenation stage, since Teide is interpreted to be at the peak of its growth. Also, as is further supported by the location of Tenerife in the middle of the archipelago, Tenerife can be regarded as an island in an intermediate evolutionary stage in compar-

ison to the other islands (Carracedo & Troll, 2016).

As current research suggests, Tenerife was formed during the shield stage by three separate island volcanoes (Anchochea et al., 1990) that later merged into one edifice: the Anaga massif (formed approx. 4.9 - 3.9 Ma), the Teno massif (formed approx. 6.4 - 5.1 Ma) and the Roque del Conde massif (formed approx. 11.9 - 8.9 Ma) (Guillou et al., 2004). It is believed that the Roque del Conde massif represents the main central shield, flanked by the Teno massif and the Anaga massif (Guillou et al., 2004; Carracedo et al., 2011). Additionally, the three shields might have had different mantle sources, as indicated by Thirlwall et al. (2000). The shield stage ended with a period of seized volcanic activity before the onset of the rejuvenation stage (Longpré et al., 2009) at ca 3.6 Ma, with the Las Cañadas volcanism playing a considerable role. In contrast to the shield volcanoes, this volcano displayed felsic and explosive eruptions—likely due to the long residence time of the magma—the products of which can be seen in the south and southeast parts of the island as thick pumice and ignimbrite layers. The volcano erupted in cycles, each cycle ending with a caldera collapse (Carracedo & Troll, 2016).

2.1.4 Ankaramites and the Teno massif

The ankaramite sample analysed in this project belongs to the Teno massif. The massif is located in the NW part of Tenerife and is characterized by a varying topography with steep ridges and valleys. It was built during eruptive phases interrupted by two events of mass wasting on the northern flank, likely taking place in a time span of approximately 250 000 years (Longpré et al., 2009). The age of the massif has been discussed by several authors (e.g. Anchochea et al., 1990), but the results of Thirlwall et al. (2000) and Guillou et al. (2004) have been interpreted to infer that the bulk of the massif was formed between 6.4 and 6.0 Ma (Leonhardt & Soffel, 2006). This is similar to the estimation of Longpré et al. (2009), which points to



Imagery ©2020 TerraMetrics, Map data ©2020

Fig 2: Three rift zones to the south, northeast and northwest give Tenerife the shape of a tetrahedron. The Teno massif is located in the north-western part of Tenerife (red circle).

6.3 Ma as the start of the formation of the Teno massif. This estimation is also supported by the results of Leonhardt & Soffel (2006) which, based on magnetostratigraphic methods, indicates that the volcanic activity in the Teno massif lasted from 6.3 to 5.1 Ma.

Longpré et al. (2009) states that from 6.3 to 6.1 Ma, phreatomagmatic eruptions were alternated with effusive eruptions of basaltic composition, building the volcano edifice. Continuous supply of magma from the upper mantle, as well as the effect of volcano load, may have led to the formation of shallow magma reservoirs in the volcano's edifice. In those reservoirs, evolved magmas were produced. Eventually, the northern flank of the volcano failed at ca. 6.1 Ma. The shallow magma reservoirs were depressurized, and what followed were explosive eruptions at the landslide headwall which to a large part drained the shallow reservoirs. The depressurization also influenced the deep plumbing system of the volcano, resulting in rapid filling of the collapse embayment by dense and less evolved magmas, initially ankaramites. As the volcano regrew, however, these dense magmas were not able to erupt as easily, and lower-density plagioclase-phyric lavas were produced instead. The process was repeated as the northern flank of the volcano became unstable once again, creating a second landslide and another period of explosive eruptions and ankaramite production, later transitioning to crystal-poor basanite lava production. There is, however, no indication of shallow magma reservoirs at this stage. At this time, mean melt fractions started to decrease which could be a sign of a decrease in hot spot influence (Longpré et al., 2009).

The chemistry of the Teno massif is characterized by relatively low amounts of SiO_2 ; and alkali basalts, subalkali basalts, basanites and picrites occur in the region. The major stratigraphic units identified are the Masca Formation (MF), the Carrizales Formation (CF), the El Palmar Formation (EPF) and the Los Gigantes Formation (LGF). Leonhardt & Soffel (2006) suggest that the oldest formation, MF, was formed between 6.27 and 6.14 Ma which is slightly different to the results of Thirlwall et al. (2000) and Guillou et al. (2004) which points to 6.42-6.02 Ma and 6.11-5.99 Ma respectively. However, in this case it is important to notice that while Leonhardt & Soffel (2006) based their results solely on magnetostratigraphic methods, Thirlwall et al. (2000) and Guillou et al. (2004) utilized Ar/Ar and K/Ar methods as well. Leonhardt & Soffel (2006) further suggests that CF and EPF chiefly were formed between 6.14 and 5.89 Ma, and that LGF, the youngest formation, was formed around 5.31 ± 0.2 Ma (Leonhardt & Soffel, 2006; Thirlwall et al., 2000; Guillou et al., 2004). The upper borders of both MF and CF are defined by unconformities formed by the two landslides described above; hence these landslides have been given the names Masca Collapse (MC) and Carrizales Collapse (CC) (Longpré et al., 2009). Both MC and CC were formed in the same polarity interval as CF and EPF, i.e. between 6.13 and 5.89 Ma (Leonhardt & Soffel, 2006). Additionally, Longpré et al. (2009) stated that the first landslide, MC, occurred at approx. 6.1 Ma, and agreed that both landslides occurred between 6.1 and 5.9 Ma. The proposed ages presented here states that all formations

formed within a short time period.

As can be deduced from the evolution of the massif, the ankaramites were predominantly deposited directly after the mass wasting events, suggesting a connection between mass wasting and the deposition of ankaramite magmas (Longpré et al., 2009). Longpré et al. (2009) has interpreted these ankaramites to represent deep magma in which crystals have had time to grow and accumulate, and from which crystal-poor magma has been removed. Therefore, it can be inferred that ankaramite magma formed continuously during the evolution of the Teno Massif. They propose that the connection between ankaramites and mass wasting is related to the load change of the volcano. Just as volcanic load increase hinders the eruption of high-density magmas, load decrease enables these high-density, likely more primitive, stagnant magmas to erupt. Furthermore, estimated high H₂O (0.8 - 2.1 wt%) and CO₂ (1.5 - 4.3 wt%) concentrations in the ankaramite magmas may have resulted in further remobilization and rapid ascent due to gas exsolution (Longpré et al., 2009).

2.2 Trace elements and elemental distribution

The use of elements, ions and ion ratios are important tools for geochemical investigations. It can be used to deduce the surrounding factors affecting a crystal during growth, and consequently receive an understanding for the history of the magmatic system. Important foundations for geochemical investigations are Goldschmidt's rules (Goldschmidt, 1937). These rules describe the distribution of elements exclusively based on ion radius and charge. The rules say that ions with smaller ion radii are more readily incorporated into solids over liquid compared to ions with bigger ion radii. It follows that Mg would be incorporated in the solid phase earlier in the crystallization sequence than Fe, as Mg is the smaller ion. Additionally, ions with higher charge (valence) are preferably incorporated into the solid over the liquid compared to ions with lower charge. Because of this, ions with high valence, for example Ti⁴⁺, are almost always readily incorporated into the solid phase. Finally, two ions with the same radius and charge should enter the solid phase in ratios proportional to their concentration in the liquid (Goldschmidt, 1937; Winter, 2014).

The term trace element is used when referring to an element that is present in concentrations of less than 0.1 wt%, and the trace elements can be grouped and classified in different ways. The terms *compatible*, *incompatible*, *high field strength elements (HFSE)* and *large ion lithophile elements (LILE)* are based on how the elements behave in magmatic systems. Elements that are compatible preferably enter the solid phase, while incompatible elements behave the opposite, i.e. they preferably enter the liquid phase. These classifications are often used when discussing partition coefficients, which are discussed further in section 2.2.1. Furthermore, HFSE refers to cations that are highly charged relative to their ionic radius, having an ionic potential >2.0, while LILE refers to cations that have low charge relative to their ionic radius (ionic potential <2.0). HFSE includes for example the rare earth ele-

ments (REE), Hf, Nb, Ce and Ti; LILE includes for example Rb, Cs, Ba, Sr and K (Winter, 2014; Rollinson, 1993) (see appendix A for index of element abbreviations and appendix A fig 1 for periodic table)

The terms *rare earth elements (REE)* and *transition metals* are used when basing the classification on the periodic table. The REE (also called lanthanides) comprises the elements with atomic numbers between 57 and 71: La, Ce, Pr, Nd, Pm, Sm, Eu, Gd, Tb, Dy, Ho, Er, Tm, Yb and Lu. These are further divided into *light rare earth elements (LREE)* and *heavy rare earth elements (HREE)*. Although the exact definition of LREE and HREE can be ambiguous, HREE included Er, Tm, Yb and Lu in a study by Baudouin et al. (2020). Apart from a few exceptions due to environmental factors, REEs have in common that they have a valence of +3. They also display what is called the *lanthanide contraction*, meaning the REEs with higher atomic numbers have smaller ionic radii than those with lower atomic numbers. Because of this, the HREEs tend to be, as inferred by Goldschmidt's rules, more compatible than the LREE. However different minerals show different sensitivities for this variation, therefore leading to different degrees of fractionation within the REE series (Winter, 2014).

The term transition metals refer to elements with atomic numbers 21-30: Sc, Ti, V, Cr, Mn, Fe, Co, Ni, Cu and Zn. Worthy of note is that this range may also include two major elements, namely Mn and Fe (Winter, 2014; Rollinson, 1993). Lastly, elements with atomic numbers 37-41 (Rb, Sr, Y, Zr, Nb), as well as Cs, Ba, Hf, Ta, Pb, Th and U, are useful in geochemical investigations, although they do not belong to any particular groups (Winter, 2014).

2.2.1 Trace element distribution

As mentioned above, the distribution of ions can be deduced using their respective ion radius and charge. For trace elements another measurement has been developed, namely the partition coefficient. Partition coefficients (D), or distribution coefficients, are specific for elements and minerals and are calculated by dividing the concentration of an element in the solid phase with the concentration of the same element in the liquid phase. This is shown in equation (1) where *x* stands for the element in question, *C* for the concentration, *s* for the solid phase and *liq* for the liquid phase:

$$D_s^x = \frac{c_s^x}{c_{liq}^x} \quad (1)$$

Estimation of partition coefficients can be done by measuring the concentration of the element in a crystal and in the glass surrounding it, or by doping synthetic or natural materials with the element. The calculation yields a number that describes whether the element is compatible or incompatible with regards to the mineral in question. Values >1 indicate that the element is compatible, while values <1 indicate that the element is incompatible (Rollinson, 1993). However, partition coefficients are heavily dependent on physical factors and can therefore vary greatly. The most important factor is the melt composition, leading to the conclu-

sion that partition coefficients can be different for instance depending on if the system is basaltic or silicic. Temperature and pressure are also factors that can affect partition coefficients. Crystal chemistry is also an important factor, as well as water content of melt and oxygen activity (Rollinson, 1993). The environmental impacts on the distribution of elements are more extensively discussed in section 2.3.

2.2.2 Trace element ratios and fractionation

Due to the fact that partition coefficients are unique for certain elements and minerals, concentrations and ratios can be used to infer influence of different minerals. Because of the accommodation of Eu and Sr into plagioclase, ratios involving these elements, e.g. Eu/Sm, Ba/Sr and Sr/Nd, can imply plagioclase fractionation. The La/Yb ratio can give information on garnet crystallization, since garnet has a larger uptake of HREE than LREE; similarly, Ni can indicate olivine fractionation. Furthermore, Sc can yield insight into the occurrence of pyroxene fractionation and Y is affected by amphibole and garnet. Additionally, elements and ratios can give information on the origin of the magma, with high concentrations of Zr and Hf indicating either evolution of the melt or an enriched source (Winter, 2014).

2.3 Clinopyroxene as a recorder of magmatic processes

The clinopyroxene end members diopside ($\text{MgCaSi}_2\text{O}_6$) and hedenbergite ($\text{CaFeSi}_2\text{O}_6$) are mainly distinguished using the Mg# ($\text{Mg}/(\text{Mg}+\text{Fe})$) (fig 3). Furthermore, the classification of augite additionally depends on the calcium content. The clinopyroxenes display a monoclinic crystal form, which for diopside consists of tetrahedral (Si^{4+}) and octahedral (Mg^{2+}) chains together with Ca^{2+} in 8-coordinated sites. The three types of pyroxenes are part of a solid solution series involving substitution of Mg^{2+} , Fe^{2+} and Ca^{2+} . Augite is characterized by Na^+ substitution in the 8-coordinated sites, resulting in a less calcic clinopyroxene, while hedenbergite is characterized by Fe^{2+} substitution in the octahedral sites, resulting in a lower Mg#. Al^{3+} can substitute into the octahedral and the tetrahedral sites as well, a process which requires coupled substitution because of the charge difference between Al^{3+} and Mg^{2+} and Si^{4+} (Klein & Philpotts, 2013). Additionally, REEs can be incorporated into both the 6- and 8-coordinated sites (Baudouin et al. 2020), with HREE being preferentially incorporated in the former and lighter REE in the latter.

As the environment changes during the growth of a clinopyroxene crystal, it is reasonable to believe that these changes are recorded in the mineral's chemistry. Because clinopyroxenes crystallize over a large variety of pressures and water contents and respond to changes in those factors, as well as in temperature and magma composition, they are good recorders of environmental changes during their growth. This is further indicated by the slow rate of diffusion taking place in the crystals, keeping the past records by hindering re-equilibration (e.g. Arimanti et al., 2007; Ubide et al., 2019; Putirka, 2008; Perinelli, 2016). Finally, Ubide et al. (2019) argues that crystallization kinetics has a pronounced influence on clinopyroxene.

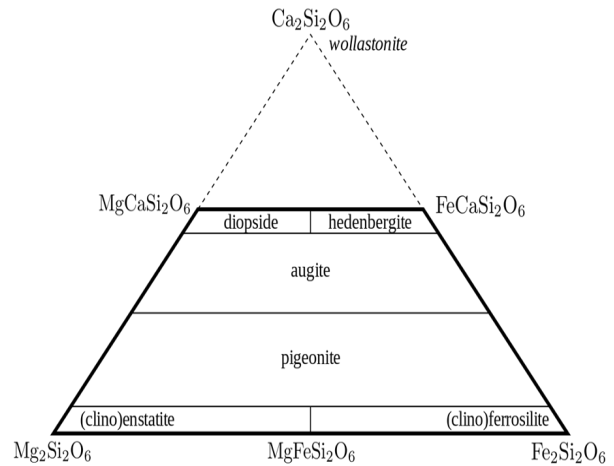


Fig 3: Classification diagram for pyroxenes. Figure by Angré, modified by Nneonneo. Retrieved 28-05-2020 from https://commons.wikimedia.org/wiki/File:Pyrox_names.svg and used under GNU Free Documentation License version 1.2: https://commons.wikimedia.org/wiki/Commons:GNU_Free_Documentation_License,_version_1.2

2.3.1. Major and minor elements in clinopyroxene

As is inferred by previous studies (e.g. Kushiro, 1960; Verhoogen, 1962), changes in the major elements of clinopyroxenes, i.e. substitution, can be attributed to changes in the environment in which they grow. The three principle factors that are considered are chemical composition, temperature and - despite perhaps being negligible - pressure of the magma in which the clinopyroxene crystals are formed (Kushiro, 1960).

Regarding the chemical composition, Kushiro (1960) argues that the amount of SiO_2 present in the magma might affect the amount of Al and Ti in the clinopyroxene crystal. As mentioned, Si is allocated into the tetrahedral sites in which Al can substitute. Magmas oversaturated in SiO_2 (tholeiitic magmas) would therefore fill the tetrahedral sites, resulting in a lower total amount of Al, with Al only allocated in the octahedral sites. Alkali magmas, on the other hand, contain less SiO_2 and would therefore leave room for more Al in tetrahedral sites, and result in a higher total amount of Al. It follows that a magma body with lower amount of SiO_2 result in clinopyroxenes with higher Al/Si ratio. Following this, the substitution of Al into the tetrahedral sites requires a coupled substitution into the octahedral sites to account for the charge difference between Al^{3+} vs Si^{4+} . In alkali magmas, as they are often rich in TiO_2 , this coupled substitution may involve Ti ions. This is also inferred by Verhoogen (1962), stating that Ti is favoured by Al being allocated in the tetrahedral sites, and therefore by low SiO_2 concentrations in the magma. As a result, clinopyroxenes in alkali magmas are often Ti-rich due to low concentration of SiO_2 in combination with high concentration of TiO_2 in the magma (Kushiro, 1960). Kushiro (1960) also mentions that the possibility of TiO_2 concentration being the controlling factor by resulting in high Ti content in clinopyroxene, leading to high Al content as well, cannot be ruled out.

Another possible reason for chemical variations is the temperature of the magma. According to Kushiro (1960), higher temperature leads to the clinopyroxenes being able to contain more Al in the tetrahedral sites than those that were formed at lower temperature. Higher temperatures would therefore result in higher amounts of Al in the tetrahedral sites, leading to a lower amount of Si. This temperature effect also applies to Ti, as described by Verhoogen (1962). They argue that since the incorporation of Ti is not favourable with respect to energy it requires entropy and therefore high temperatures.

2.3.2 Trace elements in clinopyroxene - variation in partition coefficients

Partition coefficients (D) for trace elements in pyroxenes mainly seem to depend on temperature, pressure, pyroxene composition and crystal features, and liquid composition (Green, 1994). For example, studies show that D-values for some REE elements increase with decreasing temperature and decreasing pressure in basaltic compositions (Green, 1994; Dunn, 1987; Adam & Green, 1994). However, compositional effects may be the most important factor, overwhelming the effect of temperature and pressure (Hack et al., 1994). Green (1994) found that despite creating a similar pattern, partition coefficients for individual elements in calcic pyroxenes generally display higher values than those in low-calcic pyroxenes, as well as a larger variation which can be expected due to the higher number of possible melt compositions and the complex interactions that follows a higher Ca concentration. Additionally, heavy REEs seem to behave with higher compatibility in high-Ca pyroxene than light REEs. These examples illustrate the dependency of D-values on Ca concentration (Green 1994; Hack et al., 1994; Van Orman et al., 2001). Partition coefficients also seem to be dependent on Al and Ti concentrations, as the amount of Al in the tetrahedral sites seem to affect the D-values for REEs, HFS elements, Cr and V (Green, 1994; Skulski et al., 1994).

D-values are also affected by crystal features such as sector zoning, resulting in preferential accommodation of some elements in certain sectors. This will be discussed further in section 2.3.5.

The effects of liquid composition can be applied on silicic versus basaltic compositions, as silicic liquids usually result in higher D-values (Green, 1994). This may also be applicable on tholeiitic and alkali basalts, as HFSE partition coefficients were observed to be 2-3 times higher in alkali basalts, according to Forsythe et al. (1991).

2.3.3 Literature values for partition coefficients (D) for clinopyroxene

Keeping the information above in mind, it is possible to estimate the partition coefficients for different elements between two phases. In this case, the partition coefficient between clinopyroxene and melt is of interest. Table 1 shows a compilation of partition coefficients presented in six different publications. Hart & Dunn (1993) and Villament et al. (1981) used alkali basalt, Foley (1996) alkaline lamprophyre, Bougault &

Hekinian (1974) and Matsui et al. (1977) basalt and Hauri et al. (1994) high-alumina basalt for their investigations of the clinopyroxene partition coefficients. As is evident in this table, the estimated partition coefficients are highly variable, which to some extent might depend on the analytical techniques used, but also on the factors discussed above. However, it is possible to see the general trend for each element. As mentioned in section 2.2.1, HREE tend to be more compatible than LREE due to the difference in ionic radii as a result of the lanthanide contraction. This is evident in Table 1 since the heavier REE, for example Lu, have higher partition coefficients than the lighter REE. Considering that the partition coefficients are <1 , however, all REEs are more or less incompatible.

The transition metals seem to overall have partition coefficients >1 , inferring that they are compatible and preferably incorporated into the clinopyroxene over the melt. Most striking is the value of 13 for Cr by Bougault & Hekinian (1974), indicating that Cr is highly compatible in clinopyroxene. Even though the other studies have not estimated a value that high, all of the estimated partition coefficients are high with the exception of Hauri et al. (1994) which estimated a D-value of mere 1.66. Hence it is noticeable that - within the scope of these six studies - Cr is the most compatible element in clinopyroxenes of all transition metals, and in fact of all elements present in this table. Ni is not far behind, with D-values of 2.5 and 4.4 (Villemant et al., 1981; Bougault & Hekinian, 1974).

Another noticeable element is Ba, which in four out of the six studies has a very low partition coefficient and therefore seems to be highly incompatible in clinopyroxenes (e.g. Matsui et al., 1977). Nb as well has very low partition coefficients, together with Rb (e.g. Foley, 1996). The other elements - Sr, Y, Zr, Hf, Ta, Th and U - are all incompatible with generally lower partition coefficients than the REE.

Finally, Bougault & Hekinian (1974), Matsui et al. (1977) and Villemant et al. (1981) presented a few D-values for major and minor elements Si, Al, Fe, Mg, Ca and Na. Generally, these are not particularly incompatible, and Mg and Ca are compatible with D-values of 5.4 and 3.4 respectively (Villemant et al., 1981).

2.3.4 Zoning types

Clinopyroxenes and other minerals part of a solid solution series regularly display different kinds of compositional zoning as a response to environmental changes during crystal growth. Zoning can be *normal*, i.e. composition changes from high temperature compositions in the core to low temperature compositions in the rim due to cooldown, or *reverse*, meaning the opposite: composition changes from low temperature to high temperature compositions as a response to magma temperature changes, magma mixing and magma influx (Klein & Philpotts, 2013). *Patchy* zoning describes zoning that is irregular throughout the crystal. It may form by crystallization of melt of another composition in cavities of an existing mineral, and can also be a sign of open system processes (Streck, 2008).

Oscillatory zoning can occur as fine and coarse banding (Downes, 1974) and may be caused by diffu-

Table 1: Estimated partition coefficients for selected trace elements and major/minor elements. The partition coefficients are estimated for clinopyroxene in *basalt* (Bougault & Hekinian, 1974; Matsui et al., 1977); *alkali basalt* (Villemant et al., 1981; Hart & Dunn, 1993); *high-alumina basalt* (Hauri et al., 1994) and *alkaline lamprophyre* (Foley, 1996). See appendix A for index of element abbreviations.

Element	Bougault & Hekinian (1974)	Matsui et al. (1977)	Villemant et al (1981)	Hart & Dunn, 1993)	Hauri et al. (1994)	Foley (1996)
La		0.084	0.12	0.0536	0.0515	0.0435
Ce		0.166		0.0858	0.108	0.0843
Nd		0.382		0.1873	0.277	0.173
Sm		0.736		0.291	0.462	0.283
Eu		0.753	0.63		0.458	0.312
Gd		0.82				0.335
Tb		0.97	0.73			0.364
Dy				0.442	0.711	0.363
Er				0.387	0.66	0.351
Tm		1.09				0.297
Yb		1.01		0.430	0.633	0.313
Lu		0.95		0.433	0.623	0.265
Sc		2.92	3	1.31	0.808	
Ti	0.2	0.786	1.07	0.384	0.451	
V	0.74			3.1	1.81	
Cr	13	4.22	5.3	3.8	1.66	
Co	1.32	1.12	1.02			
Ni	4.4		2.5			
Rb			0.04			0.0047
Sr		0.109	0.16	0.1283	0.157	0.0963
Y				0.467		0.438
Zr			0.27	0.1234	0.195	0.121
Nb				0.0077	0.0081	0.0027
Ba		0.0035	0.04	0.00068	0.0058	0.00061
Hf			0.48	0.256	0.223	
Ta			0.06			
Th		0.013	0.04		0.014	0.0056
U		0.017	0.05		0.0127	
Si		0.926	0.91			
Al		0.55	0.48			
Fe(tot)	0.86		0.99			
Mg			5.4			
Ca			3.4			
Na			0.17			

sion processes and kinetic controls or by convecting magma, or similar dynamic processes, resulting in temperature variations. By making a distinction between fine banding (~1-10 μm) and coarser banding, it might be possible to discern the origin of the zoning as the former may be the result of kinetic processes, while the latter may be the product of magmatic processes (Klein & Philpotts, 2013; Streck, 2008; Ginibre et al., 2002). Streck (2008) restricted the definition of oscillatory zoning to the fine banding caused by kinetic processes, highlighting the different origin of the two types. This definition will be taken into consideration here, and the distinction between oscillatory zoning and *growth bands* will to some extent be made with regards to band width, with a general distinction between the two at 10 μm .

Finally, *sector zoning* is characterized by different compositions in different faces of the crystal, which in thin section corresponds to different sectors (fig 4). The sectors typically observed in crystals displaying hourglass zoning are $\{-111\}$ (basal sector or hourglass sector) and $\{100\}$, $\{110\}$ and $\{010\}$ (prism sectors) (e.g. Leung, 1974; Ubide et al., 2019). Hollister & Gancarz (1971) proposed four factors affecting the nature of the sector zoning: rate of material addition to crystal, composition and size of said material, equilibrium rate of new material with matrix, and re-equilibration rate by ion exchange. Additionally, they argue that sector zoning can indicate a high growth rate during the crystallization, as it exceeds the diffusion rate (Hollister & Gancarz, 1971). Furthermore, Skulski et al. (1994) claimed that sector zoning in augites is caused by differences in kinetic growth processes, and Downes (1974) stated that the main influencing factors are the composition of the melt, the structure of the crystal and the site occupancy, and the different growth rates of the crystal faces.

2.3.5 Implications and previous studies regarding zoning

Regarding oscillatory zoning, Downes (1974) carried out a study on oscillatory zoning combined with sector zoning in calcic augites, in which they found two types of lamellar bands - coarse banding with varying thickness, commonly approx. 250 μm , and fine, regular banding approx. 20 μm thick - that lay parallel to the face of the sector in question. They suggested that the bands were formed due to a primary growth processes, simultaneous with crystallization. When examining the fine banding, they found no normal core-to-rim zoning, and no clear oscillations for Fe, Mg and Ca. However, Al and Ti oscillated between 1.0-1.5 wt% and 0.2-0.4 wt% respectively, and there was a drop of Al and Ti within each band.

Experiments by Skulski et al. (1994) demonstrated that sector zoned augite in basalts of alkaline composition showed an enrichment of Al and Ti, as well as Ca, Cr, HFSE and REE in the $\{100\}$ sector compared to the $\{010\}$ sector (at 1250 $^{\circ}\text{C}$ and 1 GPa). They further observed reverse zoning of incompatible elements in the $\{100\}$ sector, as well as normal zoning in the $\{010\}$ sector. These observations are supported by the results from an experimental study by Hack et al. (1994), where they observed that especially alkaline

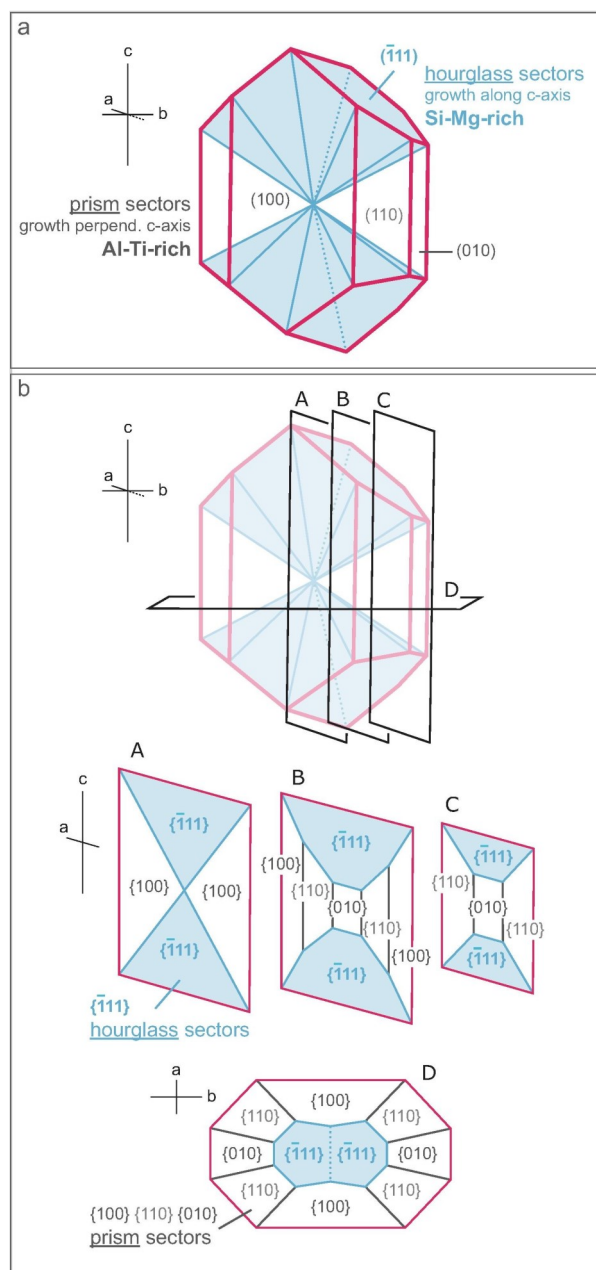


Fig 4: Crystallographic principles of sector zoning. a) The sectors in relation to an augite crystal and b) an illustration of how cutting effects affect the appearance of the sector zoning in thin section. As is evident from the figure, the typical hourglass zoning (bA) is only achieved if the crystal is cut along the c-axis in the centre of the crystal. A cut parallel to the c-axis but not in the centre will cause the hourglass sectors to drift away from each other (bB-C). Figure reused with permission from Ubide et al. (2019), who in turn modified from Leung (1974) (see reference list for complete acknowledgement).

compositions were host to sector zoned clinopyroxenes, and that Al, Ti and REE showed the largest variation between the sectors. Finally, Ubide et al. (2019) also concludes that HFSE and REE elements are strongly influenced by kinetic effects, and therefore also show pronounced sector zoning.

In a study carried out by Leung (1974), sector zoned titanaugetes were found to show compositional

differences, i.e. zoning, in both the core-to-rim direction and in sectors. In the core-to-rim direction, an increase of Si and a decrease of Al of up to 5 wt% oxide were observed, as well as an enrichment of Fe and a depletion of Mg. The Fe and Mg changes would indicate a higher to lower temperature crystallization, as the high temperature phase - the Mg phase - is depleted. They did, however, observe a few crystals which exhibited a slight increase of Mg towards the rim, occurring along with a sudden Al decrease. Ca remained relatively constant throughout the crystal, and Ti decreased slightly towards the rim (0.5-1 wt% oxide), however it behaved very varied (Leung, 1974). When studying the chemistry of sector zoning, Leung (1974) further found that sector $\{-111\}$ (basal sector) was enriched in Si and Mg, and sectors $\{100\}$, $\{110\}$ and $\{010\}$ (prism sectors) were enriched in Al, Ti and Fe (as inferred by fig 4). Sector $\{010\}$ also showed a slight depletion of Al and Ti compared to $\{100\}$ and $\{110\}$, concordant with Hollister & Gancarz (1971) who suggested that the degree of enrichment of Al, Ti and Fe are as follows: $\{100\} > \{110\} > \{010\} > \{-111\}$. Ubide et al. (2019) found similar results, concluding that the hourglass sectors and the prism sectors showed chemical variations due to a charge-balancing coupled substitution: $[\text{Si}^{4+} + \text{Mg}^{2+} + \text{Fe}^{2+}] \rightarrow [\text{Al}^{3+} + \text{Ti}^{4+} + \text{Fe}^{3+}]$. The prism sectors thus displayed higher concentrations of Al and Ti, and the basal sectors displayed higher concentrations of Si and Mg.

Leung (1974) further assessed growth rates when studying the sector zoning in titanaugites. They suggested that the observed *growth layers* - a term used in that study to describe layering parallel to the bases of growth pyramids, likely similar to the banding mentioned in Downes (1974) - may form as a result of cyclic convections during growth. These cyclic convections might in turn be caused by heat of fusion accumulated at the solid-liquid interface as elements are incorporated in the crystal. Following this, they propose that the rate with which heat is emitted from the crystal face determines the growth rate, even though the growth rate is sensitive to rate of diffusion and degree of supercooling as well. In pyroxenes, they suggest that the $\{-111\}$ face is a fast growing face in hourglass-structured pyroxenes, followed by $\{100\}$, $\{110\}$ and $\{010\}$. They also suggest that the absence of $\{001\}$ faces in their samples indicate that it is the fastest growing face, essentially growing so fast that it eliminates itself, and would therefore likely not be present in pyroxenes formed with high growth rate.

Finally, in a study by Longpré et al. (2008), clinopyroxenes from the El Palmar Formation in the Teno massif was examined with special interest in zoning, (dis)equilibrium and thermobarometry. They observed 20-40 μm Fe-Mg zoning in the rims that was in disequilibrium with the melt and that was determined to be the result of growth processes, in contrast to diffusion processes. This was inferred by the fact that elements of different diffusion coefficients displayed zoning of similar width, as did olivine which would have a higher diffusion rate than clinopyroxene in those conditions (Longpré et al., 2008; Freer, 1981). Taking after a study by Klügel et al., (2000) discussing the same type of zoning in olivine, they further indicated that the zoning might have been created at high

growth rates, and that the rims likely formed on a short time-scale of up to a few days (Longpré et al., 2008; Klügel et al., 2000). Additionally, they suggested that the high growth rate of the rims were a result of undercooling due to water enrichment during magma ascent in combination with decompressional crystallization and degassing (Longpré et al., 2008).

2.3.6 Magma recharge and mixing

Open system processes may have a large impact on magmatic systems, and determining the role of these processes is therefore an important key to understand the evolution of a system. Streck (2008) has presented a comprehensive guide regarding zoning and crystal textures that might serve as evidence for open system processes, i.e. contamination and magma mixing/recharge. The presence of reverse zoning, step zoning (zoning that occurs in steps, in contrast to progressive zoning that occurs gradually), growth bands and patchy zoning, as well as resorption textures, are signs that may point towards open system processes. However, important to note is that patchy zoning may arise from re-equilibration processes as well (Streck, 2008). Reverse zoning indicates a crystallization that does not follow the liquid line of descent for that particular mineral, i.e. it is not only affected by cooldown and the related fractionation. Additionally, as mentioned in section 2.3.4, growth bands can be an indicator of open system processes if formed as a primary growth feature, as suggested by Downes (1974). Furthermore, abrupt changes in temperature and chemistry caused by mixing with newly arrived hot magma can result in disturbed sector angles, irregular dissolution surfaces and intervals of more primitive magma composition (Ubide et al., 2019; Streck, 2008; Ubide & Kamber, 2018). Finally, rounded grains and spongy texture are examples of resorption textures that might indicate open system processes (Streck, 2008).

An interesting aspect of open system processes is that of magma recharge, also commonly referred to as mafic replenishment, and its possible connection to eruption triggering. However, the role of magma recharge as an eruption trigger has not yet been fully understood, and few studies have been carried out. Ubide & Kamber (2018) showed that traces of magma recharge and magma mixing can be seen in clinopyroxene phenocrysts from Mt. Etna, by analysing variations in Cr concentration preserved in the clinopyroxene due to high compatibility and relatively slow diffusion. They noted that the clinopyroxene crystals displayed distinctive Cr zoning and that the Cr-rich zones were rich in other compatible elements as well, reflecting the arrival of new primitive magma. The Cr-rich zones were interpreted to have crystallized shortly before the eruption, as they occurred close to the clinopyroxene rims, creating a possible connection between arrival of primitive magma and the eruption. The crystallization of the Cr-rich zones depleted the system of Cr, causing the crystal's outermost rim, outside of the Cr-rich zones, to be characterized by low Cr concentrations as well as an increase in Al and Ti and a decrease in Mg and Si. These rims likely represent final decompression and surface crystallization (Ubide & Kamber, 2018). This topic was discussed in Ubide et

al. (2019) as well, however with focus on sector zoned phenocrysts. In this study they found Cr enriched and HFSE and REE depleted zones in a sector zoned mantle overgrowing a Na-rich resorbed core. They argued that the depletion of HFSE and REE in these zones is a charge balancing mechanism compensating the increased incorporation of Al in the tetrahedral sites. They also found that the transition metals Cr³⁺, Sc³⁺ and Ni²⁺ experience little to no sector zoning, and therefore little response to kinetic processes, and that these elements therefore are reliable when evaluating open system processes to constrain magmatic histories (note, however, that this observation contradicts that of Skulski et al. (1994) who found that Cr was enriched in certain sectors, see section 2.3.5). Finally, similar to Ubide & Kamber (2018), this study also observed rims enriched in Al and Ti (Ubide et al., 2019).

3 Methods

A variety of analytical techniques were used in this thesis in order to carry out qualitative and quantitative analyses for both major and minor elements and trace elements, including scanning electron microscope (SEM) analyses for major and minor elements and laser ablation inductively coupled plasma mass spectrometry (LA-ICP-MS) analyses for trace elements. An explanation for the workings of these instruments and analytical techniques are to be found in appendix B.

Two thin sections, ASTE17.03A1 and ASTE17.3A2, derived from the same ankaramite sample from the Teno massif, Tenerife, were viewed using optical microscope Olympus BX53. They were observed to exhibit a porphyritic texture consisting of large clinopyroxene crystals, and to a lesser extent large olivine and plagioclase crystals, surrounded by a matrix containing prismatic plagioclase needles and small-scale pyroxene and olivine crystals. The crystals are varying in size and shape, with some displaying euhedral crystal shape while others rather display subhedral to anhedral crystal shapes. Opaque minerals were also found in matrix and in the interior of crystals. Flow texture was observed throughout the thin sections. Four clinopyroxene crystals, two from each thin section, were elected for further analyses based on crystal quality and equilibrium, as well as size and presence of zoning: A1a and A1b from the A1 thin section and A2a and A2b from the A2 thin section.

3.1 Scanning electron microscopy (SEM)

The clinopyroxene crystals presented were studied with scanning electron microscope Tescan Mira 3, using BSE, SEM-EDS and EBSD analyses. Special interest was taken to the chemical variations observed from the core of the clinopyroxene to the rim, paying extra attention to the chemical changes that characterizes the zoning. BSE was used for imaging, to acquire a first impression of the present phases and to view zoning in terms of compositional differences. The majority of the analyses consisted of SEM-EDS measurements, specifically point analyses (spectrums), lines and compositional maps. The instrument was calibrated using cobalt (Co), and the analyses were mainly performed with HV = 15 kV, BI = 15.00 and WD = 15 mm.

EBSD analyses were carried out for crystal A1a to determine the crystallographic axes of the crystal in order to relate its orientation in the thin section to the zoning. The analyses were performed in low vacuum and was therefore carried out without carbon coating of the sample. LVSTD (Low Vacuum Secondary Tescan Detector) were used with the following settings: 40 Pa Uni-Vac, HV = 20 kV, tilt correction = 70o and dynamic focus = 70o.

Both EDS and EBSD analyses were carried out and evaluated using software Aztec 3.3.

3.1.1 SEM: Sample preparation

For BSE imaging and SEM-EDS analyses the thin sections were coated with carbon to avoid issues with charging of the sample. Additionally, bits of carbon tape were used between the sample and the sample holder to further diminish charging effects.

For the EBSD analyses, the already carbon-coated thin section was polished using diamond paste and colloidal silica. The thin section was thereafter washed carefully with water and dish soap and put in ultrasonic bath (Branson 200 Ultrasonic Cleaner) and a stub was attached to the thin section with double coated carbon tape and silver paint.

3.2 Laser ablation inductively coupled plasma mass spectrometry (LA-ICP-MS)

LA-ICP-MS was performed to analyse trace element concentrations and variations. The analyses were carried out using a Bruker Aurora Elite ICP-MS equipped with a 193 nm Cetac Analyte G2 excimer laser in helium atmosphere. The standards used were NIST610 as a primary standard and NIST612, BCR2G and BIR1G as secondary standards, and finally Ca as internal standard with a concentration of 15.66 wt%. Nineteen lines with spot size 13x85 µm and nineteen spot analyses with spot size 30x85 µm (fig 5) were taken, distributed in all four crystals. The elements analysed were Si and Na, the REEs La, Ce, Pr, Nd, Sm, Eu, Gd, Dy, Er and Yb; the transition elements Cr, Ni, Co, Ti, V and Sc; and finally Zr, Sr, Y, Hf, Ba and Nb. Special interest was taken to the chemical variations in the zoning and the rims, and the lines were drawn perpendicular to the concentric zoning to gain accurate information of the chemical variations. The results were processed using Igor Pro 6.37 and Iolite v.3.

3.2.1 LA-ICP-MS: Sample preparation

For the LA-ICP-MS analyses the carbon coat was removed using DiaPro Nap ¼ diamond paste, after which the thin sections were washed with water and finally put in ultrasonic bath and cleaned with ethanol.

3.2.2 Evaluating LA-ICP-MS results

Part of the evaluation of the LA-ICP-MS results involved calculating the liquid composition at the time of crystallization of the analysed pyroxene. This was carried out using the mathematical relationship for partition coefficients, as described in section 2.2.1.1:

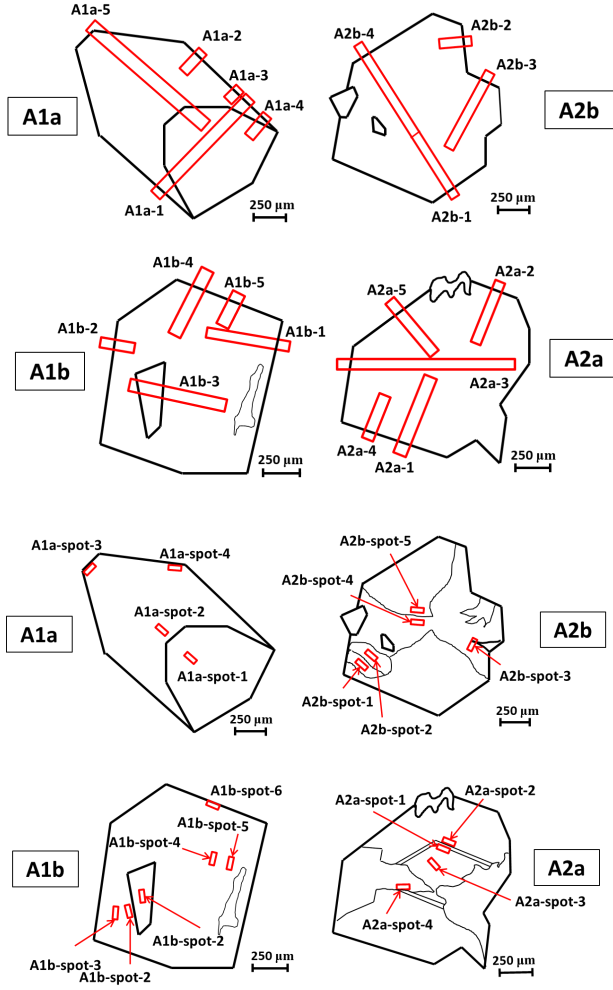


Fig 5: Schematic sketch of the four clinopyroxene crystals and the location of the lines and spots with LA-ICP-MS. Main features have been added to the sketches in order to acquire a better apprehension for the locations in relation to the features.

$$D_{cpx}^x = \frac{C_{cpx}^x}{C_{liq}^x} \quad (2)$$

where D stands for the partition coefficient of the element x in clinopyroxene and C for the concentration of element x in the clinopyroxene and the liquid respectively. The equation was rewritten to solve C_{liq}^x :

$$C_{liq}^x = \frac{C_{cpx}^x}{D_{cpx}^x} \quad (3)$$

Additionally, relative partition coefficients were estimated between the sectors of the sector zoning in A1a by using the composition of two sectors, here referred to as sector A and B. For the sake of the calculation, this was done by assuming that the chosen partition coefficients (see section 3.2.3) are true for sector A, and the liquid composition was therefore calculated for that sector. As follows, the calculated liquid composi-

tion would be assumed to represent the true liquid composition at the time of crystallization. Thereafter, equation (2) was used to determine the partition coefficients based on the liquid composition of sector A and the clinopyroxene composition of sector B, thus acquiring partition coefficients for sector B as illustrated by equation (4) below.

$$D_{cpx,B}^x = \frac{C_{cpx,B}^x}{C_{liq,A}^x} \quad (4)$$

Calculations for relative partition coefficients were made with the assumptions that the liquid composition did not change over time as the sector zoned crystal was formed and that the sector zoning was solely kinetically controlled.

3.2.3 Chosen partition coefficients for evaluation

To determine reliable partition coefficients, values from the literature (see table 1) were chosen, primarily from Villemant et al. (1981) and Hart & Dunn (1993), but also Foley (1996). These partition coefficients were then plotted against ion radii for 6- and 8-coordinated (M1 and M2) ions in an Onuma diagram (fig 6). This diagram is based on the *lattice strain model* (e.g. Blundy & Wood, 2003), describing the dependency of partition coefficients on ion charge, ion radius, site radius and that site's elastic response, suggesting that the ion that can be incorporated into the lattice with low strain will have a higher partition coefficient than an ion incorporation resulting in higher strain. As can be deduced from fig 6, the lattice strain model allows for prediction of partition coefficients solely based on charge and ion radius (Blundy & Wood, 2003).

The curves in fig 6 represents the lattice strain model, and are drawn based on a similar diagram by Purton et al. (1997). The partition coefficients were evaluated based on how well they fit the curves in the diagram, and this was used to estimate new or verify existing partition coefficients. Some elements were however left uncorrected due to the uncertainty of the typical accommodation site of the element in clinopyroxene, in which case it was considered more appropriate to verify the partition coefficient using the literature. Finally, the partition coefficient for Pr was solely estimated using the diagram, taking into account the partition coefficients for Ce and Nd. The resulting partition coefficients are presented in table 2.

4 Results

4.1 Optical observations

The four chosen clinopyroxene crystals have in common that they are euhedral with some fracturing and are containing plagioclase and opaque inclusions that are concentrated mainly along the rims. The crystals also display zoning. However, the type and extent of this zoning is not the same for all crystals. Based on the kind of zoning, the crystals have been sorted into two groups: the A1a and A2b crystals and the A1b and A2a crystals (fig 7).

The A1a crystal measures 1.75 mm at the long-

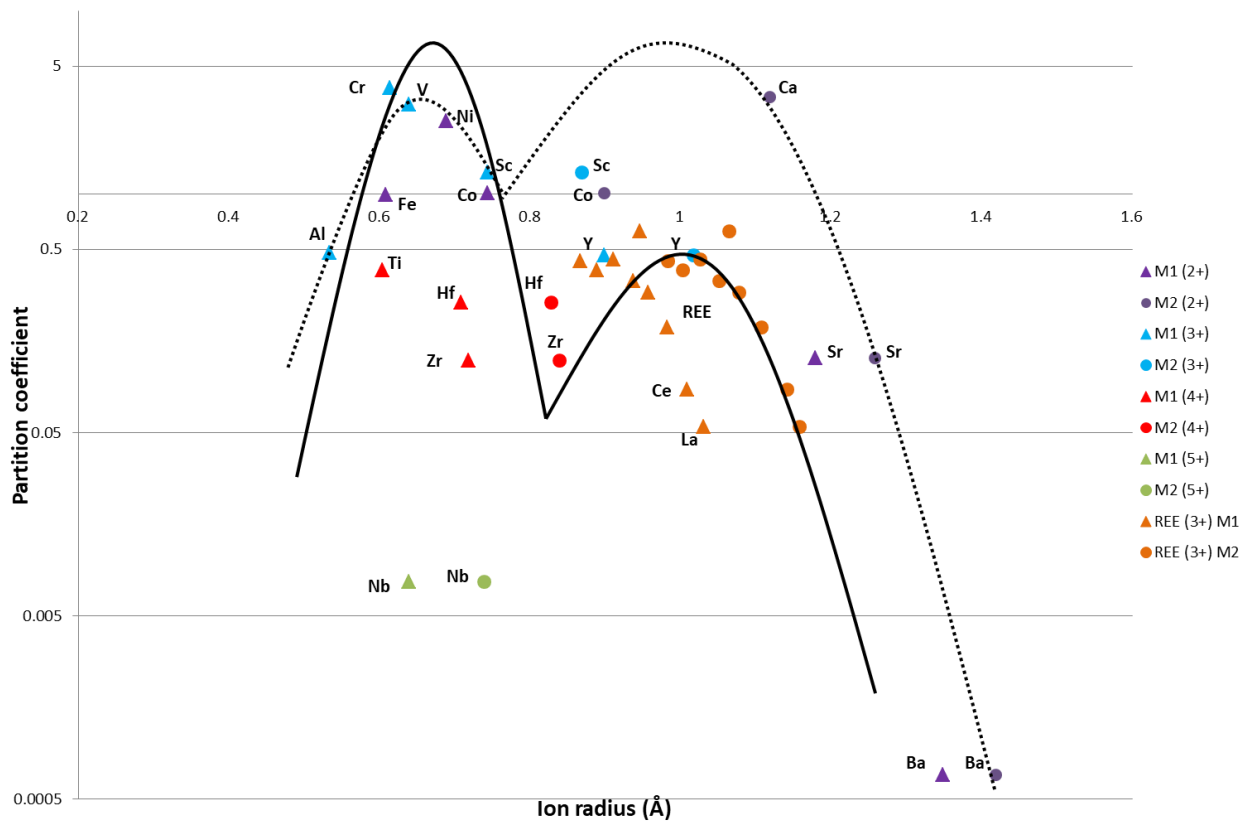


Fig 6: The partition coefficients to use when evaluating the LA-ICP-MS results were chosen with consideration to the Onuma diagram. The partition coefficients are acquired from Villemant et al. (1981), Hart & Dunn (1993) and Foley (1996) and are plotted against ion radii for 6-coordinated (M1) and 8-coordinated sites (M2). The lines were drawn based on a similar diagram by Purton et al. (1997), representing the *lattice strain model* (e.g. Blundy & Wood, 2003). The solid line strives to connect elements with 3+ charge and the dotted line elements with 2+ charge.

Table 2: The final partition coefficients chosen with consideration to the Onuma diagram and used for evaluation of the LA-ICP-MS results.

Element	La	Ce	Pr	Nd	Sm	Eu	Gd	Dy	Er	Yb	Hf
D-value	0.054	0.0858	0.137	0.187	0.29	0.63	0.335	0.442	0.387	0.43	0.256
Element	Sc	Ti	V	Cr	Co	Ni	Sr	Y	Zr	Nb	Ba
D-value	1.31	0.384	3.1	3.8	1.02	2.5	0.1283	0.467	0.1234	0.0077	0.00068

est axis and exhibits sector zoning with two clearly visible sectors and high interference colours; orange in one sector and pink in the other. One of the sectors can be seen to vaguely be divided into five very similar subsectors (fig 8). Additionally, the crystal has a slightly darker interval approaching the rim. A twinning plane runs through the crystal and the two twins mirror each other and have different extinction angles. The crystal is free from inclusions except for a small plagioclase crystal in the interior of the pyroxene. The A2b crystal measures 1.6 mm and also seems to display two twins with different extinction angles and sector zoning, although the twinning plane is slightly uneven and the sectors are somewhat irregular and presented differently. Additionally, as is evident in fig 7 the A2b is different from A1a in that it has lower interference colours; brown and grey. It also contains

more inclusions, namely a large plagioclase crystal and a large opaque crystal in the rim, as well as a smaller pyroxene. Lastly, A2b seem to display a similar interval in the outer parts of the crystal as A1a; however, A2b displays clear concentric zoning in this interval.

The A1b crystal measures 1.6 mm and displays lower interference colours than A1a - displaying dark and light beige colours - and contains numerous inclusions, specifically a large plagioclase crystal and several opaques. The small inclusions are mostly concentrated near the centre of the crystal, right next to a darker brown area with an irregular shape that seems to represent the core of the crystal. The rest of the crystal is characterized by concentric zoning parallel to the rims with varying width, and seemingly different widths in different parts of the crystal. The zoning is

especially pronounced approaching the outer parts of the crystal, as the zoning in the inner parts is poorly pronounced. The A2a crystal measures 1.7 mm and is similar to A1b in that it has low interference colours, also dark and light beige, and varying concentric zoning that is parallel to the rims and is less pronounced in the interior of the crystal than closer to the rim. However, the A2a crystal does not exhibit any signs of a darker core. Rather, the central part of the crystal – where the zoning looks patchy and irregular rather than concentric – is host to numerous small inclusions. Furthermore, one part of the crystal seem to be overprinted and lack zoning. Finally, a larger plagioclase inclusion is present in the rim of the crystal.

4.2 Scanning electron microscopy (SEM-EDS)

The scanning electron microscope analyses revealed that all four of the clinopyroxene crystals are of diopside composition (using the classification by Morimoto (1988)), i.e. the Mg end-member of the clinopyroxene series. The crystals are relatively homogenous when it comes to Na and Ca, presenting only small changes that seem to be random without following any specific trend. Therefore, the elements of interest in these analyses were Mg, Si, Al, and Ti, and to some extent Fe, and their variations in relation to the zoning of the crystals. For representative data from SEM-EDS spectrums the reader is referred to appendix D.

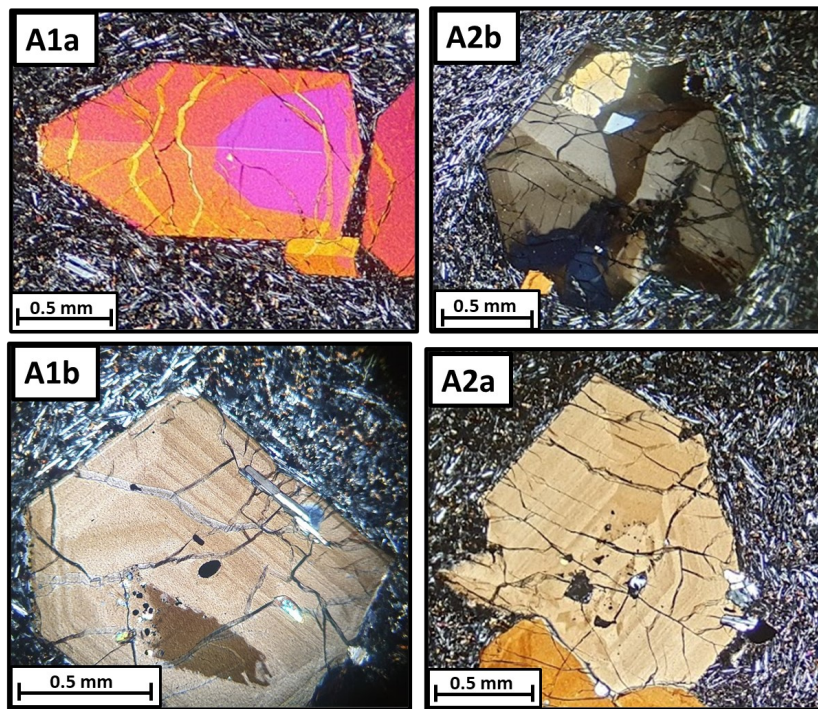


Fig 7: The four clinopyroxene crystals chosen for the chemical analyses viewed under crossed polars in optical microscope. The longest axes measures 1.75 mm in A1a, 1.6 mm in A2b, 1.6 mm in A1b and 1.7 mm in A2a. Note the difference in zoning between A1a/A2b and A1b/A2a, and the twinning plane running through A1a and A2b.

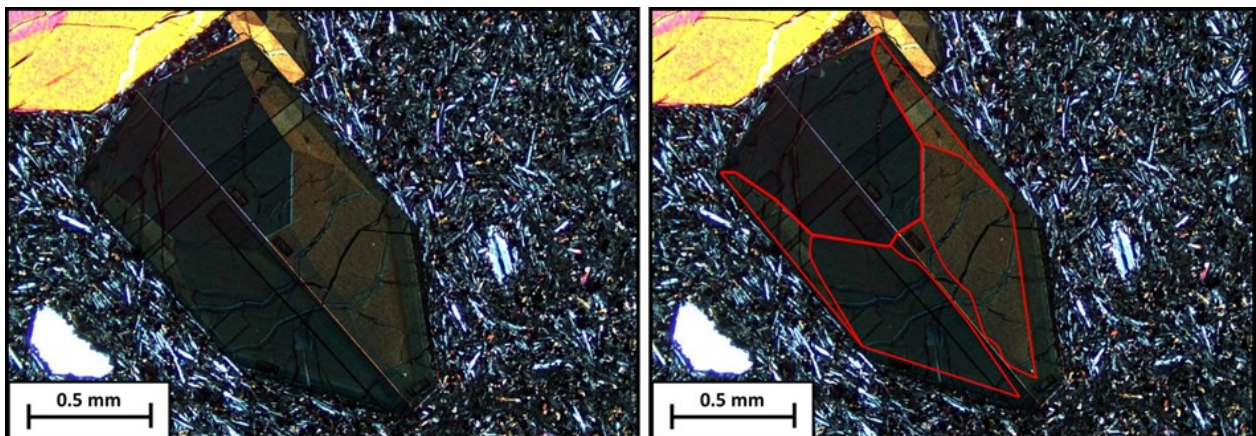


Fig 8: Figure illustrating the subsectors observed in A1a observed under crossed polars in optical microscope. To the left, two pictures of A1a under crossed polars are combined to produce a picture where both twins are extinguished in order to acquire a better view of the subsectors. To the right, these subsectors are marked with red lines.

4.2.1 Sector zoned crystals: A1a and A2b

Starting off with the sector zoned crystals A1a and A2b, the sector zoning is clearly visible when using the backscatter electron (BSE) detector (fig 9). One sector displays a darker contrast than the other, and it is this sector that according to EDS analyses displays high Mg and Si concentrations relative to the lighter sector, which in turn has lower concentrations of these elements and higher concentrations of Al and Ti. The same pattern is seen in both sector zoned crystals, the two of them having virtually the same chemical compositions. In general, the Mg+Si sectors have a Mg# of ~75-79 and the Al+Ti sectors an Mg# of ~73-76, i.e. the Al+Ti sectors are generally characterized by lower Mg#. However, both sectors have Al/Ti ratios of ~3.0-4.5.

Going from the Mg+Si sector to the Al+Ti sector, Mg and Si decrease by around 8-14 wt% and 4-8 wt%, while the Al and Ti increase is very varied, ranging from approx. 50-80 wt% for Al and 20-80 wt% for Ti. Fe concentration does change when going from one sector to the other; however, the changes are small and without any certain pattern, as Fe can both increase and decrease between the Mg+Si to the Al+Ti sector.

In addition to these two sectors, the Al+Ti sector of A1a seem to be further divided into five subsectors. All of these subsectors have similar compositions; however, they display slightly different contrasts in BSE (fig 9).

Apart from the sector zoning, both crystals are relatively homogenous in the core-to-rim direction. However, A2b also display irregular compositional variations slightly resembling that of patchy zoning. This compositional variation is clearly evident in EDS maps (see appendix C, figure 1). The “dark spots” of this irregular zoning has the same chemical composition as the Mg+Si sectors. Additionally, the concentric zoning in the outer parts of A2b is slightly visible in Al, Ti, Mg and Si, with Mg and Si behaving oppositely to Al and Ti. However, these chemical changes cannot be confirmed with the results here. The corresponding interval in A1a displays a slightly darker contrast in BSE than the rest of the Al+Ti sector, but does not exhibit concentric zoning.

4.2.2 Concentrically zoned crystals: A1b and A2a

While crystals A1b and A2a do not exhibit sector zoning, they do display chemistries are similar to that of the sector zoning. As observed during optical microscopy, the bands have a very varying width (fig 9). In A1b, the width of zoning is different in different parts of the crystal. In the part of the crystal where the bands are the widest and the zoning is most distinguishable, the band widths range from approximately 10 μm to 70 μm , with some bands reaching up to 95 μm and 120 μm . Band widths in A2a also show great variation, however they do not reach the same thicknesses. Rather, the band width varies between approximately 10 μm to 80 μm , the most defined wide bands situated at the border between the irregular centre and the concentric zoning. Finally, the zoning varies between sharp and gradual compositional variations. (fig 10-11).

In both crystals, the zoning is chiefly observed

in Al and Ti; hence, Al is the most useful element when aiming to identify the zoning. The zoning is also visible in Mg and Si which behave oppositely to Al. The zoning is to some extent visible in Fe, however only in some instances where it can be seen to vaguely follow Al. Ca and Na show no relation to the zoning. What are common for all elements, however, are small internal variations on the scale of 5-15 μm , seen chemically and to some extent optically as well.

Due to the different elemental concentrations giving rise to the zoning, both crystals have varying chemistries. In A2a, two separate types of chemical compositions related to the zoning have been recognized. These are of similar chemical compositions to the Al+Ti and Mg+Si sectors in the sector zoned examples; however, both compositions have higher concentrations of Al and Ti compared to the Mg+Si sector in the sector zoned crystals. In the concentric zoning of A2a, one composition has a Mg# of ~77-79, while the other has a Mg# of ~74-77, and both have Al/Ti ratios of approximately 3.5-4.5. A1b does not exhibit two distinct chemical compositions. Rather, with Mg# of ~75.5-78, the different compositions of this zoning are more varied and less distinct from one another. The Al/Ti ratio, however, is the same as in A2a: ~3.5-4.5. For both crystals, the differences between the chemical compositions are generally smaller compared to the sector zoning. Similar to the sector zoning, however, Fe variations are irregular.

As mentioned in section 4.1, A1b and A2a are similar in that the concentric zoning is less pronounced in the centre of the crystal, and furthermore, in A2a the widest bands are generally located close to the centre. A2a is also overprinted in a certain part of the crystal, and this part is revealed to have a lighter BSE contrast. Finally, A1b is different from A2a in that it also possesses an irregularly shaped core with a different chemical composition than the rest of the crystal. In fact, with an Mg# of ~83 it is the highest Mg# observed in these clinopyroxene samples. Furthermore, the core also has the lowest measured Ti concentration, with an Al/Ti ratio of ~5.75.

4.2.3 Rims

Even though the four clinopyroxene crystals display different zoning and chemistry, they all have in common the chemical changes occurring at the rim. Using BSE imaging, a narrow light band close to the outer rim was observed in all four crystals. The edges of the rims are uneven and rather jagged, resulting in varying widths from the light band to the edge (fig 12). From the analysed sites however, the rims have been measured and estimated to be around 5-33 μm for A1a, 5-37 μm for A1b, around 15 μm for A2a and around 8-18 μm for A2b.

As shown by figure 13, the nature of this light band varies between different sites. Some sites were observed to exhibit two closely adjacent light bands and/or one wide band, some sites exhibit a single band and a few display what can be referred to as a “double rim” (fig 13). The frequency of two light bands seems to be higher in the concentrically zoned crystals, while the single bands tend to be present only in the sector

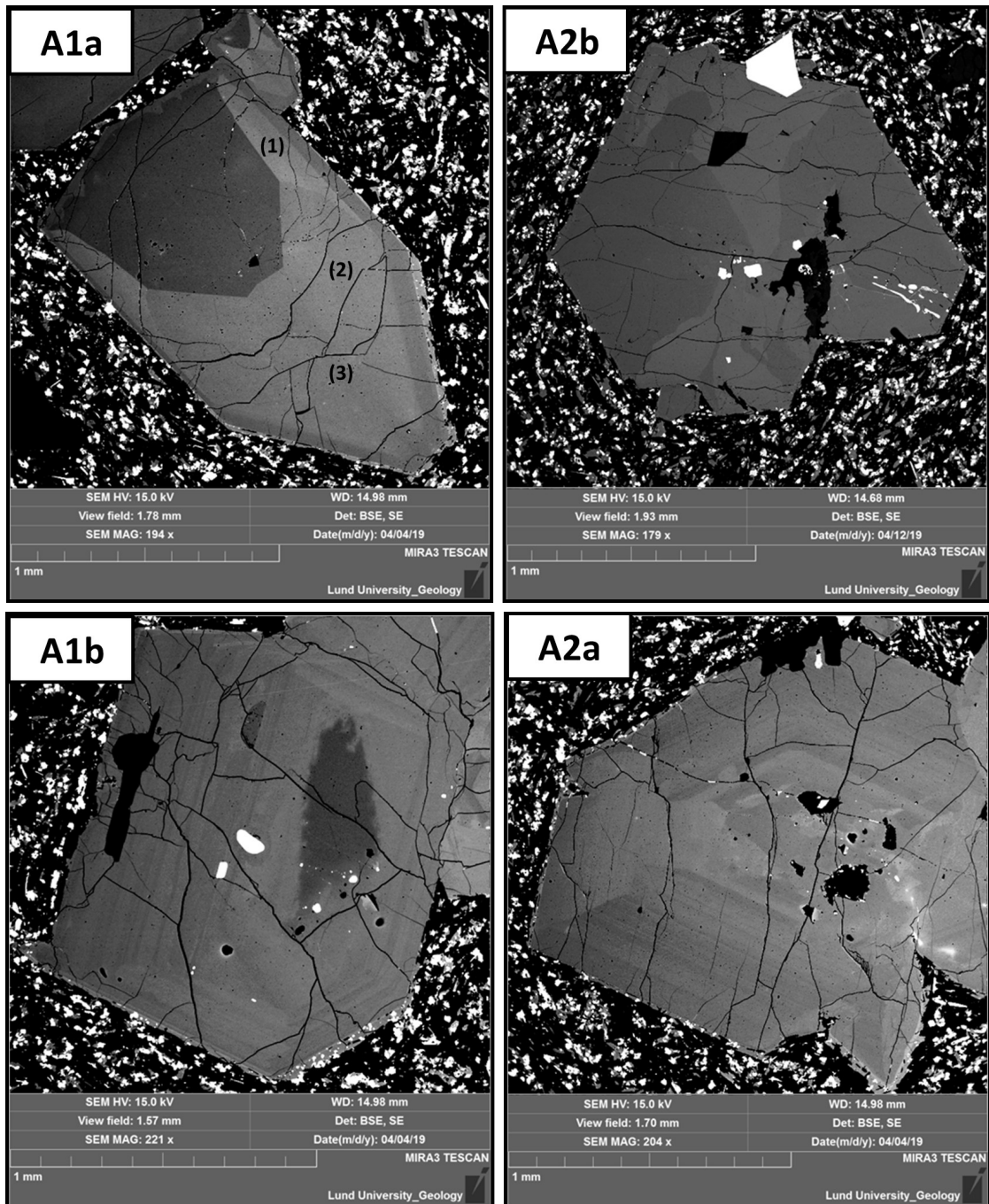


Fig 9: BSE images of sector zoned crystals A1a (upper left), A2b (upper right), A1b (lower left) and A2a (lower right). *Upper left:* The dark (Mg+Si rich) and light (Al+Ti rich) sectors are clearly visible in this crystal, as is the darker interval close to the rim and the subsectors. The subsectors are marked as (1), (2) and (3), with (1) being the lightest and (3) the darkest in contrast. The black inclusion in the Mg+Si sector is determined to be a plagioclase. *Upper right:* The dark and light sectors are clearly visible here as well, and in contrast to A1a, A2b displays two dark sectors. Also note the irregular zoning in the bottom part of the crystal, as well as the small dark area next in the upper left corner of A2b adjacent to the black plagioclase inclusion, which is part of the small pyroxene inclusion. The crystal also displays numerous opaque inclusions. *Lower left:* The concentric zoning can be observed as bands of alternating contrast, with wider bands in the left part of the crystal than in the right. The centre displays irregular zoning as well as a dark core. Furthermore, a large plagioclase inclusion can be seen close to the left rim, as well as opaque inclusions closer to the centre. *Lower right:* Similarly to A1b the bands here can be distinguished by contrast in BSE, however A2a is more symmetric. It also displays an irregular centre, but lacks a core. Also note the left part of the crystal that to some extent lacks zoning, as well as the plagioclase inclusion at the top of the crystal. The pictures are edited to display a higher contrast in order to more easily observe the zoning.

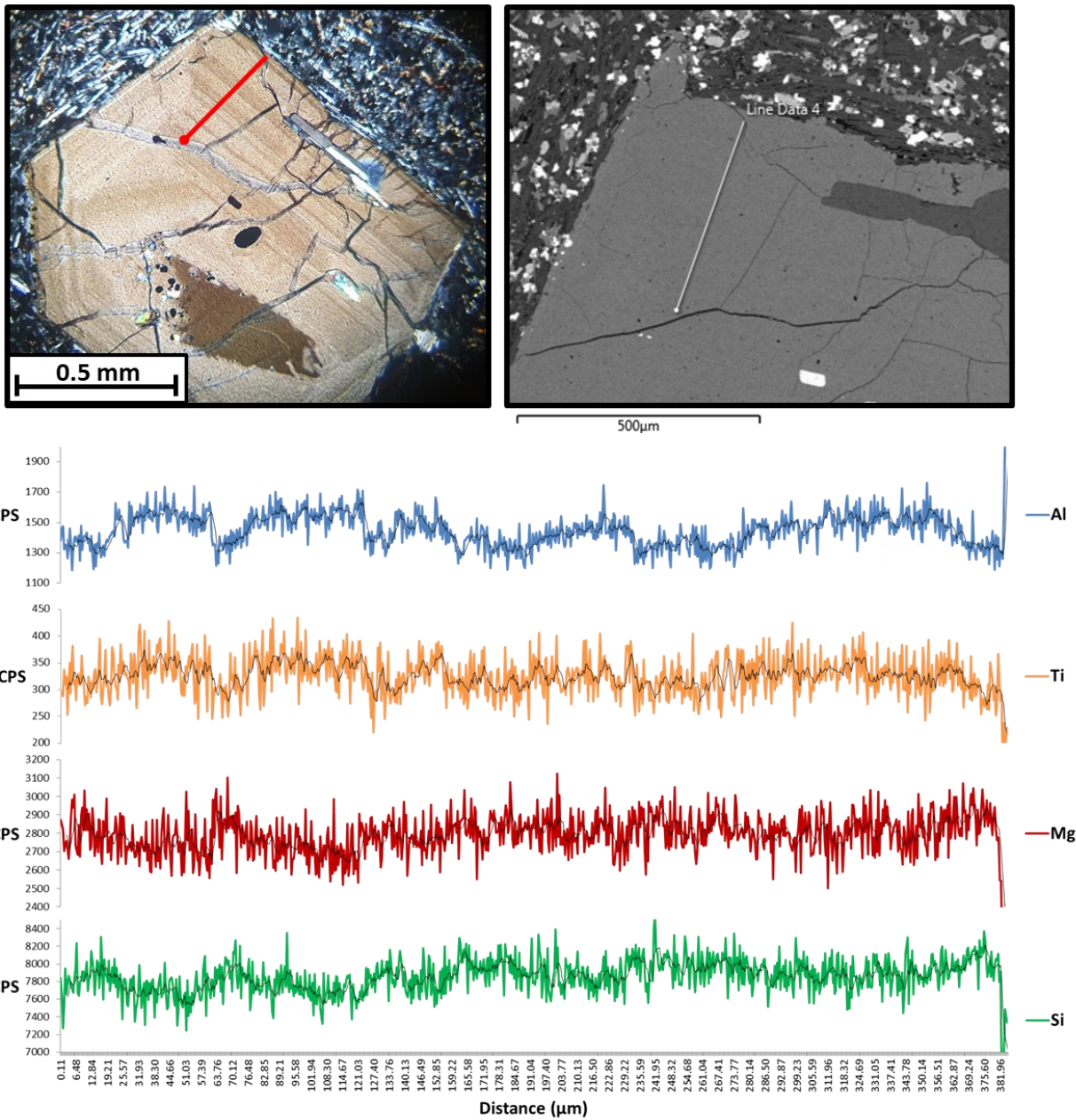


Fig 10: Chemistry of the concentric zoning in Al_{1b}, displaying variations in Al, Ti, Mg and Si plotted in CPS (counts per second). The line starts in the interior of the crystal (left part of diagram) and ends at the rim (right part of diagram), and the location of the line is shown in the upper pictures (red and white line respectively). The left is the Al_{1b} crystal under crossed polars in optical microscope, while the right is a BSE image. As can be seen in the diagrams Al shows clear variations between the zoning bands, displaying higher concentrations in the light bands under crossed polars. Ti follows the same pattern as Al, however not as pronounced. Furthermore, Mg and Si behave oppositely to Al. The lines are based on SEM-EDS line data presented in appendix E, table 1.

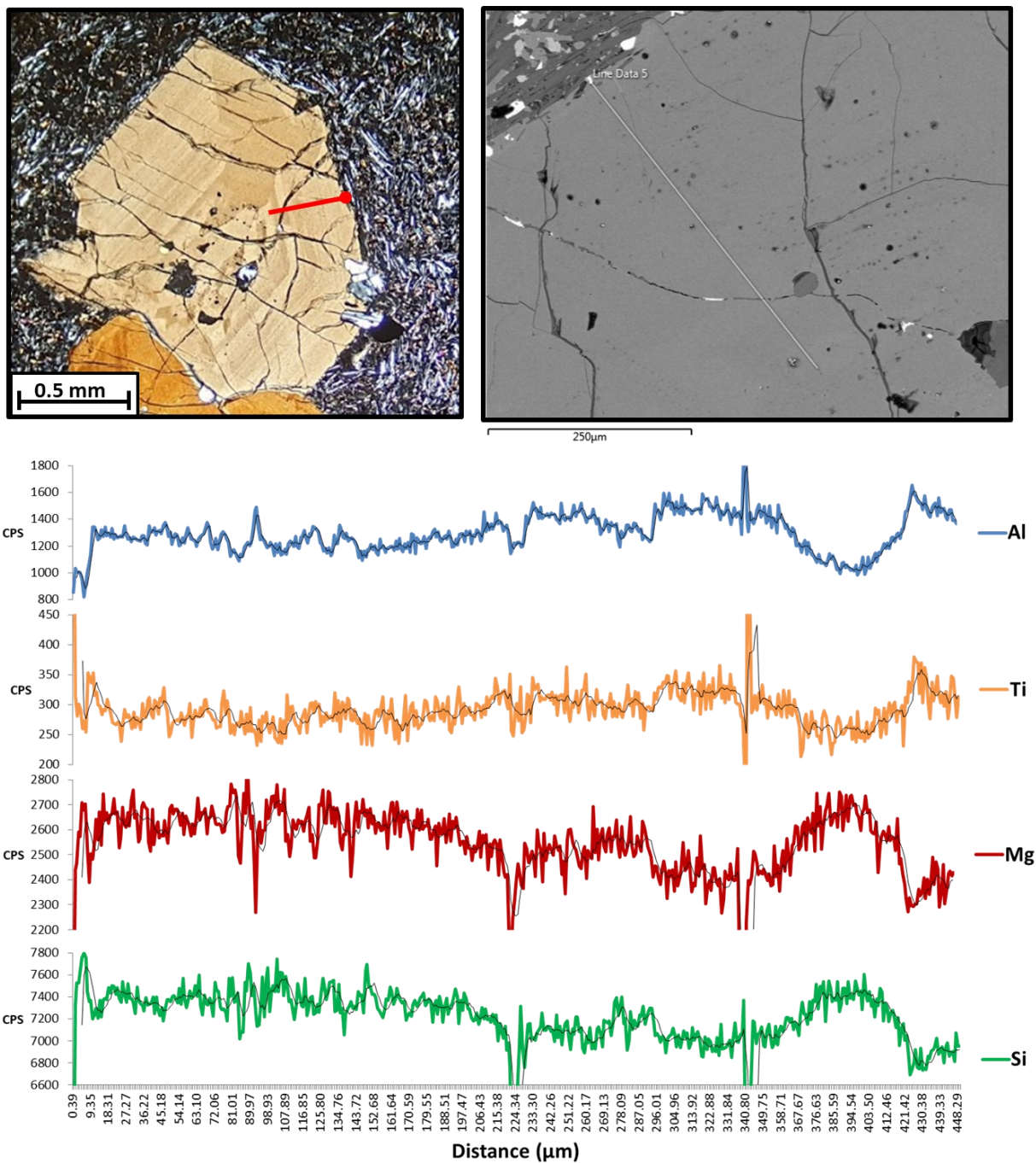


Fig 11: Chemistry of the concentric zoning in A2a, displaying variations in Al, Ti, Mg and Si and plotted in CPS (counts per second). The line starts in the rim (left part of diagram) and ends in the interior of the crystal (right part of diagram), and the location of the line is shown in the upper pictures (red and white line respectively). The left is the A2a crystal under crossed polars in optical microscope, while the right is a BSE image. Similar to in fig 10, Al shows clear variations between the zoning bands, displaying higher concentrations in the light bands under crossed polars. Ti follows the same pattern as Al, however not as pronounced. Furthermore, Mg and Si behave oppositely to Al. Note the generally higher Si concentrations towards the rim, correspondingly seen as a similar increase in Si and decreases in Al and Ti. Spikes in the graph due to fractures and impurities have not been taken into consideration when deciding the limiting values for the y-axis, in order to increase visibility of variations related to the zoning. The lines are based on SEM-EDS line data presented in appendix E, table 2.

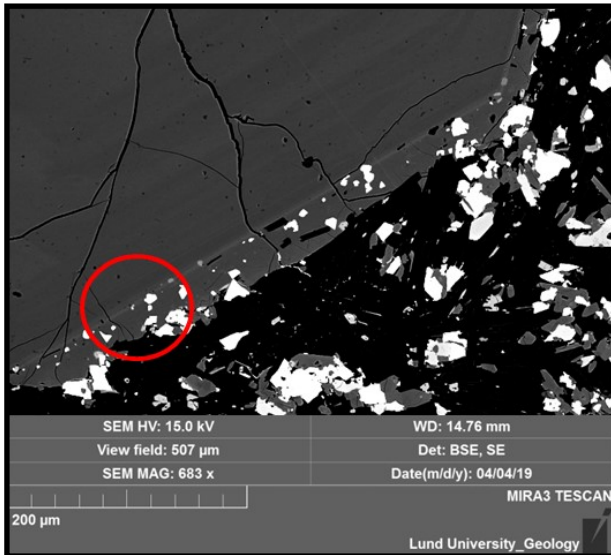


Fig 12: BSE image of the rim of A1b. Observe the jagged appearance of the rim, the light band, and how the rim inclusions seem to have started to crystallize simultaneous with the band. Two light bands in this crystal can be observed inside of the red circle. The picture is edited to acquire a higher contrast in order to more easily distinguish the compositional differences.

zoned crystals. Furthermore, the “double rims” were only observed in one face of the concentrically zoned crystal A1b.

The EDS-analyses show that the light band marks the start of extensive chemical changes (fig 14-15). Generally, the light band represents a chemical composition with higher Ti and/or Fe concentrations, after which a significant Al drop occur that lasts throughout the rim. In addition, in most sites of the concentrically zoned examples, an Al increase occurs before or during the sharp Al decrease. It is clear that the sites which exhibit single light bands display less complex chemical variations—characterized simply by a decrease in Al—than the sites which exhibit two light bands or “double rims” and is characterized by Al fluctuations, as shown in fig 14-15. Thus, the detailed variations are somewhat different between different sites. In fact, Al seems to behave differently at the band depending on the composition at that site. In the Mg+Si sectors, the Al drop seems to occur at the light band and continue throughout the rim. In contrast, in the Al+Ti sectors Al seem to stay the same or even experience a slight increase at the light band (not necessarily related to the Al increase observed in the concentrically zoned crystals), and the Al drop does not occur until outside of the light band. Additionally, some sites experiences a decrease of Mg and Si at the

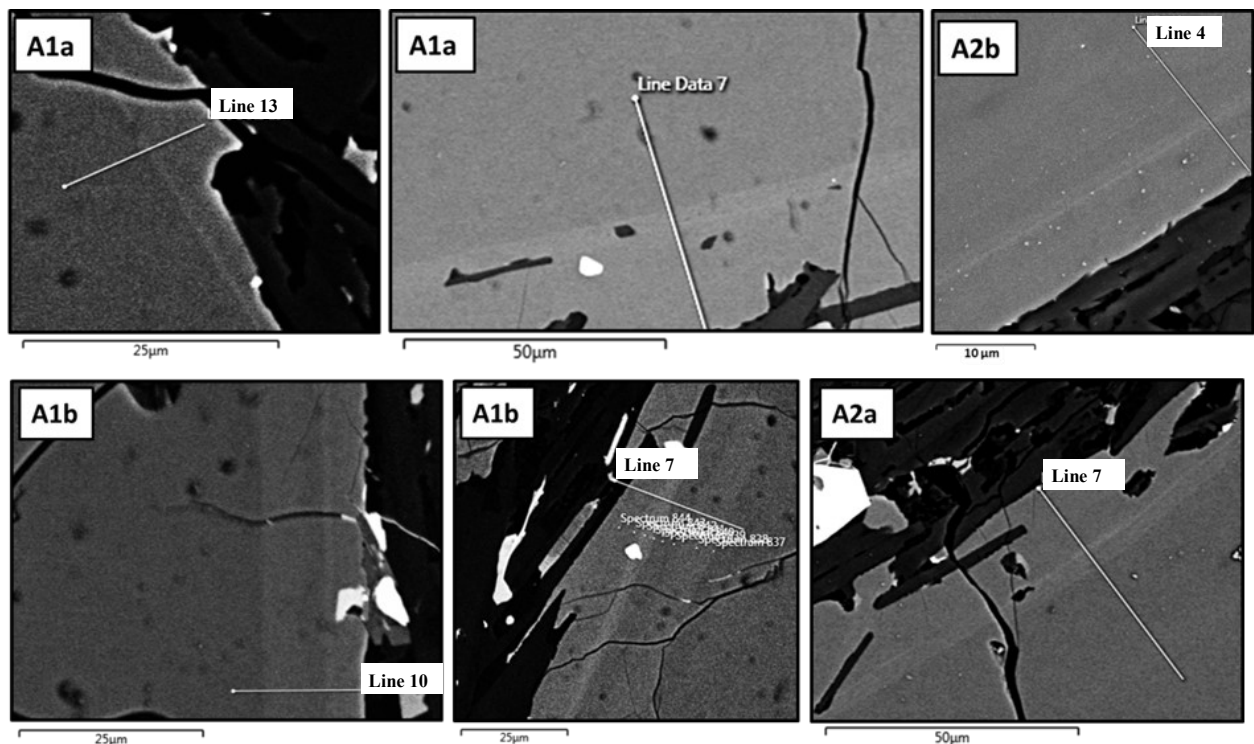


Fig 13: Different examples (BSE images) of the light band at the rims of the crystals. The upper row are examples from the sector zoned crystals (A1a and A2b), while the lower row are examples from the concentrically zoned crystals (A1b and A2a). While the appearance of the light band varies between different sites, some differences have been observed between the sector zoned and the concentrically zoned crystals. Comparing upper left corner (A1a) with lower left corner (A1b) illustrates this difference well, as A1a displays a single band while A1b rather displays a longer interval which is what in this thesis is referred to as a “double rim”. The same is seen in the lower middle example (A1b). Furthermore, site with two light bands seem to be more common in the concentrically zoned crystals; however the distinction between a single light band and two light bands is not unequivocal, and the light bands in upper middle and right corner (A1a and A2b) and the lower right corner (A2a) are difficult to evaluate. The lines marked on the images are presented in fig 14-15; however, upper middle line (A1a line 7) is omitted due to unreliable analyses.

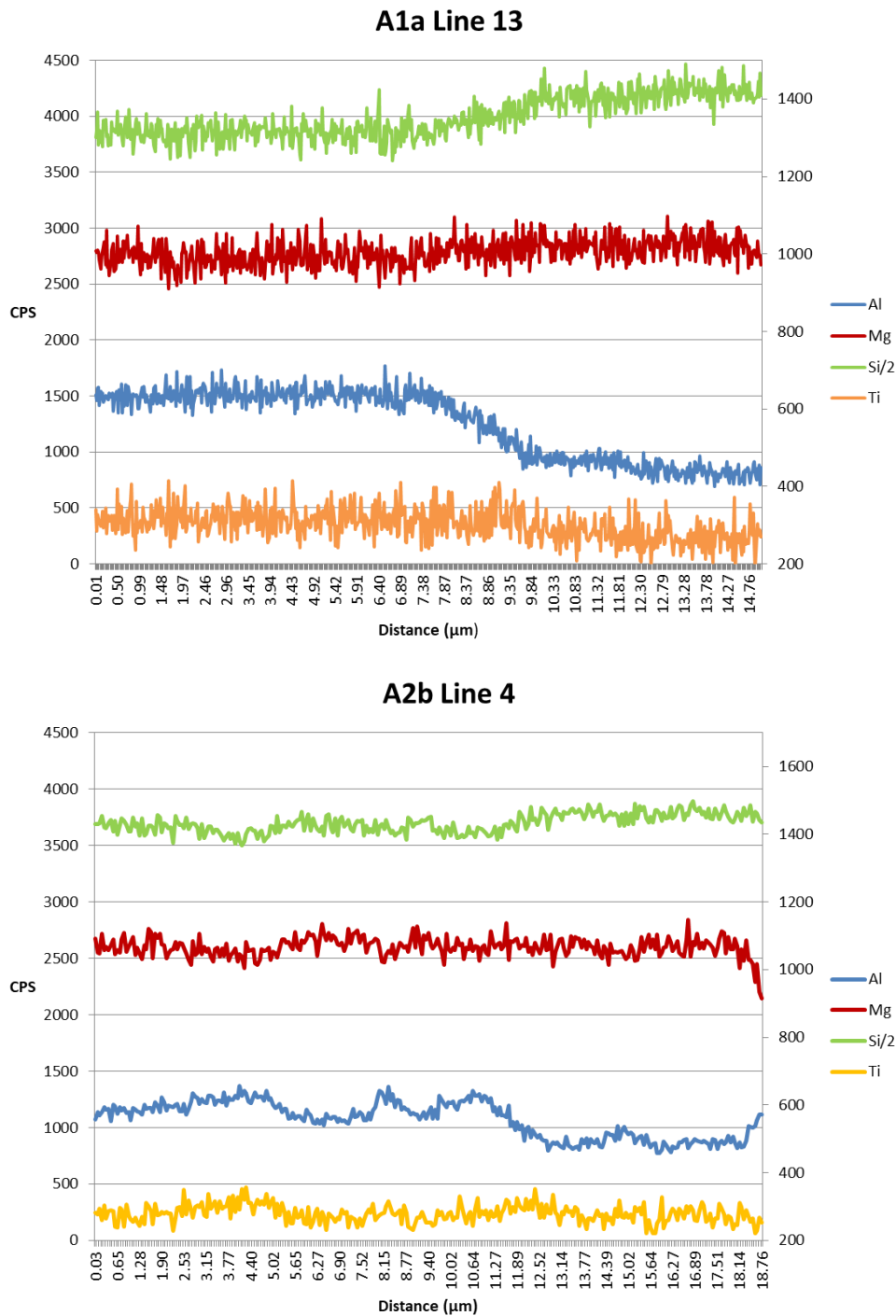
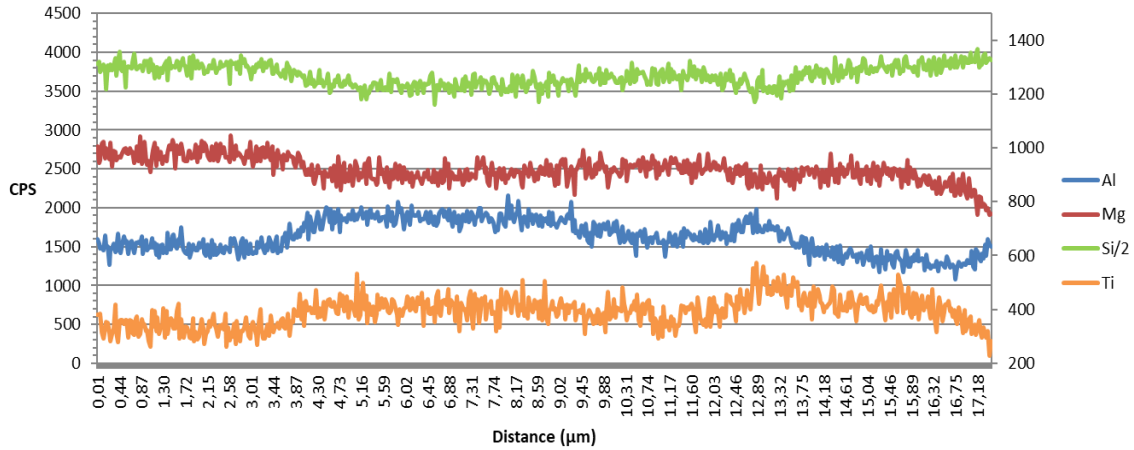
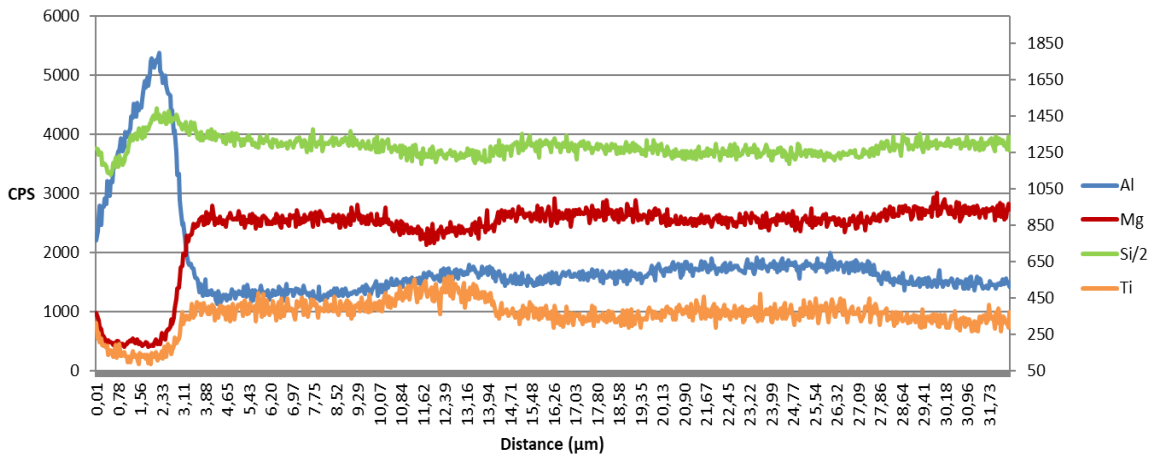


Fig 14: Graphs for the rims in the sector zoned crystals in fig 13 plotted in CPS (counts per second). In both graphs the rim is located to the right of the diagram. Note the simplicity of the chemical variations in A1a line 13 compared to A2b line 4 and the concentrically zoned crystals in fig 15, only exhibiting a steady Al decrease. A2b line 4 is more complex as can be expected due to the BSE image (fig 13). Here, the elements fluctuate before the Al decrease, and there is an additional Al increase after the decrease (at approx. 15 μm). Observe that Si is plotted at half concentration for illustrative purposes, and that Ti is plotted on the secondary axes to the right. The lines are based on SEM-EDS line data presented in appendix E, table 3-4.

A1b Line 10



A1b Line 7



A2a Line 7

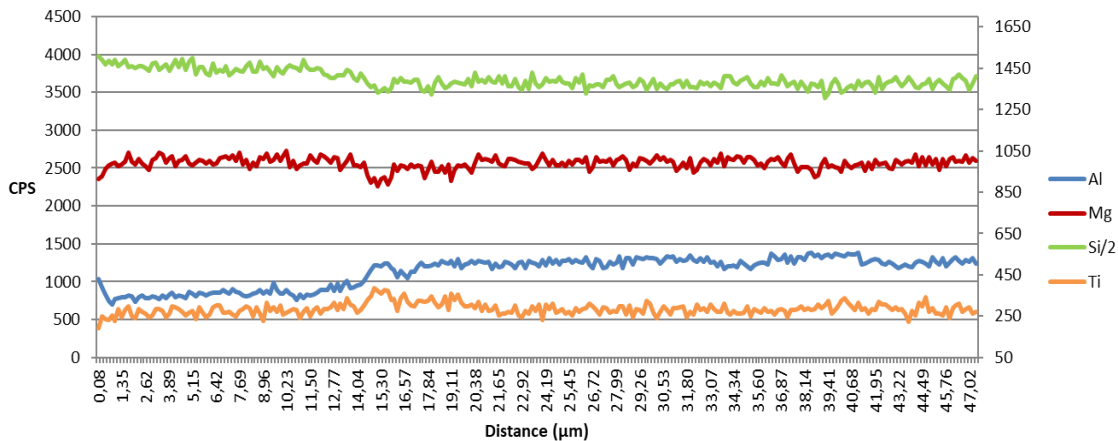


Fig 15: Graphs for the rims in the concentrically zoned crystals in fig 13 plotted in CPS (counts per second). In the upper graph the rim is located to the right in the diagram, while in the middle and lower graph the rim is located in the left of the diagram. A1b line 7 (middle diagram) goes some distance into the matrix which explains the compositional variation between 0 and 4 μm . Al, Mg, Si and Ti are plotted to illustrate the differences in behaviour between the elements. Note the increase in Al before the extensive Al decrease (at around 12 μm for the upper, 13 μm for the middle and 15 μm for the lower diagram). Also note that while Ti behaves similarly to Al, Si and Mg behaves oppositely. Observe that Si is plotted at half concentration for illustrative purposes, and that Ti is plotted on the secondary axis to the right. The lines are based on SEM-EDS line data presented in appendix E, table 5-7.

light band if Al experiences an increase, and a constant or increasing concentration of Mg and Si at the light band if Al decreases, essentially meaning that Mg and Si behave oppositely to Al. Furthermore, Fe only has a larger spike than Ti at the light band in sites where the Al drop occurs at the light band, rather than after.

Generally, the rims have Al/Ti ratios of ~2.0-3.0, with one value reaching as low as 1.83. Furthermore, the dark rims have a Mg# of ~73-77 while the light rims have a Mg# of ~70-74.

4.2.4 Comparison of chemical compositions and substitution relationships

Taking the results above into account, the different chemical compositions can be plotted into groups. These groups make a distinction between the chemistry of the Mg+Si sector and the Al+Ti sector of the sector zoned crystals, the rim of both sectors, as well as isolating the two compositions of the concentric zoning in A2a. Note, however, that due to the more varied nature of the chemistry of A1b it is not possible to distinguish two separate chemistries for this crystal. As mentioned, the Al/Ti ratio is generally similar when comparing the Mg+Si and Al+Ti sectors, with values of around 3-4.5 for both sectors in sector zoned crystals and the concentrically zoned crystals. Howev-

er, the plotting of Al against Ti (fig 16) makes it possible to distinguish between these compositions. By doing this, it is clear that five different chemical compositions are discernible. These are the Al+Ti sectors and Mg+Si sectors, which clearly have different chemistries; the rims which seem to correspond to Al-depleted versions of the sectors; and the A1b core which has the lowest concentration of Ti. Furthermore, one of the two compositions of A2a falls within the same range as the Al+Ti sector, while the other is intermediate between the two sectors, and A1b has compositions ranging between the two. The plot also illustrates the relatively stable Al/Ti ratio, as the different compositions plot in a linear fashion despite varying Al and Ti concentrations. The distinction between these different chemical compositions is also apparent in when comparing for example (Al+Ti) against (Mg+Si) and Mg against Fe (see appendix C fig 2).

Fig 17 describe possible substitution relationships between different elements. A negative linear relationship is seen between Al and Si and between Ti and Mg. A negative correlation is also seen between Mg and Fe, and Fe+Mg for all measurements equals to a sum between 0.92 and 1.02. Additionally, positive correlations are discernible when plotting Ti against Fe and Mg against (Mg+Si).

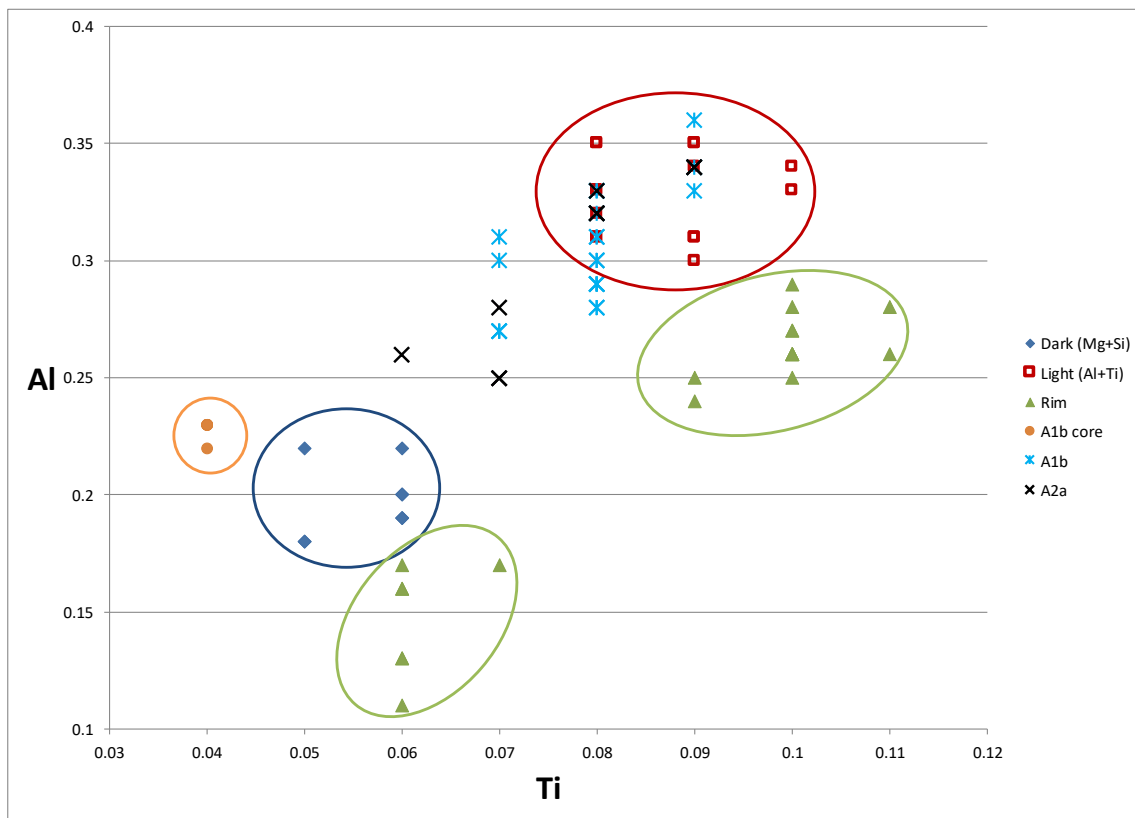


Fig 16: Plot of Al against Ti (cations) reveal five distinct groupings of chemical compositions: the in BSE light Al+Ti sectors (red squares), dark Mg+Si sectors (dark blue diamonds), rims (upper and lower green triangles) and the A1b primitive core (orange circles). The light and dark sectors are represented by compositions collected from both phenocryst A1a and A2b, while the rims represent all four phenocrysts. A1b and A2a are plotted separately, using light blue stars and black crosses respectively, and represents the varying chemical composition of these concentrically zoned phenocrysts. Note the coincidence of the light sector, A1b and A2a at Ti = 0.08 and Ti = 0.09, and the linear fashion in which the different compositions are plotted.

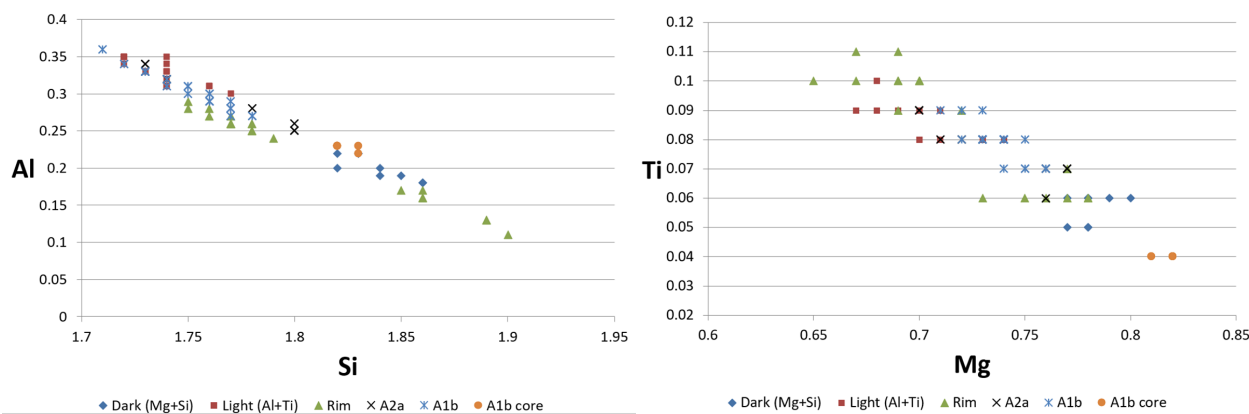


Fig 17: Two examples of possible substitution relationships. The plots illustrate the relationships between Al and Si (left) and Ti and Mg (right). All concentrations are plotted in cations. Both plots display a negative linear trend. Additionally, in the Ti-Mg plot the residual core in A1b is compositionally isolated from the other chemical spectrums.

4.2.5 Inclusions and matrix crystals

As inferred in section 4.1, inclusions are common occurrences in these crystals. These inclusions are to be found both in the interior of the crystals and in their rims, especially numerous between the light band and the edge. The inclusions are mostly plagioclase and iron oxides. The plagioclase inclusions are fairly rich in Ca and poor in K, ranging from labradorite to bytownite composition. The plagioclase inclusions situated in the interior of the crystals has lower Ca concentration and are therefore of bytownite composition, while the plagioclase inclusions in the rim have higher Ca concentrations and can be classified as labradorites. Plagioclase crystals in the matrix are of similar composition, however spikes of K and Na in some crystals create compositions more in line with alkali feldspar. Additionally, nepheline has been observed in the matrix.

The iron oxides are chiefly represented by titanium magnetites and ilmenites. The iron oxides in the interior of the crystals are above all titanium magnetites; however, ilmenites in the crystals do occur as well.

4.3 Electron backscatter diffraction analyses (EBSD)

EBSD analyses were performed to determine the orientation of the mineral in the thin section by viewing so called Kikuchi patterns, created by backscatter electrons, and identifying the zone axes. The results of the EBSD analyses on crystal A1a are presented in fig 18. The results indicate that the crystal is oriented at an angle towards the c-axis. Additionally, the angle of the c-axis is slightly different between the two twins which is consistent with the fact that the two twins have different extinction angles (see additional maps in appendix C fig 3).

4.4 Laser ablation inductively coupled plasma mass spectrometry LA-ICP-MS

The trace element data received from the LA-ICP-MS analyses reveal that the transition metals V, Ni, Sc and

Co are among the trace elements with highest concentrations out of the elements analysed (Cr belongs to this group as well but will be discussed in detail in section 4.4.5). Along with the transition elements, the HFS element Zr and the LIL element Sr also display high concentrations relative to other elements. Furthermore, REEs with even atomic numbers generally have higher concentrations than similar REEs with odd atomic number, and lighter REEs generally have higher concentrations than heavier REEs. As follows, Ce and Nd generally have higher concentrations than La and Pr, and the heavy element Yb has the lowest concentration of all REEs. Finally, Y and Hf have intermediate concentrations while the highly incompatible Nb and Ba have very low concentrations. In fact, the concentration of Ba was measured to be below the detection limit (~0.8 ppm) in all of the spot analyses.

For complete data from the LA-ICP-MS spot analyses the reader is referred to appendix F.

4.4.1 Sector zoned crystals: A1a and A2b

As sector zoning is present in most of the analysed trace elements, the observations above are translatable to the zoning of A1a and A2b. In fact, the elements with higher concentrations are the ones which clearly display zoning (fig 19, table 3). As a result, sector zoning of REEs is predominantly visible in lighter REEs with even atomic numbers (Ce, Nd, Sm, Gd, Dy), less so in REEs with odd atomic numbers (La, Pr, Eu), and slightly visible or absent in the heavy REEs Er and Yb. All zoned REEs exhibit higher concentrations in the Al+Ti sectors than in the Mg+Si sectors. The transition metals behave similar to the REEs in that sector zoning is visible in V and slightly visible in Sc, both of them increasing in the Al+Ti-sectors. Zoning is however not visible in Cr, Ni or Co. Furthermore, zoning is also visible in Sr, Zr and Hf, and occasionally in Nb and Ba, all of which are also increasing in the Al+Ti-sectors.

According to the spot analyses (table 3), the increase of the zoned trace elements in the Al+Ti sector ranges from a few ppm to over a hundred ppm, as is the case for e.g. V. The relative change typically lies

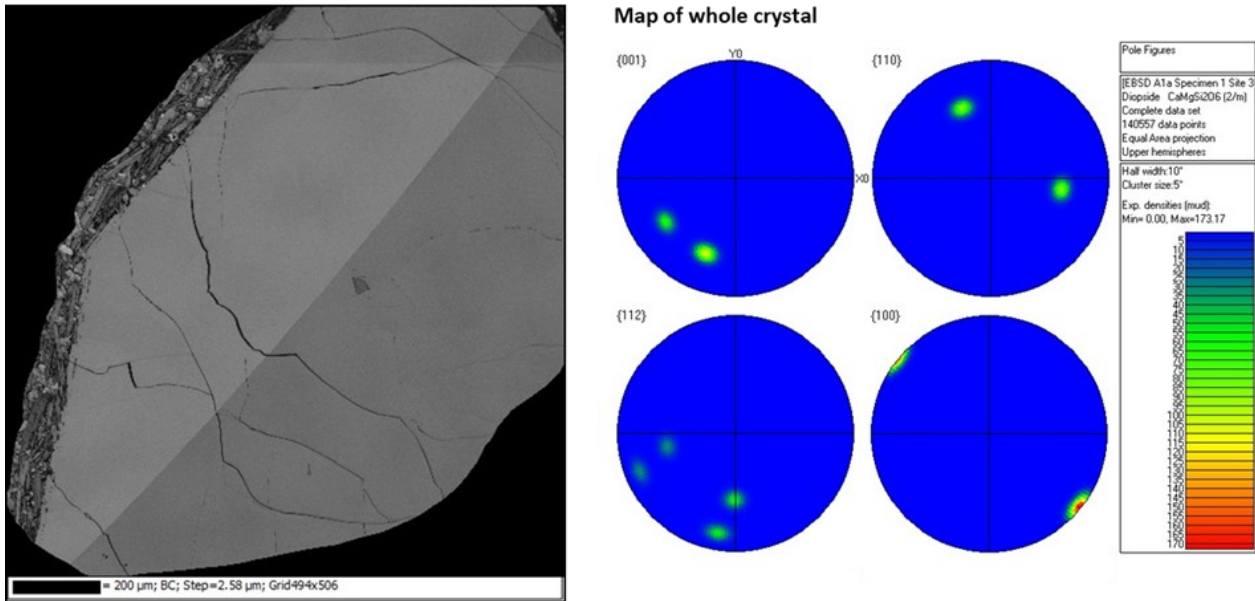


Fig 18: EBSD results for crystal A1a. The pole figures make clear that there is a slight difference in crystallographic orientation between the two twins, as is also evident by the difference in contrast in the left picture.

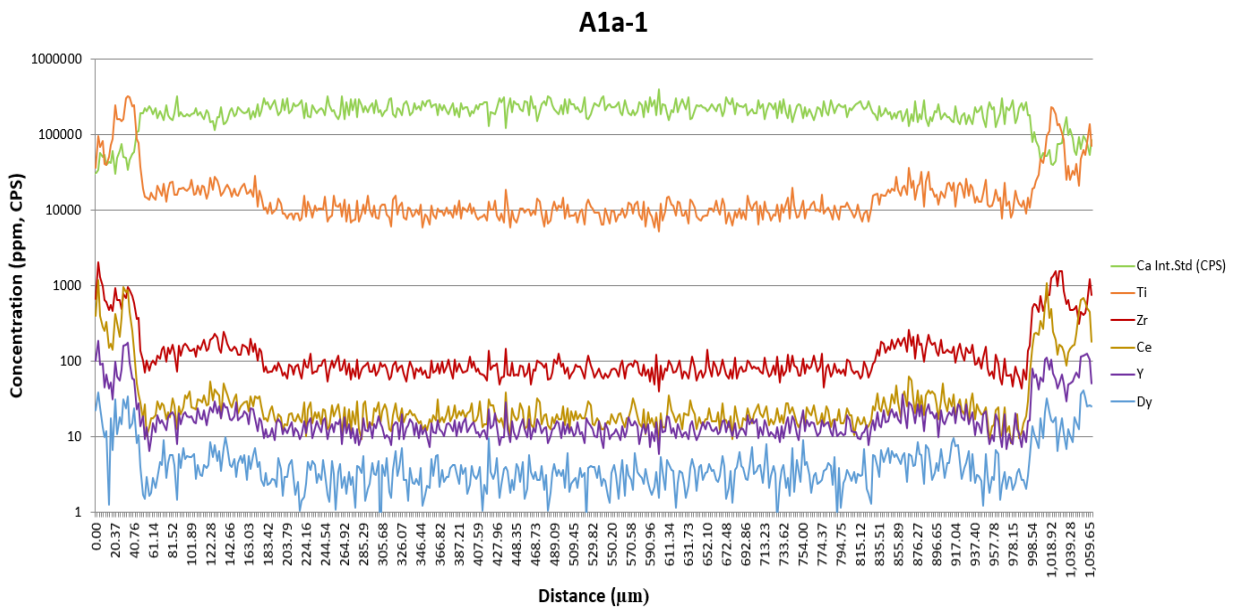


Fig 19: Sector zoning is visible in most elements. Here, Ti, Zr, Ce, Y and Dy (plotted in ppm) have been chosen to illustrate the zoning of line A1a-1. The green line (top) represents Ca (internal standard) plotted in CPS (counts per second). Where the Ca-line goes below 100 000 CPS can be regarded as the edge of the crystal. Note the border between the sectors at ca. 180 μm and 820 μm, and the lower concentrations of the elements between these borders, representing the Mg+Si sector. Also note that Cr spikes are present close to the rims (not included in this graph), thus perhaps affecting the concentrations of these elements in the Al+Ti sector at this site.

between 1 and 2 times the concentrations of the Mg+Si sector (see appendix C table 2 for data regarding the A2b crystal).

4.4.1.1 Relative partition coefficients between sectors

The relative partition coefficients calculated for the A1a Mg+Si sector is presented in appendix C table 2 as average and median partition coefficients calculated from A1a-1, and as partition coefficients calcu-

lated from A1a-spot-1 and A1a-spot-2. The results indicate that most elements are less compatible in this sector (fig 20). One clear exception of this is Yb, which displays higher partition coefficients in the Mg+Si sector. Another notable exception is Eu, which also displays slightly higher partition coefficients in this sector. Furthermore, the REEs Ce, Pr, Nd and Sm are estimated to have very similar partition coefficients in both sectors.

Table 3: The difference in trace element concentrations between the Al+Ti and the Mg+Si sector in A1a. The “visible change” column refers to the graphical estimation of the change. The concentrations are based on spot analyses of A1a-spot-2 (Al+Ti) and A1a-spot-1 (Mg+Si). The “difference” column to the right is colour coded, with green representing an increase and red a decrease, and refers to the difference between the sectors, as calculated with $Difference = C(Al+Ti) - C(Mg+Si)$. Most trace elements are enriched in the Al+Ti sector relative to the Mg+Si sector with exception for Co and Ni. Cr was excluded from the graphical estimation due to the interference of Cr spikes, and Ba is below the detection limit (LOD) and can therefore not be evaluated.

A1a				
Element	Visible change (graph)	Al+Ti sector (ppm)	Mg+Si sector (ppm)	Difference (ppm)
La	Increase	9.12	5.12	4
Ce	Increase	30.7	19.4	11.3
Pr	Increase	5.46	3.4	2.06
Nd	Increase	28.7	18.31	10.39
Sm	Increase	8.42	5.23	3.19
Eu	Increase	2.72	1.71	1.01
Gd	Increase	9.28	5.68	3.6
Dy	Increase	6.87	4.21	2.66
Er	Increase	2.83	1.74	1.09
Yb	Increase	1.56	1.18	0.38
Cr	<i>(omitted)</i>	51.6	37.2	2.06
Ni		121.8	126	-4.2
Co		39.4	42	-2.6
Ti	Increase	14280	10240	4040
V	Increase	390	287	103
Sc	Increase	110.9	98.6	12.3
Zr	Increase	167.5	109.9	57.6
Sr	Increase	87.7	74.5	13.2
Y	Increase	27.3	17.55	9.75
Hf	Increase	6.91	4.97	1.94
Ba	Increase	<i>Below LOD</i>	<i>Below LOD</i>	
Nb		1.126	0.54	0.586

4.4.2 Concentrically zoned crystals: A1b and A2a

Variations across the concentric zoning are seen in most trace elements (fig 21). Specifically, in A1b where the zoning is the widest, the LREE La, Ce, Pr and Nd display regular zoning on the scale of approx. 25-45 μm , with peak concentrations of approx. 2-3 times the concentration at the base level. For other trace elements, however, zoning is less regular and therefore problematic to evaluate. There is also no clear connection between that and the zoning of Al.

What is easier to evaluate is the chemistry of the core in A1b (table 4). All REEs decrease relative to the surrounding clinopyroxene composition, with Er

and Yb showing a slightly less clear decrease than the other elements. Out of the transition metals, Sc exhibits no change while V and Co both decrease in the core. So does Zr, Y, Hf and Sr, while Ba and Nb display no difference. In contrast to the other trace elements, both Ni and Cr show an increase in the core, reaching concentrations of approx. 240 ppm for Ni and 5400 ppm for Cr. This Cr concentration corresponds to 18 times the Cr concentration of the surrounding clinopyroxene composition and a liquid composition at the time of crystallization of ca. 1420 ppm (see appendix C fig 4)

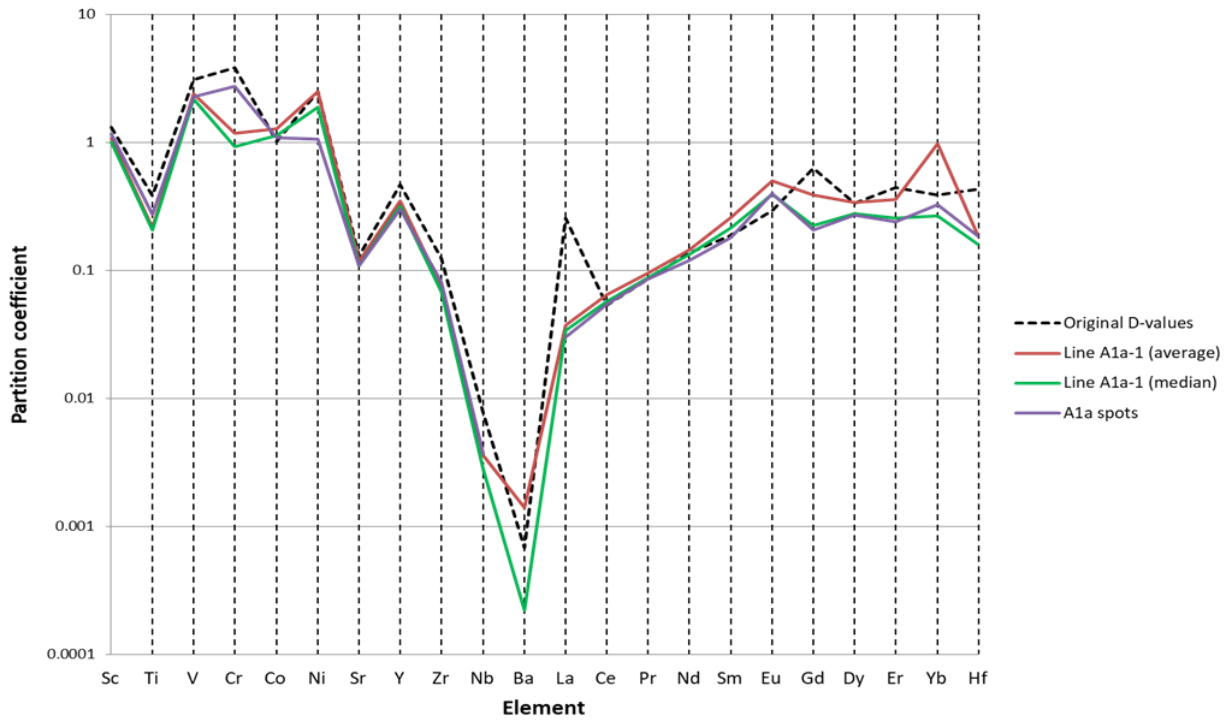


Fig 20: The calculated partition coefficients for the Mg+Si sector. The dashed line represent the values used to represent the Al+Ti sector, and the red, green and purple lines represent the average values from the A1a- line, the median values from that line, and the values calculated from the spot analyses of A1a. As can be deduced from the graph, most elements are estimated to have lower relative partition coefficients in the Mg+Si sector than the Al+Ti sector. Notable exceptions are Yb, Eu and Ce, Pr, Nd and Sm.

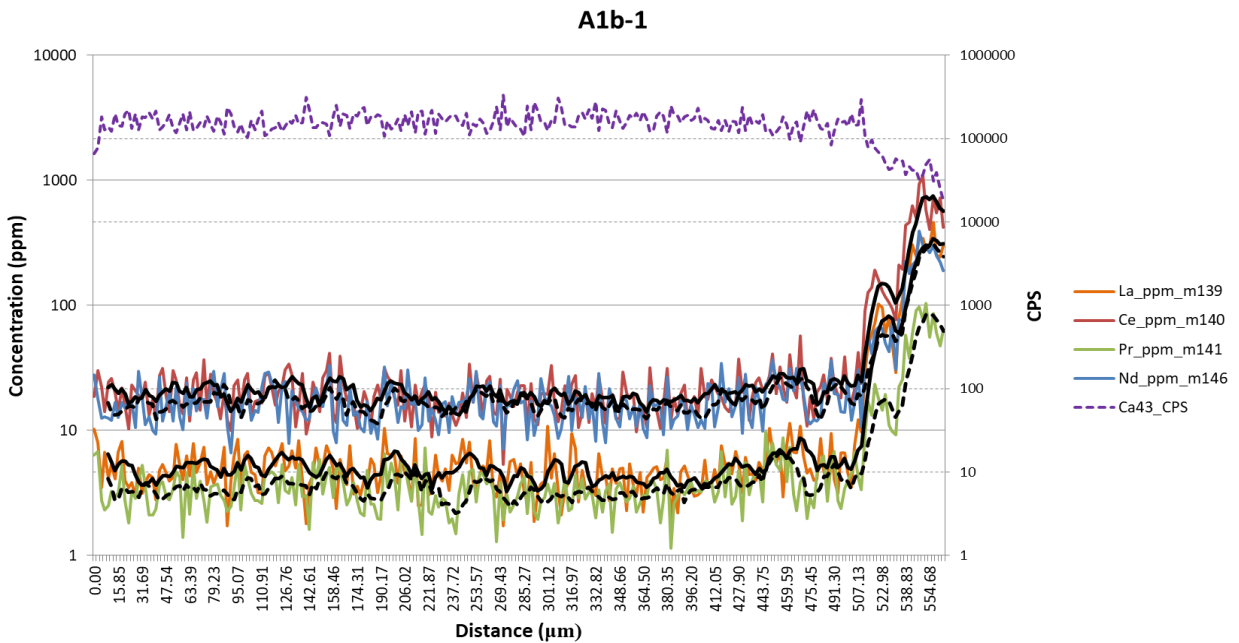


Fig 21: Graph showing the fluctuations of LREEs La, Ce, Pr and Nd over the concentric zoning in A1b. All four elements are plotted with a moving average of 5, meaning that the average of 5 points is plotted as one (black lines) to facilitate viewing of the chemical variations. If viewed without colour: Lower dashed black line represents Pr, lower solid black line represents La, upper dashed black line represents Nd and the upper solid black line represents Ce. The dashed purple line represents the internal standard Ca plotted in CPS (counts per second) on the right y-axis. Ca >100 000 CPS represents the clinopyroxene crystal, while Ca <100 000 indicate matrix signals. As can be seen in the graph, all four LREEs variate throughout the line in a similar fashion on a scale of approx. 25-45 µm.

4.4.3 Rims

Due to the changes of the major and minor elements in the rims it is reasonable to assume that the trace elements are affected as well. The results show an increase of incompatible elements (REEs, Sr, Nb, Hf, Y, Zr and Ba) in or outside of the rims, an increase that seems to be more pronounced in highly incompatible elements, for example Nb, than less incompatible elements. Additionally, Eu increases slightly less than other similar elements.

In contrast to the incompatible elements, ele-

ments with higher partition coefficients seem to behave differently. Sc and Cr both decrease in the rims, and Ni, Co and V all decreases, increases or stay constant depending on the site.

4.4.4 Liquid composition: Ratios and trends

Similar to the major elements described in section 4.2.1, the sector zoned crystals are relatively homogeneous in the core-to-rim direction regarding trace elements. Same is suggested for the concentrically zoned

Table 4: The difference in trace element concentrations between the A1b core and the composition outside of the core. The “visible change” column refers to the graphical estimation of the change. The concentrations are based on spot analyses of A1b-spot-1 (core) and A1b-spot-2 (surrounding). The “difference” column to the right is colour coded, with green representing an increase and red a decrease, and refers to the difference in concentration as calculated with $Difference = C(core) - C(outside\ of\ core)$. Most trace elements are depleted in the core relative to the rest of the clinopyroxene. The exceptions are Cr, Ni and Co. Ba is below the detection limit (LOD) and can therefore not be evaluated.

A1b core				
Element	Visible change	Core (ppm)	Outside of core (ppm)	Difference (ppm)
La	Decrease	2.12	4.62	-2.5
Ce	Decrease	8.49	18.06	-9.57
Pr	Decrease	1.566	3.13	-1.564
Nd	Decrease	7.87	16.56	-8.69
Sm	Decrease	2.4	5.08	-2.68
Eu	Decrease	0.905	1.86	-0.955
Gd	Decrease	2.56	4.84	-2.28
Dy	Decrease	1.88	3.53	-1.65
Er		0.69	1.31	-0.62
Yb		0.43	0.89	-0.46
Cr	Increase	5390	301	5089
Ni	Increase	240.3	139.9	100.4
Co		35.8	34.6	1.2
Ti	Decrease	7620	16300	-8680
V	Decrease	245.4	349	-103.6
Sc		81.6	84.9	-3.3
Zr	Decrease	33.8	100.6	-66.8
Sr	Decrease	74.8	94.4	-19.6
Y	Decrease	7.96	15.53	-7.57
Hf	Decrease	1.78	4.75	-2.97
Ba		<i>Below LOD</i>	<i>Below LOD</i>	
Nb		0.282	0.779	-0.497

crystals, as they do not display any clear core-to-rim trend apart from the concentric zoning. However, line A1a-1 displays some variation in REEs in the Al+Ti sector, with an increase followed by a decrease towards the rim (see appendix C fig 5). The same is seen in Zr, Hf and Y. This variation is not seen in any of the other clinopyroxene crystals.

Plotting of Sr/Nd and Eu/Sm ratios of the calculated liquid compositions (hereafter indicated with *(liq)*) show no common trend in the core-to-rim direction. In line A2a-1, Sr/Nd_(liq) decreases slightly towards the rim, while it shows a slight increase towards the rim in A1a-5. The La/Yb_(liq) ratio shows variation in the core-to-rim direction, especially prominent in the concentric zoning of A1b, however it does not display any general trend towards the rim.

4.4.5 Cr spikes

Of the nineteen lines that were analysed with LA-ICP-MS, sixteen displays some kind of Cr spike or increase (fig 22, table 5). One of the lines without Cr spike was taken in the concentrically zoned crystal A2a, and the remaining two were taken in the sector zoned crystal A2b.

4.4.5.1 Sector zoned crystals: A1a and A2b

In the sector zoned crystals, all of the observed spikes occur close to the rim. A1a displays large spikes in all analysed rims (lines A1a-1 - 5), with Cr concentrations increasing between 800 and 1400 ppm at the spike, resulting in spikes that have peak concentrations of 5 to 35 times the base level concentration. Two of the spikes (A1a-2 and A1a-5) show a rather protracted trend, while the other spikes are sharp. By correlating with the internal standard, the sharp spikes are estimated to be located between 25 µm and 40 µm from the edge of the crystal. For the more protracted spikes it is naturally more difficult to pinpoint an exact value, however the range seem to be 30-65 µm for A1a-2 and 65-265 µm for A1a-5. Finally, line A1a-1 exhibit a Cr spike seemingly located in the matrix that coincides with a Co spike.

A2b only displays spikes in two of the analysed rims of the crystal (A2b-2 and A2b-3), both located approx. 20 µm from the edge of the crystal. Both spikes show a smaller increase than the spikes in A1a, i.e. 75 ppm and 90 ppm respectively. However, the general Cr concentrations of A2b is lower than that of A1a, meaning that the relative increase of the A2b spikes are 8.5 and 10 times the base level concentra-

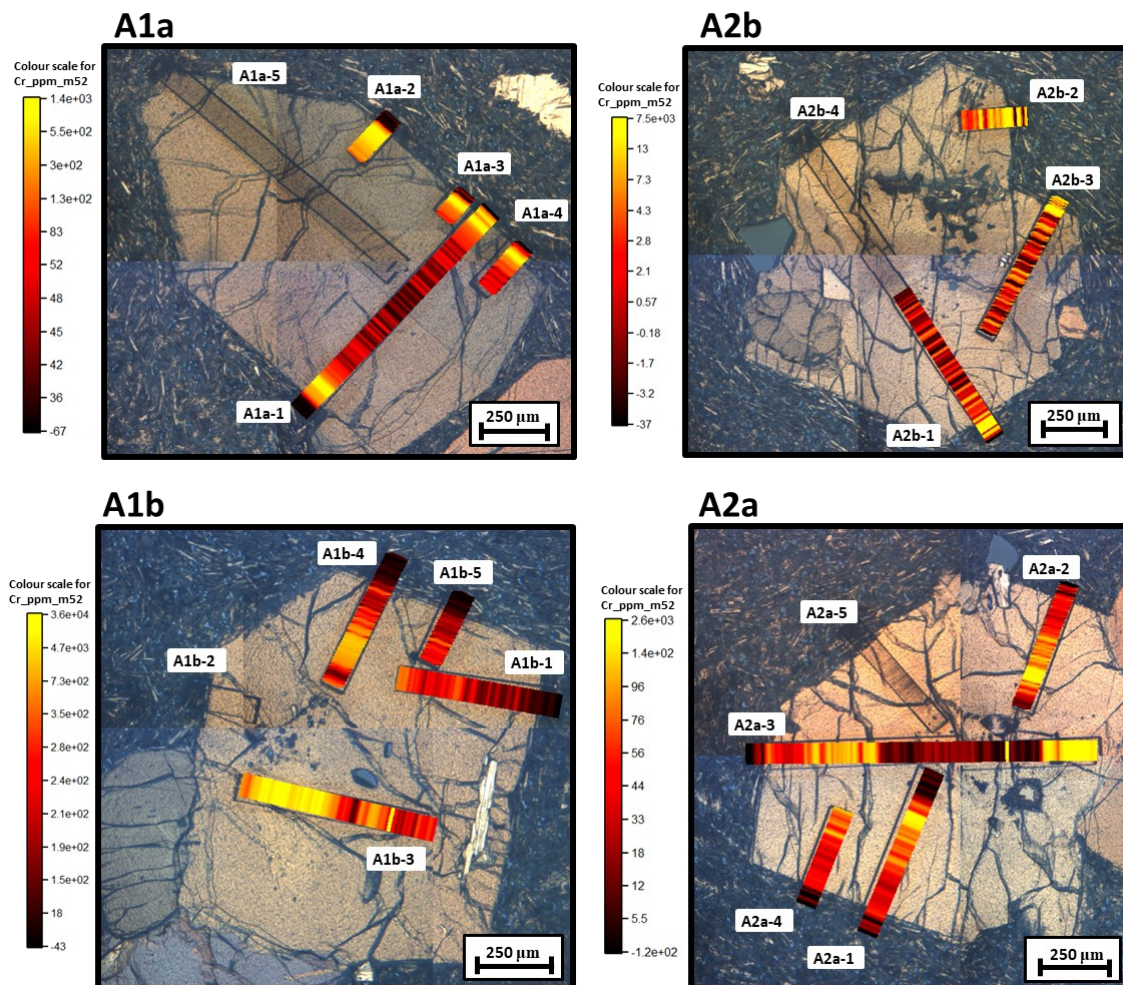


Fig 22: Cellspace images of the Cr concentrations in the lines analysed with the LA-ICP-MS technique. Note the high Cr concentration of the A1b core (A1b-3), as well as the consistent location of the spikes in A1a. Also take note of how a Cr spike seems to be located outside of the clinopyroxene crystal in line A2b-1. A few lines were excluded when producing the cellspace images due to fault of software.

Line	Spike rim	Spike interior	No spike	"Size" of spike (lowest-highest ppm)	Ni increase at spike	Comments
A1a-1	x			40-1000, 960 ppm, 25-fold // 40-1400, 1360 ppm, 35-fold	No	Two spikes, one for each rim.
A1a-2	x*			200-1000, 800 ppm, 5-fold	Slight	*No sharp spike, but a more protracted one. Larger variation of Ni during spike.
A1a-3	x			100-1000, 900 ppm, 10-fold	No	Ambiguous true base level concentration.
A1a-4	x			50-1000, 950 ppm, 20-fold	No	
A1a-5	x			100-1500, 1400 ppm, 15-fold	No	Somewhat protracted.
A1b-1			x**	100-550, 450 ppm, 5.5-fold	No	**No spike, however two Cr increases. Gradual decrease towards rim.
A1b-2		x		250-1500, 1250 ppm, 6-fold	No	Gradual decrease after spike.
A1b-3		x		200-2000, 1800 ppm, 10-fold	No	
A1b-4		x		300-3300, 3000 ppm, 11-fold	Yes	Gradual decrease after spike, tiny "spike" closer to rim.
A1b-5		x***		250-600, 350 ppm, 2.4-fold	No	***Tiny "spike" part of a gradual decrease.
A2a-1		x		50-500, 450 ppm, 10-fold	Yes	Followed by a gradual decrease. Small increase at rim.
A2a-2		x		50-600, 550 ppm, 12-fold	Slight	Slight increase of Ni. Gradual decrease of Cr towards rim.
A2a-3		x****		20-1000, 980 ppm, 50-fold	Yes	****Long line. Big spike in middle of phenocryst accompanied by increase of Ni. Increase of Cr further out (20-200 ppm, 10-fold) gradual decrease, without a preceding spike, and small increase at rim.
A2a-4			x		Yes	Slightly higher Cr concentrations in interior (50-150 ppm, 3-fold), including a tiny "spike". Gradual decrease as in the other lines.
A2a-5		x		50-750, 700 ppm, 15-fold	Yes	Gradual decrease towards rim.
A2b-1			x			Increase outside of rim.
A2b-2	x*****			10-85, 75 ppm, 8.5-fold	No	*****Small spike just inside rim. Some other signs of spikes outside of rim too. Generally very low Cr-concentrations.
A2b-3	x*****			10-100, 90 ppm, 10-fold	No	*****Small spike just inside rim. Very low concentrations.
A2b-4			x			Some increase towards rim, but no spike

Table 5: The occurrence, nature and size of the Cr spikes that were recorded during the LA-ICP-MS analyses. While the spikes in the sector zoned crystals are located in the rim, the spikes in the concentrically zoned crystals are located in the interior of the crystal. These crystals also display a gradual decrease across the concentric zoning towards the rim.

tion respectively, similar to the spikes in A1a. Finally, the other two lines (A2b-1 and A2b-4) seem to record a slight increase of Cr in the rim, however a Cr spike does not occur until in the matrix just outside of the crystal. Furthermore, the Cr concentrations in these lines seem to increase slightly over the concentric zoning.

4.4.5.2 Concentrically zoned crystals: A1b and A2a

While the Cr spikes in the sector zoned crystals occur at the rim, the large spikes in the concentrically zoned crystals occur in the interior of the crystal. Judging from the placement on the lines, it seems that they occur in the concentric zoning, a small distance outside the border between the irregular centre and the concentrically zoned part of the crystals. In A2a it seems to coincide with a wavy growth band, while in A1b the location is less clear but seems to coincide with a wide zoning band. However, both crystals display elevated Cr concentrations in the concentric zoning, starting at the border and gradually decreasing outwards towards the rim, compared to the irregular centre (the A1b core is an exception of this, as discussed in section 4.4.2).

All lines in A1b display Cr increases of varying degree. The three large spikes in A1b-2, A1b-3 and A1b-4 increase with 1250 ppm, 1800 ppm and 3000 ppm respectively, i.e. the spikes have concentrations of 6, 10 and 11 times the base level concentration. In contrast, the lines A1b-1 and A1b-5 exhibit only small increases during a gradual decrease rather than a sharp spike (fig 23). In fact, A1b-1 exhibits two of these increases. The increases are approx. 450 ppm and 350 ppm, corresponding to 5.5 and 2.4 times the base level concentrations.

A2a display Cr spikes in all lines but one (A2a-4), however this line still exhibits slightly elevated Cr

concentrations and the gradual decrease towards the rim that is recorded in the other lines. Additionally, line A2a-3 exhibits a spike at one part of the crystal but lacks a spike in the unzoned overprinted part of the crystal. However, here it displays a gradual decrease similar to the other lines. The four lines with Cr spikes display spikes with a similar trend, even though they have slightly different concentrations. They all increase 450-980 ppm, resulting in concentrations 10, 12, 15, and even 50 times the estimated base level concentrations.

Finally, some of the lines in both A1b and A2a (A1b-4 and A2a-1 - 4) show small Cr increases at the rim, however these increases are not similar to the spikes seen in the sector zoned crystals.

4.4.5.3 Cr spikes and liquid composition

Using the partition coefficient of Cr according to appendix B table 1, liquid compositions were calculated for chosen Cr spikes and plotted in figure 23-24. As is evident from these graphs, the relative concentration of Cr is higher in the clinopyroxene crystal than it would be in the surrounding liquid, as is suggested by the high partition coefficient of Cr in clinopyroxene. Furthermore, the calculated Cr concentration in the liquid not the same in all crystals. The spike in A1a-3 is calculated to represent a liquid Cr concentration of 250 ppm, the spike in A1b-3 a liquid Cr concentration of 400 ppm, the spike in A1b-4 a Cr concentration of 700 ppm in the liquid, and the spike in A2a-2 a Cr concentration of 100-150 ppm.

4.4.5.4 Cr spikes and other elements

In a few instances Ni experiences an increase during the Cr spike. This is recorded in A1a-2, A1b-4 and all A2a spikes. Furthermore, Cr spikes simultaneous with an increase of Sc and a slight decrease of LREEs was observed. Finally, as mentioned in section 4.4.5.1 one

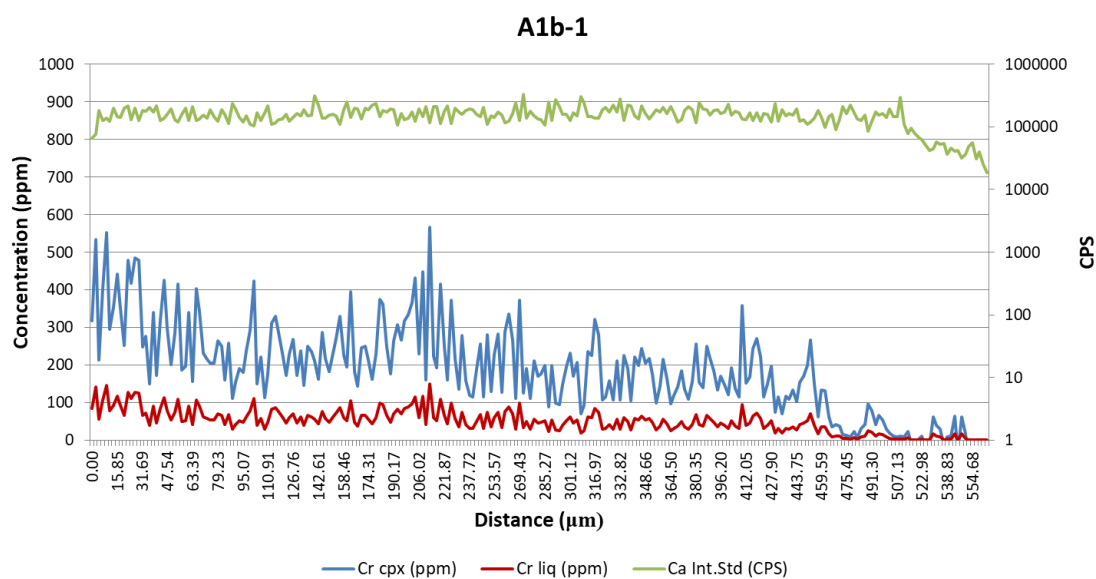


Fig 23: The gradual Cr decrease recorded in line A1b.1. The red line (lower) represents the calculated liquid composition using $D(\text{Cr}) = 3.8$. The blue line (middle) represents the Cr concentration in the clinopyroxene crystal, and lastly the green line (top) is Ca (internal standard) plotted in CPS at the right axis. A value of Ca of <100 000 CPS is interpreted to suggest that the analysed phase at that point is not a clinopyroxene crystal, where the Ca-line goes below 100 000 CPS can be regarded as the edge of the crystal.

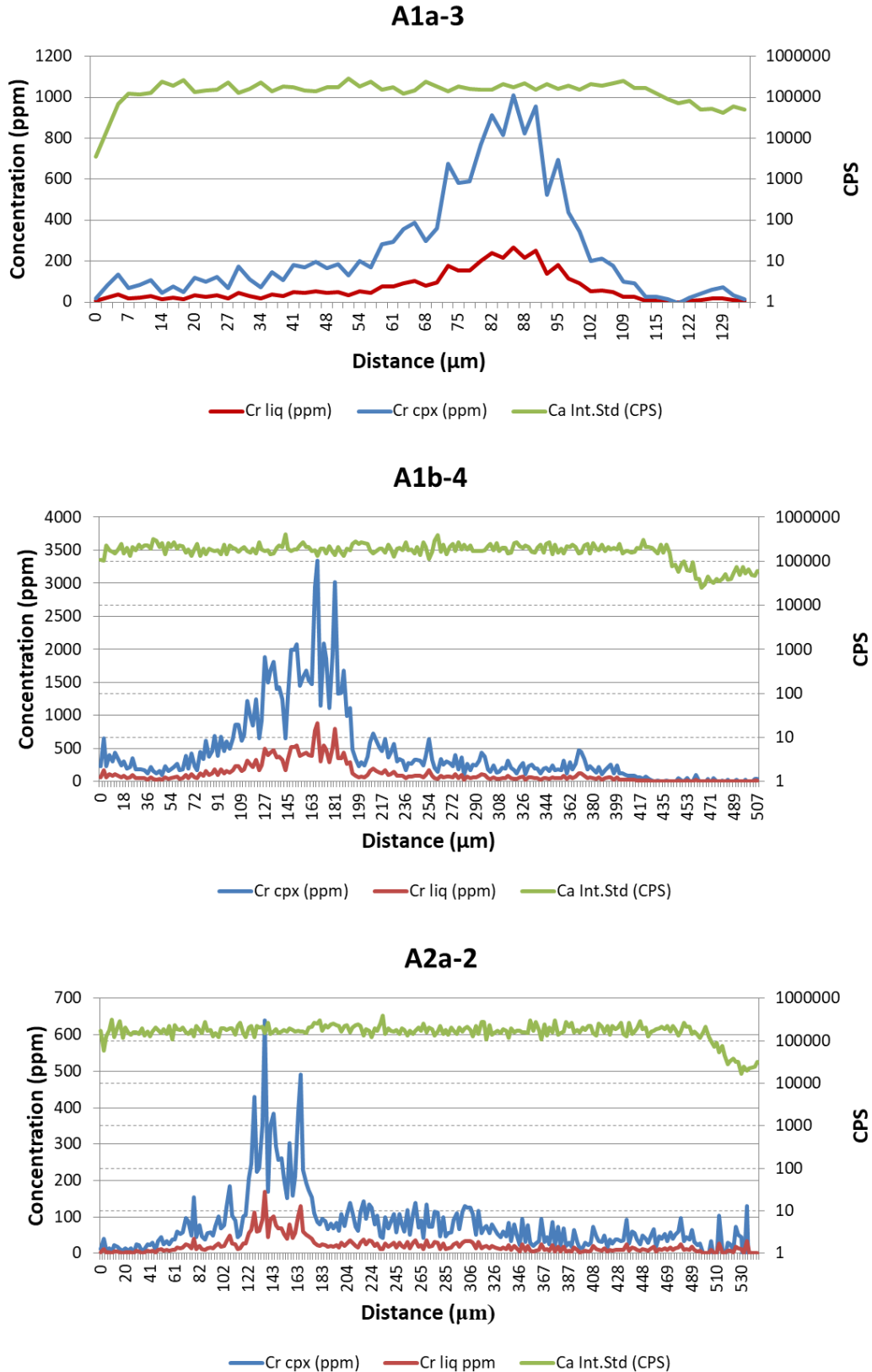


Fig 24: A selection of the Cr spikes recorded in line A1a-3, A1b-4 and A2a-2. The red line (lower) represents the calculated liquid composition using $D(\text{Cr}) = 3.8$. The blue line (middle) represents the Cr concentration in the clinopyroxene crystal, and lastly the green line (top) is Ca (internal standard) plotted in CPS (counts per second) at the right axis. A value of Ca of $<100\,000$ CPS is interpreted to suggest that the analysed phase at that point is not a clinopyroxene crystal, thus where the Ca-line goes below $100\,000$ CPS can be regarded as the edge of the crystal. With this in mind, note the location of the spike in relation to the rim in A1a-3 compared to A1b-4 and A2a-2.

of the spikes in Al₁-1 is accompanied by a Co spike. However, the behaviour of other elements during Cr spikes is irregular and therefore difficult to evaluate.

5 Discussion

Before discussing the results it must be noted that there are uncertainties in the results presented in this thesis. The interpretations have been made with respect to these uncertainties; nonetheless, they need to be highlighted. First of all, only one sample was used and only four clinopyroxene crystals were analysed. Additionally, as the thesis focused on clinopyroxene the matrix was scarcely analysed. Therefore, despite the likely scenario that the features seen in these crystals are to be seen in other crystals evolved in the same magma body as well, it should be noted that the result in this thesis is based on analyses of only a fraction of the magma body. Secondly, while the SEM results are based on numerous data points there is always a possibility that the results do not represent the whole truth. An example of this is the width of the rims which were estimated from only a few sites on each crystal, and should not be regarded as absolute and representative values. Furthermore, time restrictions left some aspects inadequately analysed simply due to unintentional oversight. Also, while SEM analyses offer the possibility of high resolution analyses, point analyses can be slightly imprecise when analysing undefined features, as was the case when analysing the light band in the rims. It is also important to remember that when comparing concentrations of elements with low concentrations, i.e. Ti and Fe, between different sites, small changes in absolute concentrations can yield large relative changes. Thus, chemical variations representing a large relative change might simply be within the error margin of the analysis.

Thirdly, the LA-ICP-MS analyses were performed on a limited number of lines and spots. While the data acquired can be considered representative, caution has to be taken when applying them to the bigger picture. Furthermore, it cannot be ruled out that due to the spot size, minor variations in the clinopyroxene crystals were not recorded. Finally, the increase of Cr concentration in the Cr spikes was estimated relative to the Cr base level concentration before and after the spike. These estimations are dubious since the base level concentration varied throughout the analysed lines and was assessed graphically using an approximate mean concentration. Therefore, these estimations should only be used to acquire a general apprehension for the size of the Cr spike and not as absolute values.

Finally, a comment has to be made on the validity of the hypotheses presented below. The results in this thesis, while supporting the hypotheses presented, are not completely unequivocal and more studies are needed to be able to constrain the history of these clinopyroxene crystals with certainty. Therefore, all hypotheses presented should be regarded with caution.

5.1 General chemistry and substitution relationships

This section will discuss the general chemistry and the substitution relationships of the sample. A negative

correlation was observed between Mg and Fe, and adding the calculated Mg ions and Fe ions yields sums of around 1, both observations indicating that Fe-Mg substitution occurs in the sample. Considering that the crystals were determined to be of magnesian end-member composition, i.e. diopsides, it is therefore likely that Fe substitutes for Mg in a number of the octahedral sites. Similarly, a negative linear relationship was observed between Ti and Mg, likely an indirect substitution due to the evolution of Ti in coupled substitution (see section 5.2). A negative linear relationship was also seen between Al and Si, likely indicative of Al substitution in the tetrahedral sites of Si. Al can also substitute in the octahedral sites which can be regarded insignificant considering the sum of Fe and Mg of around 1; however, as will be discussed below, the zoning of Fe is irregular, and the element is only zoned in some instances. This suggests that while Fe-Mg substitution may occur when Fe is zoned, the instances where Fe is not zoned - despite zonation in Mg - might be instances where Al-Mg substitution occurs instead, i.e. Al is incorporated into the octahedral sites. Furthermore, Na likely substitutes for Ca in the 8-coordinated sites, however this substitution have not been related to the zoning and it seems constant throughout the crystals. Finally, the Al/Ti ratio is similar in different sites despite varying Al and Ti concentrations. This indicates that while the concentrations may change, no extensive internal fractionation between Al and Ti occurs in the sample.

The differences in concentration observed in the REEs can be attributed to two factors. The results showed lower concentrations of REEs with odd atomic numbers than REEs with even atomic numbers. This was an expected outcome as it is in line with Oddo-Harkins rule. However, it was also observed that the LREEs have higher concentrations than the HREEs. This possibly points to REE fractionation, in which the less incompatible HREEs are fractionated away while the more incompatible LREEs are enriched, suggesting the magma body in question has had time to experience fractionation and become more evolved (for continued discussion, see section 5.8). Finally, the very low concentrations of highly incompatible elements Nb and Ba and higher concentration of some compatible transition metals indicates that the system was relatively unevolved at the time of the crystallization and eruption. This is consistent with the ultramafic and silica undersaturated nature of the samples, inferred by e.g. the lack of quartz and the presence of nepheline, as well as the occupancy of Al in the tetrahedral sites (see section 2.3.1).

5.2 The chemical and crystallographic nature of the sector zoning

When analysing the sector zoned crystals A1a and A2b it is clear that the sectors are characterized by markedly different chemistries. In both optical microscopy and BSE imaging the sectors were distinguished simply by observing the difference in contrast which was opposite between planar light in optical microscopy and BSE, i.e. the light sectors in optical microscopy appeared dark in BSE. These dark sectors, rich in Mg and Si, are interpreted to represent the hourglass sec-

tors, also called basal sectors, while the light sectors are thought to represent the prism sectors. The Mg+Si sectors display higher Mg# than the Al+Ti sectors, meaning that the Mg/(Mg+Fe) ratio generally is higher in the Mg+Si sectors. Furthermore, Si and Mg seem to correlate with each other, as the Mg+Si sectors also have higher Si concentrations than the Al+Ti sectors. The Mg+Si sectors also have lower Al and Ti concentrations, probably responsible for the darker contrast in BSE imaging. However, despite the fact that the Mg+Si sectors have lower Al and Ti concentrations overall, the Al/Ti ratios are the same as in the Al+Ti sectors. As mentioned in section 5.1, this indicates that even though the Al and Ti concentrations are different between the sectors, there is no significant fractionation between Al and Ti. Rather, the compositional difference between the Al+Ti sectors and the Mg+Si sectors is governed by the coupled substitution $[Mg + Si] \rightarrow [Al + Ti]$, as presented by Ubide et al. (2019), further indicated by the distinctly different chemical compositions when plotting elements from the different sides of the substitution reaction (see appendix B fig 2). The substitution is likely coupled due to Al incorporation in the tetrahedral and octahedral sites, as mentioned in section 2.3.1. Note however that the involvement of Fe in this substitution by Ubide et al. (2019) is omitted here since Fe was analysed as $Fe^{2+} + Fe^{3+}$, and therefore it is not possible to distinguish ferrous and ferrous iron in the substitution.

As suggested by the trace element analyses, incompatible elements are enriched in the Al+Ti sectors relative to the Mg+Si sectors. However, V and Sc also show an increase in the Al+Ti sectors despite the fact that they in most studies presented in table 1 were reported to have a partition coefficient of >1 , and therefore should be regarded as compatible. This is difficult to explain with the results in this thesis alone, however one explanation may be simply the varying nature of the partition coefficients as a response to surrounding factors. Since some studies concluded partition coefficients of <1 for both V and Sc, it can be suggested that the variation of the partition coefficients cause them to fluctuate around 1. This is in contrast to Cr, Ni and Co, all of which are not sector zoned and are more reliably proved to be compatible. Thus, Sc and V might in this specific context have partition coefficients of <1 and behave incompatible.

Due to the presence of subsectors in A1a, the Al+Ti sector is in this crystal interpreted to be made up of three prism sectors in each twin, which when mirrored results in the appearance of five subsectors. As mentioned in the results, these subsectors are chemically very similar; however, BSE imaging reveals differences in contrast. Using the information acquired about the Al+Ti and Mg+Si sectors, a lighter contrast is interpreted to indicate slightly higher Al and Ti concentration, as well as slightly lower Mg and Si concentration. With this reasoning in mind, it is probable that subsector (1) has slightly higher concentrations of Al and Ti than subsector (2) and (3), and that (3) has the lowest Al and Ti concentrations. Using the information given in Ubide et al. (2019), these subsectors can be identified as prism sectors $\{100\}$, $\{110\}$ and $\{010\}$ respectively. This is an interpretation that goes well in hand with previous research in which it

was suggested that the concentrations of Al, Ti and Fe in the prism sectors are $\{100\} > \{110\} > \{010\} > \{-111\}$, the latter being the hourglass sector (Hollister & Gancarz, 1971).

It is worthy of note that neither A1a nor A2b exhibit the clear hourglass zoning commonly associated with sector zoning. However, hourglass zoned clinopyroxene crystals occur in the thin sections as well, and the appearance of the sector zoning is interpreted to simply be a product of how the crystal was cut when the thin section was made (see fig 4). An hourglass type zoning requires that the crystal is cut along the c-axis completely viewing the hourglass sectors. Hence, any crystal cut at an angle towards the c-axis will not display complete hourglass zoning. This is likely the case with A1a whose Mg+Si sector likely represents the hourglass sector viewed obliquely (fig 25), consistent with the chemistries of the sectors presented in literature (e.g. Ubide et al., 2019). It is further supported by the EBSD results, confirming that the crystal is oriented at an angle towards the c-axis. In contrast, A2b exhibit zoning that is closer to the typical hourglass zoning despite not exhibiting a perfect display of the hourglass sectors. The fact that the hourglass sectors fail to meet in the centre indicates that while the crystal likely was cut along the c-axis, it was not cut right in the middle but rather slightly closer to one of the crystal's edges. However, the fact that a twinning plane runs through the crystal might change the perception of the sectors, and it might explain why a cut along the c-axis is not coherent with the apparent shape of the crystal when comparing with fig 4. Also important to note is the irregularity of the A2b sectors and twinning plane which are markedly different from the pristine sector and twinning plane seen in A1a, leading to the argument that A2b grew under slightly different circumstances than A1a. What caused these irregularities cannot be explained with the results in this thesis; however, it might be related to crystal kinetics during growth. For example, slightly lower growth rates would enable the influence of diffusion which would otherwise have been outgrown. The same reasoning can be applied to the irregular zoning. It can be concluded that while A2b grew similarly to A1b, it was affected by slightly different factors – for example growth rate – resulting in an imperfect sector zoning. Furthermore, if the irregular zoning is assumed to be classified as patchy zoning it can be used as an additional indicator of open system processes (see section 2.3.6) or disequilibrium crystallization. Open system processes further comes into play when considering that sector angles may be affected by mixing with a hot magma, as discussed in section 2.3.6. Thus, open system processes may also be responsible for the irregular nature of the sector zoning. However, this hypothesis leaves the question why A2b displays irregular sector zoning while A1a does not. Aside from these speculations, assuming that A2b grew under different circumstances than A1a would indicate that it might have grown at another stage in the crystallization or in a slightly different part of the system.

Finally, the optically different interval in both crystals approaching the rim might be attributed to magma chamber processes. In A2b, this interval is characterized by concentric zoning. This could either

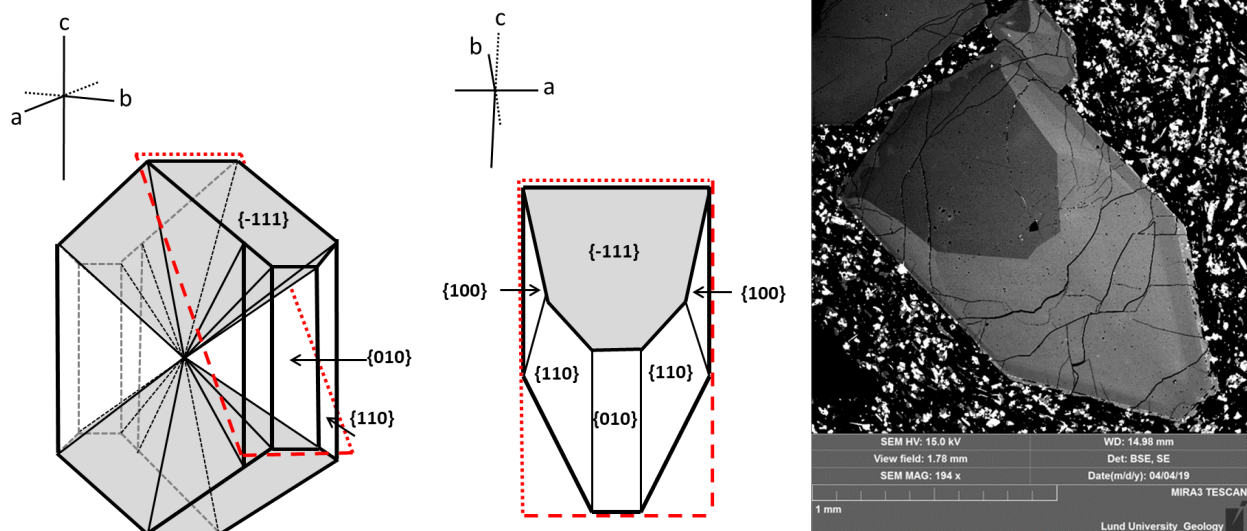


Fig 25: A suggestion for how A1a was cut in the thin section in relation to the sector zoning, redrawn from Ubide et al. (2019). The proposed cutting surface is marked by red lines. Note the distinction between the dotted red lines and the dashed red lines, illustrating that the crystal is likely viewed from the crystal centre as suggested by the EBSD results. The right axis indicator (indicating the orientation of the axes in relation to the surface) is approximate and is drawn to illustrate that the c-axis is tilted away from the viewer (illustrated by the dotted line), and that the b-axis is oriented towards the viewer and inclined slightly upwards, 90° from the c-axis and the a-axis. Note also that the twinning plane observed in the thin section is excluded from this figure for simplicity, and that the crystal in reality would consist of two twins rather than a single crystal. Finally, the proposed cutting surface can be related to the BSE picture to the right as it displays the sectors in question.

indicate the onset of convection in the magma chamber, or simply kinetic processes related to a lower growth rate. However, since the sector zoning in the interval seems to be unaffected a lower growth rate is not the most likely explanation. As the corresponding interval in A1a displays a darker contrast in BSE, it is interpreted to have slightly lower Al and Ti and slightly higher Mg and Si concentrations than the Al+Ti sector. Following the discussion in section 2.3.1, the incorporation of Al in the tetrahedral sites might be positively correlated with temperature, meaning a higher temperature would result in lower Si concentration (Kushiro, 1960). Thus, a lower Al concentration and higher Si concentration would indicate a decrease in temperature. If assuming this is correct, it would be consistent with a lower growth rate possibly inferred by the concentric zoning in A2b. On the other hand, as will be discussed in section 5.5, the intervals might be related to the spikes of Cr recorded in the crystals. Indeed, the Cr concentrations seem to be slightly elevated in the concentric zoning of A2b, and the location of the spikes in the rims of A1a could be argued to be consistent with the interval of lower Al and Ti.

Note however, that the suggestions above are merely speculations and more analyses on the chemistry in these intervals are required to evaluate the cause with certainty.

5.2.1 Differences in partition coefficients between sectors

As mentioned in section 3.2.2, the calculations of the relative partition coefficients were made based on the assumptions that the liquid composition did not change over time, and that the sector zoning was solely kinetically controlled. These assumptions naturally result in

an extensive simplification of the system and the results should therefore not be interpreted too heavily. Rather, they are to be considered approximate relative partition coefficients illustrating the kinetic control of the sector zoning, and the liquid composition used in the calculation likely does not represent the true liquid composition, as this would more likely be an intermediate between the two sectors' corresponding liquid compositions. It can, however, be argued that the hourglass sectors $\{-111\}$ generally have lower partition coefficients for most trace elements than the prism sectors.

5.3 Character of the concentric zoning and clues to the growth history

As mentioned in the results, Al is the element that shows the most pronounced zoning. Similar to the sector zoning, the bands that appear light in BSE are the bands with a higher concentration of Al. Similarly, the overprinted part of A2a has a slightly higher concentration of Al than surrounding pyroxene. Al is accompanied by Ti, which might explain the lighter contrast in BSE imaging, and opposed by Mg and Si. This leads to the conclusion that the oscillatory zoning is governed by the same coupled substitution as the sector zoning, i.e. $[\text{Mg} + \text{Si}] \rightarrow [\text{Al} + \text{Ti}]$. Furthermore, Fe is observed to behave irregularly, and is not always distinctly zoned. In a few instances, however, it displays a similar pattern as Al and Ti. As discussed above, a possible reason for this is Mg-Fe substitution. As the Al concentration is increasing, and coupled substitution invokes a decrease of Mg, Fe might become involved in the substitution and substitute for Mg. In other words, Fe behaves oppositely to Mg, rather than conformably with Al. Furthermore, the in-

stances where Fe does not appear to be zoned might be characterized by Al-Mg substitution, meaning that Al enters not only the tetrahedral Si-site but the octahedral Mg-site as well.

Similar to the sector zoned crystals, the varying chemical compositions can to some extent be divided into groups. This leads to the observation that A2a has one composition very similar to the Al+Ti sectors of the sector zoning, and one composition intermediate of those and the Mg+Si sectors. A1b, however, has a more varying chemistry that constitutes a range between the Al+Ti and the Mg+Si sectors. The chemically diverse nature of the concentric zoning compared to the sector zoning can be explained simply with the fact that it is a different type of zoning, and while sector zoning is characterized by defined areas of two distinct compositions, concentric zoning exhibits less sharp boundaries. Rather, the composition fluctuates between ends of a spectrum, producing an unlimited number of compositions in between. Furthermore, the resolution of the concentric zoning can be low and therefore it might prove difficult to isolate certain compositions, which in combination with the challenge of identifying the different bands in SEM can lead to unintentional bias that might affect the results. Therefore, it is not unlikely that A2a in reality has the same extensive chemical variation as A1b, only that A2a was analysed with unintentional bias.

The width of the concentric zoning is very varied as well. This can likely to some extent be attributed to how the crystal was cut. In A1b, for example, it is evident that the bands on one side are wider than the bands on the other side of the centre, and similarly that part of the crystal also has a larger core-to-rim width. It is therefore possible that this crystal was cut oblique to the c-axis, and that the crystal would be closer to symmetric if viewed differently, for example along the c-axis. It is also important to consider different growth rates in different sectors of the crystal, and the possibility that it is the differing growth rates that yield one part with wider and one with narrower bands, both kinds of sectors represented in the A1b crystal. This would pose a more likely explanation for the askew location of the irregular centre. Therefore, taking conclusions from the absolute widths of the zoning bands is not suitable to this situation as the true width can only be roughly estimated using the known widths as limiting values. Nonetheless, it is still possible to evaluate the relative widths of bands that are positioned close to each other. Furthermore, A2a is more symmetric and likely cut with a lesser angle towards the c-axis, possibly the reason why the band widths in this crystal display less variation than those of A1b. Hence, the band widths of A2a can be used to get an apprehension for the true band widths of A1b.

With this in mind, it is evident that the widths of the zoning bands are varied and alternates between thicker and thinner bands. Since the method of characterizing the bands as oscillatory bands and growth bands according to the distinction presented in Streck (2008) is dubious due to the cutting issues mentioned above, discrimination and evaluation of zoning origin can only be done speculative. However, if assuming that the character and width of the A2a zoning bands are close to the truth, it can be established – using the

definition in Streck (2008) – that the concentric zoning consists of both growth bands and oscillatory zoning, since the crystals exhibit both narrow bands of $<10\ \mu\text{m}$ as well as wider growth bands.

Since width of zoning cannot be used as a certain indicator for zoning origin, chemistry might give a better understanding. As mentioned above and discussed in section 2.3.1, the incorporation of Al into the tetrahedral sites might be temperature dependent, with higher temperatures leading to more Al in the tetrahedral site and, as follows, a lower concentration of Si. Considering that the zoning is characterized by intervals of higher Al and Ti and lower Mg and Si, this may indicate that the zoning was at least partly caused by a fluctuating temperature resulting from convection in the magma chamber; thus, the zoning would be considered a primary growth feature and not a result of kinetic processes. However, it is likely that kinetic processes affected the zoning as well. Because of this, the zoning will continue to be referred to as “concentric” zoning to highlight the possibility of several different affecting factors.

5.3.1 Origin of the A1b core

The irregularly shaped core in A1b is interpreted to be a partially resorbed early clinopyroxene phase. This interpretation is partly based on optical observations, and partly on chemical analyses. As for the optical observations, the comparison between A1b and A2a is important. While A1b possesses the irregular core, A2a does not; however, the two crystals have in common that the centre is irregular and not concentrically zoned. Furthermore, both of them are hosts to small inclusions that in A1a are concentrated along one of the resorbed surfaces of the core. This leads to the conclusion that these small inclusions formed upon resorption of the core. The fact that A2a, while lacking a core, possesses small inclusions throughout the entire centre of the crystal therefore indicates that these formed upon resorption of an A2a core, only that this core became completely resorbed while the A1b core only became partially resorbed. As follows, this would suggest that the entire irregular centres of the crystals are replacement material formed when the core was resorbed and replaced. Since the irregular centre of A2a is slightly smaller than that of A1b, it is possible that the resorption of the A2a core went to completion simply because the core was smaller from the beginning. This is however a subject of speculation since cutting effects can be behind the difference in centre width just as it likely affected the width of the concentric bands; and furthermore, considering that the three dimensional crystals are observed in a two dimensional medium, it cannot be ruled out that A2a was cut adjacent to the centre and in reality possesses a small core that simply was cut away from the sample.

As for the chemistry, the chemical analyses revealed that the core of A1b has the most primitive composition observed in terms of high Mg# and low Ti concentration, and further the trace element analyses showed that the core is rich in Cr and Ni which are two highly compatible elements that would fractionate away early in the evolution of the system. Additionally, the core has lower concentrations of incompatible elements, for example REEs, which are ex-

pected to increase in concentration as the system evolves. This infers that the core is the most primitive - and therefore likely earliest - phase present in the analysed clinopyroxene crystals. This is further supported by the fact that this early phase has been either partially or completely resorbed, and that by that point this early phase was no longer in equilibrium with its surroundings, suggesting that the system over time evolved away from this early phase towards the concentrations observed in the other parts of the crystals. However, it is important to note that it is not a given that the core represents an earlier phase of this magmatic system. It is also possible that it is a xenocryst that is not genetically related to the magma from which the concentrically zoned mantle was formed. A xenocrystic clinopyroxene entering a new magmatic system would likely be in disequilibrium with the surrounding magma and therefore become resorbed, similar to how an early primitive phase would. Whether the core was simply an early phase genetically related to the system or a xenocryst is not possible to determine from these results; however, taking into account the differences in chemical composition between the core and the mantle - and the amount of fractionation and time of system evolution that difference entails - the xenocryst hypothesis would seem to be a likely explanation.

5.4 Chemical imprints from eruption and mass wasting events

The rims have chemistries not seen in any other part of the crystals, most noteworthy a light band (in BSE) inside of the rim and a sharp Al decrease. The rims also have lower Mg# values than the sector zoning and concentric zoning, suggesting that unlike the zoning these chemical changes are not strictly governed by the $[Mg + Si] \rightarrow [Al + Ti]$ substitution, even though it cannot be ruled out that this substitution occurs to some extent to achieve charge balance. For example, the light contrast of the light band in BSE likely comes from a higher concentration of Ti and/or Fe, and whether it is Ti or Fe that exhibits the largest peak at the light band seem to be related to the behaviour of Al, as Fe only has the largest spike at sites where the Al drop occurs at the light band, rather than after. The behaviour of Al also seems to be related to the Mg and Si changes, since whether these elements increase or decrease at the light band seems to be related to where the Al decrease occurs. As inferred by the results it is likely that these variations are related to in what composition the rim lies, i.e. in which sector, since the Mg+Si sectors seem to experience the sharp Al decrease at the light band, whereas in Al+Ti sectors Al stay the same or exhibit a slight increase at the light band, only to sharply decrease outside of the band. As follows, it can be deduced that Fe only has a larger peak concentration than Ti at the light band in the Mg+Si sectors, and also that these same bands does not experience a decrease in Mg and Si. This is likely due to the fact that the sector in general has lower concentrations of Al and Ti and higher concentrations of Mg and Si, and thus disfavours Al and Ti - allowing Fe to take the place of Ti at the light band - and favours Mg and Si. It goes to show that the chemical composition of the pyroxene influences the way the

elements behave in response to environmental changes. However, there are variations to these results, for example in the behaviour of Mg and Si at the light band, and as follows they are not unequivocal and should not be interpreted too heavily. Furthermore, the light bands occur at small scales and are therefore problematic to analyse with high accuracy, and without including data from the surrounding.

The discussion above refers to the light band that occurs just before the Al poor rim. Some sites, chiefly in the concentrically zoned crystals, were observed to exhibit two light bands or even what is referred to as a “double rim”, and hence it is the outermost band of these two that are analysed and discussed above. The presence of two light bands will be discussed further below, however a few comments have to be made regarding these. It is important to note that while the “double rims” are distinguishable, the distinction between two light bands and one light band is not always apparent. In some instances, the two light bands are clearly separated, while in others they are close together and therefore very similar to the single bands seen in the sector zoned crystals. Therefore, the observations regarding the nature of the light bands should be used with caution, and continued research is needed to confirm the frequency of two light bands and “double rims” in the concentrically zoned crystals compared to the sector zoned crystals.

The chemical changes in the rims are interpreted to be connected to the eruption event and the result of decompression and ascent, however this interpretation is not unequivocal if taking into account the results of Ubide & Kamber (2018) (see section 2.3.6). They observed outermost rims that had higher concentrations of Al and Ti and lower concentrations of Mg and Si, and suggested that these rims represent final decompression and surface crystallization. If assuming that Al increases in response to decompression, it would mean that the sharp Al decrease observed in the clinopyroxene crystals in this thesis would be the result of the opposite, i.e. higher pressure. This is not feasible, and likely the concentration of Al is governed by other processes going on during decompression and ascent. However, if assuming that the Al concentration increases upon decompression - in line with the interpretations by Ubide & Kamber (2018) - it can be related to the light band inside of the rim. The Al increase recorded at the light band in some sites, as well as the Al increase observed in the concentrically zoned crystals, would then be interpreted as results of lower pressure, and the light bands as recorded moments of pressure decreases. Finally, this suggests that a pressure decrease occurred just before the rim was formed, i.e. just before or at the start of decompression and ascent. Furthermore, the observations of two light bands and “double rims”, and the fact that these two light bands were mainly—and “double rims” were exclusively—observed in the concentrically zoned crystals thus suggest that these crystals might have recorded two events of pressure decrease, with only one occurring just before the actual eruption. Important to note is that an Al increase at the light band is not a constant occurrence; however, the “double rims” in Al₁b seem to be characterized by an Al increase and is therefore more suited for this hypothesis than the sites with two light bands.

If assuming that the above is true, and that Al is negatively correlated with pressure, the Al drop outside of the light band must be explained by other processes. If the rim represents decompression and ascent it likely crystallized in a multiply saturated system. This is consistent with the observation that the rim is host to numerous small inclusions and that these inclusions start to appear at the light band, i.e. at the supposed pressure decrease. Since these inclusions mainly consist of plagioclase crystals and iron oxides, it is reasonable to believe that the plagioclase crystals - being Al-bearing phases - along with plagioclase crystallizing in the matrix depleted the system of Al, resulting in a sharp Al decrease in the clinopyroxene rims. This is further supported by the trace element analyses, as Eu increases less at the rim than similar elements, suggesting a Eu depletion caused by the crystallization of plagioclase. Plagioclase fractionation is however not obvious when plotting the ratios Eu/Sm and Sr/Nd, which will be further discussed in section 5.8.

Simultaneous crystallization of the clinopyroxene rims and the matrix upon saturation of multiple phases might also explain the increasing concentrations of incompatible trace elements in the rims. Since incompatible elements during crystallization preferably stays in the liquid phase, while compatible elements enter the solid phase, the incompatible elements slowly become enriched in the system. During multiple saturation, many phases, and therefore a large part of the bulk volume, crystallizes simultaneously and the enrichment of incompatible elements is likely quicker than it is earlier on the liquid line of descent, resulting in the relatively steep increase of incompatible elements over a short distance in the clinopyroxene rims. It also explains why highly incompatible elements like Nb increase more than other less incompatible elements, and why the concentration of compatible elements tend to not increase in the rim. Finally, the irregularity of V might be caused by a fluctuating partition coefficient that according to previous research (see section 2.3.3) lies around 1, or by the presence or lack of V-enriched phases in the rim or matrix affecting the results.

5.5 Link between Cr spikes, magma recharge and the eruption event

The sudden spikes of Cr create an interesting dimension to the evolution of the clinopyroxene crystals. Similar to previous research (see section 2.3.6), the spikes are interpreted to be caused by injections of primitive magma into the magma chamber, i.e. magma recharge. The reasoning behind this is that Cr is a compatible element that is fractionated away early in the evolution of a system, as argued in section 5.3.1 when discussing the A1b core. Furthermore, Cr is also highly compatible in clinopyroxene which suggests that the presence of Cr in the system would result in a proportional presence of Cr in the clinopyroxene. Therefore, very low base level concentrations of Cr interrupted by spikes with high concentrations indicate that new Cr has been added to the system. The simplest explanation for this Cr addition is the injection of new primitive magma into the system, as this magma has yet to be fractionated and depleted of compatible

elements. The calculated liquid composition of Cr in the system presented in section 4.4.5.3 give insight into the bulk concentration of Cr at the time of the magma recharge; however, these calculations do not consider varying partition coefficients, which might explain the difference of the calculated Cr concentration in the melt between spikes in the concentrically zoned crystals, despite them likely recording the same event. The melt concentrations can thus only serve to illustrate the addition of Cr to the system.

Because of the high partition coefficient for Cr in clinopyroxene, the crystals would in theory be one of the primary candidates for uptake of this newly added Cr, resulting in a spike. The fact that a few of the Cr spikes are accompanied by an increase in Ni, which also is a compatible element that fractionates away from the system early in the evolution, further supports this interpretation.

The large Cr spikes in the concentrically zoned crystals A1b and A2a are located in the interior of the crystal, more specifically outside the border between the irregular centre, i.e. the replacement of the resorbed core, and the concentric zoning, with elevated concentrations already at the start of the concentric zoning compared with the irregular centre. The lines lacking spikes are partly explained by the position of the line, with A2a-4 probably starting outside of the spike. Furthermore, the lack of spike in one section of A2a can be explained either by post-recharge overprinting or by crystallographic differences in Cr uptake.

The common location and the similarities of the spikes in the concentrically zoned crystals in terms of size - with concentrations of 10-15 times the base level concentration, with two outliers of 6 and 50 times the base level concentration - indicate that the spikes were caused by the same event of magma recharge. Furthermore, the two crystals have in common that the Cr concentration after the spike gradually decreases throughout the concentric zoning. There are two possible explanations for this. Either, the magma recharge causing the spike was sufficiently large that it took a certain amount of time before it disappeared from the system. This is consistent with the fact that the concentration in the crystals becomes lower further out from the spike, similar to how the bulk concentration of the system would become lower over time as the Cr is incorporated into solid phases. Or, the magma recharge was initiated with a relatively large injection causing the spike, after which there was a continuous inflow or pulses of primitive magma into the magma chamber, diminishing over time. In both cases, the spike would have had to be preceded by a slightly smaller influx causing the elevated concentrations inside of the spike. Which one of these hypotheses that is correct cannot be determined from the results in this thesis. However, what is certain is that elevated concentrations of Cr were present in the magma chamber throughout the crystallization of the concentric zoning, and that these concentrations were not present during the crystallization of the irregular centre. The fact that the elevated Cr concentrations seem to coincide with the concentric zoning begs the question if and how the two are related. If the zoning is to be classified as a primary growth feature caused by temperature changes

following convection in the magma chamber, this convection is likely what is causing the oscillatory behaviour of Cr during the gradual decrease. As discussed in section 2.3.3 the partition coefficient for Cr might be dependent partly on the amount of Al in the tetrahedral sites; furthermore, Al and Cr seemed, according to the results of Skulski et al. (1994), to be enriched in the same sectors, suggesting a positive correlation between Cr and the amount of Al allocated in the tetrahedral sites. As follows, high temperature intervals of the zoning – where the amount of Al in the tetrahedral sites is higher and the concentration of Si therefore is lower – would feature a higher concentration of Cr. The positive correlation between Cr and temperature can further be supported by the fact that the large Cr spike in A2a occurs in a slightly irregular and wavy band, possibly indicating dissolution caused by the high temperature of the magma recharge (see section 2.3.6). Thus, while the large spikes are interpreted to represent the actual magma recharge event, the smaller increases along the gradual decrease, which are clearly observable in A1b-1, are interpreted to represent merely an interval of higher temperatures due to convection or – if assuming that the large injection was followed by numerous smaller injections, as described above – smaller secondary injections.

In contrast to the concentrically zoned crystals, the Cr spikes in the sector zoned crystals occur in close proximity to the rims. This is especially evident in A1a which was observed to have Cr spikes in all analysed rims (fig 26), while A2b only have Cr spikes in two of the lines. The other two lines inferred that a Cr spike occurs in the matrix close to the crystal. This is a peculiar observation since it lacks coherence with the other results. In theory, while plagioclase is unlikely to experience a large uptake of Cr, iron oxides might be responsible for the uptake. If the iron oxides incorporated a high amount of Cr it would be responsible for the Cr spike seen in the matrix. This reasoning can be applied on A1a as well, since an additional spike was observed in the matrix outside of the rim that coincided with a spike in Co (line A1b-1). Since Co does not correlate with Cr in other spikes, this could indicate Cr uptake by another phase. However, it does not explain why no Cr spike was observed in the rim of A2b despite it being observed in two other rims of the crystal. There are however possible explanations. The Cr spikes that were observed in A2b are smaller and less pronounced than those in A1a, which goes along with the fact that A2b generally contain lower concentrations of Cr. This indicates a difference in partition coefficient leading to a lesser uptake of Cr for A2b, supported by the fact that the relative increases of the spikes are proportional to the base level concentrations and similar to the spikes in A1a. Furthermore, the Cr spikes observed in A2b seem to be located in the Al+Ti sector—as is the case with A1a as well since only Al+Ti sector rims were analysed—while the lines which do not display Cr spikes in the rims are located in the Mg+Si sectors. This observation is however not definite, since one of the lines in the Al+Ti sector encounters the Mg+Si sector type compositions produced by the irregular zoning. However, if assuming that the compositional differences of the irregular zoning are governed by other processes than the sector

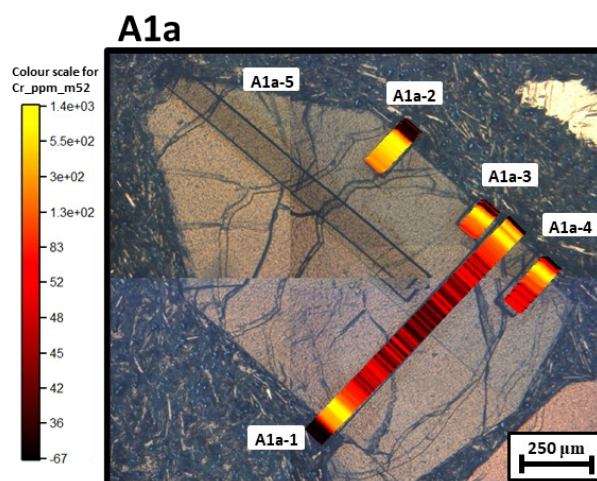


Fig 26: Cellspace image of the Cr spikes in A1a, all located in close proximity to the rim. A1a-5 was excluded when producing the cellspace images due to fault of software.

zoning, the different kinetic properties of the sectors might be the determining factor for the Cr uptake. In other words, varying partition coefficients or other kinetic processes may result in little uptake of the Cr in the Mg+Si sectors and affect the presence of Cr spikes. Important to note, also, is that even in the lines lacking Cr spike in the crystal the Cr concentration reaches slightly higher values in the concentric zoning near the rim than in the rest of the crystal, as discussed in section 5.2, indicating some extent of Cr uptake.

Of course, the incoherence regarding the presence and location of the spikes may also be attributed to faulty analyses resulting in a misplacement of the spike or signal misinterpretation.

While the results of A2b are ambiguous, the spikes in A1a are consistent in all analysed rims. The proximity of the spikes to the rim suggests that the magma recharge occurred closely before the eruptive event, begging the question if the eruption might be connected to the magma recharge as suggested in Ubide & Kamber (2018). The location of the Cr spike in relation to the chemical changes in the rim certainly points to that being true, however it cannot be argued to be true without eliminating a few uncertainties. Firstly, as with the spikes in A2b, some caution needs to be taken when evaluating the exact location of the spike. In this case, it boils down to the location of the Cr spike in relation to the light band and the Al poor rim. Since trace elements and major and minor elements were analysed using different analytical techniques, clear correlation between the results is lacking. When analysing the results of the LA-ICP-MS analyses it is possible to see where the edge of the clinopyroxene is located in the graph, however it is more problematic to find the exact location of the Al poor rim and, especially, the light band. Therefore, using the results presented, it is not possible to locate these features with absolute certainty. Speculations can however be made, from which the most likely explanations can be drawn. The spikes in A1a were estimated to be located between 25 μm and 40 μm from the edge. Considering that the rims for that crystal were measured to be 5-33 μm wide, and despite the fact that the width of

the rims varied to a large degree, the most likely case is that the Cr spike occurred shortly before the light band formed and the rim started to grow. The presence of an unusually thick rim of >40 µm, in which case the Cr spike would have occurred after the rim started to grow, of course cannot be ruled out, however it is not regarded as the most likely scenario considering the measurements taken.

Finally, if regarding the interval with lower Al and Ti concentrations discussed in section 5.2 as a result of the Cr spikes, the location of the spikes must be adjusted to fit that interval. A correlation like this is however not deemed to be likely due to (1) the immediate lack of coherence between the interval and the location of the spikes according to fig 26 and (2) the previous hypothesis that Cr is positively correlated with Al.

Due to the locations of the Cr spikes, the magma recharge event recorded in the sector zoned crystals is interpreted to be separate to the event recorded in the concentrically zoned crystals. However, what is relevant in the discussion above is the absence of Cr spikes in the rims of the concentrically zoned crystals. While a slight Cr increase is seen in some of the analysed lines, Cr spikes similar to the ones observed in the sector zoned crystals were not observed in A1b or A2a. If assuming that the rims formed during decompression and ascent, the rims of the concentrically zoned crystals would have formed simultaneous with the rims of the sector zoned crystals, thus recording the same events and processes. This incoherence can be explained similarly to the lack of spikes in some parts of A2b, i.e. by kinetic processes and varying partition coefficients. This would be consistent with the fact that small Cr increases are seen in the rim of some lines of the concentrically zoned crystals, essentially meaning that these crystals did in fact record the magma recharge event, only with a minor Cr uptake. However, if the lack of Cr spikes cannot be attributed to kinetic processes, other factors have to be considered, including growth rate and location in the magma chamber, and these will be discussed further in section 5.9.

5.6 Plagioclase compositions inferring a Na-Ca substitution trend

While plagioclase crystals in the interior of the clinopyroxene crystals are of bytownite composition, the plagioclase crystals in the rims are of labradorite composition. This suggests that plagioclase crystals that formed later in time have higher Ca concentration and lower Na concentration than the ones formed early during crystallization. This might be explained by an overall decrease in temperature and/or pressure; however, it cannot be determined from these results only. Furthermore, this progressive Na to Ca trend is not observed in the clinopyroxene crystals in which Na and Ca seemingly remains constant. Possible explanations for this are diffusion mechanisms that over time counteracts the what would be core-to-rim zoning, or that other kinetic processes limits Na-Ca substitution in the crystals. Considering that the crystals exhibit zoning, despite it not being related to Na and Ca, diffusion is not a likely explanation as it likely would counteract the zoning of other elements as well. None-

theless, it cannot be ruled out since different elements have different diffusion coefficients, and all elements would therefore not necessarily be affected the same way.

5.7 Notes on growth rates

As discussed in section 2.3.4, the presence of sector zoning can give information about the growth rates of the clinopyroxene crystals. It is reasonable to believe that the A1a and A2b crystals grew with a relatively high growth rate, outgrowing the diffusion. This is consistent with the relatively wide nature of the concentric zoning present in the outer parts of A2b, and the lack of other core-to-rim zoning.

The concentrically zoned crystals, on the other hand, might not have grown as fast. Assuming that the growth bands are primary growth features as discussed in section 5.3, a wider band should be indicative of higher growth rate since more material crystallized in that particular compositional interval. Thus, in the case for A2a, the growth bands closely outside of the irregular centre can be regarded intervals of high growth rate. In contrast, narrower bands can be interpreted to have grown under an interval of low growth rates (as long as they are still regarded as primary growth features), suggesting that the growth rate might have fluctuated. Furthermore, as discussed in sections 2.3.5 and 5.3, it is important to consider different growth rates in different sectors of the crystal, and the possibility that the differing growth rates can yield different band widths throughout the crystal. Using this reasoning, it is possible that the wider bands in A1b are located in a sector of the crystal with higher growth rate than the narrower bands.

5.8 Chemical trends and melt evolution

Due to the lack of general trends in the core-to-rim direction in the clinopyroxene crystals, no extensive melt fractionation by another phase is inferred to have occurred during their growth. While a variation was seen in REEs, Zr, Hf and Y in line A1a-5 (see appendix C fig 5), no other line records this variation and it can therefore not be used as an indicator for varying concentrations of these elements in the melt. Rather, it is possible that the variation is a result of crystal kinetics related to the subsectors.

A decrease of the Sr/Nd_(liq) ratio would suggest plagioclase fractionation since Sr is commonly incorporated into plagioclase (see section 2.2.2); similarly the same process would result in an increase of the Ba/Sr_(liq) ratio and a decrease of the Eu/Sm_(liq) ratio. The lack of trend in these ratios indicate that the majority of plagioclase crystals did not form as the crystallization of the clinopyroxene crystals was undergoing, but rather late in the crystallization sequence. The exception to this is line A2a-1 which experiences a slight Sr/Nd_(liq) decrease towards the rim, suggesting either Sr_(liq) depletion, Nd_(liq) enrichment or a combination of the two. However, considering the uniqueness of this observation it cannot be used as an indicator of plagioclase fractionation. Furthermore, the constant nature of the Eu/Sm_(liq) ratio provide additional indication of the lack of plagioclase fractionation.

Regarding the REEs, the higher concentration of LREEs in relation to HREEs indicates REE frac-

tionation. However, the lack of a general trend of the $\text{La/Yb}_{(\text{liq})}$ ratio in the clinopyroxene crystals suggests that this fractionation did not occur to a large extent during the growth of these crystals. Rather, the differences in concentration might indicate fractionation at an earlier stage or might reflect the chemistry and degree of melting of the source. However, the increase of incompatible elements in the clinopyroxene rims point to enrichment of these elements in the melt late in the crystallization sequence; however, the trace element composition of the rims is difficult to evaluate due to analysis resolution and matrix interference.

In conclusion, while the melt likely was somewhat fractionated by the growth of the clinopyroxene crystals (affecting compatible elements such as Sc and Cr), fractionation by another phase is not recorded in the analysed crystals. This suggests that the crystals grew early in the crystallization sequence and likely did not grow simultaneously with other phases to any large extent, consistent with their phenocrystic appearance (see section 5.9.1 for discussion regarding the use of the term “phenocryst”) and the porphyritic nature of the sample. The rims are however exceptions to this, since the multiple saturation of the system likely resulted in more extensive fractionation by several phases. Also, despite the probable occurrence of fractionation during the evolution of the magma, the ultramafic and silica undersaturated nature of the samples indicate, as mentioned in section 5.1, that the system was likely relatively unevolved at the time of the eruption. However, if comparing with the composition of the A1b core, it is clear that the A1b core has a higher concentration of Ni, for example. If considering the core as genetically related to the melt from which the concentrically zoned mantle was formed (see discussion in section 5.9.1), it could indicate Ni depletion caused by early olivine fractionation. Thus, fractionation and evolution of the system before the crystallization of the analysed clinopyroxene crystals cannot be disregarded.

5.9 Interpretations regarding magmatic history and open system processes

5.9.1 Origin and growth histories of the clinopyroxene crystals

Considering the difference between the concentrically zoned and the sector zoned crystals regarding type of zoning, rims, general chemistry and other features such as the resorbed core of A1b, the crystals are interpreted to belong to two different generations or two different origins, inferring that magma mixing occurred in the system. This claim is supported by the following observations: (1) Despite the proximity of the four crystals to each other in the sample they display widely different crystallographic features. It is not feasible to argue that crystals formed simultaneously and under the same temperature, pressure and in the same liquid composition, would respond in two completely different manners, with one crystal producing sector zoning and another producing concentric zoning. Therefore, it can be argued that A1a and A2b were formed under one set of circumstances, while A1b and A2a were formed under another. (2) While the rims are similar in all crystals, the variations re-

garding the light band inside of the rims, for example the “double rims” in A1b and the seemingly higher frequency of two light bands in the concentrically zoned crystals, cannot be disregarded. While it can be argued that these differences are too small and too inconsistent to alone indicate differences in generation or origin, they may act as further verification of other observations. (3) While the chemistry of the concentrically zoned crystals is similar to that of the sector zoned crystals in that they seem to be governed by the same coupled substitution, the fact that the concentrically zoned crystals display a varied chemical composition, while the sector zoned crystals rather display two separate chemical compositions, further highlights the differing processes affecting the crystals. (4) The presence of the partially resorbed core in A1b indicates a complex growth history for the concentrically zoned crystals, one that is not indicated in the sector zoned crystals due to the homogenous nature of the sectors in the core-to-rim direction.

The most important observations acting as evidence for two different generations or origins are (1) and (4), collectively suggesting that the concentrically zoned crystals experienced a longer and more complex growth history, under other environmental factors, than the sector zoned crystals. Furthermore, the complicated growth history indicates a relatively long residence time. Taking the results and discussions presented in this thesis into account, a possible growth history for these crystals can be pieced together (fig 27). This history can broadly be divided into three stages: Resorption and recrystallization of the primitive core, crystallization of the concentrically zoned mantle and magmatic recharge event, and lastly the crystallization of the rim. Starting with the partially resorbed core, this core likely represents the oldest part of the crystal, and was once formed in a primitive and unevolved magmatic system in which that primitive composition was in equilibrium with the liquid. This was likely either in an early stage of the magmatic system in which it is found today, meaning it would be regarded as an antecryst, or in another magmatic system from which it was moved to the magmatic system in which it is found, meaning that it would be regarded as a xenocryst. In any case, the phase was at some point in time in disequilibrium with the surrounding liquid, resulting in resorption and replacement of the phase as a response to changes such as temperature, pressure and liquid composition. This resulted in the irregular centre of the concentrically zoned crystals as well as the formation of the small inclusions therein. For A1b, the resorption of the primitive phase was never completed, thus resulting in the partially resorbed core observed in the crystal. At a certain point in time, the environment affecting the crystals changed, marked by the onset of the concentric zoning. Discussed in section 5.3, the cause for the concentric zoning cannot be determined for certain from the results in this thesis; however, it is likely that a convective magma chamber is at least partly the reason for the concentric zoning, resulting in bands with chemistries representing different temperatures and, perhaps, pressures. Shortly after the onset of the concentric zoning, a magma recharge of hot primitive magma with high concentrations of Cr resulted in the Cr spike, as well as the wavy nature of

the Cr-rich growth band in A2a. After this recharge event, the crystals continued to grow and produce concentric zoning. The system was successively depleted of Cr, and thus the Cr concentration of the concentrically zoned crystals decreases in the core-to-rim direction. As mentioned before, it is possible that smaller secondary recharges occurred at this time. The crystallization continued until the formation of the rim, likely a response to decompression related to the eruption.

In contrast, the sector zoned crystals seem to have had a rather straightforward growth history, with their chemistry only affected by the possible magma chamber convection towards the end of the crystallization resulting in the concentric zoning of A2b, and the magma recharge creating the Cr spikes in the rims. This leads to the conclusion that the concentrically zoned crystals likely started to form earlier than the sector zoned crystals. Furthermore, if assuming that the sector zoned crystals are relatively young, they can be interpreted to be formed in, and genetically related, to the melt in which they are found, i.e. they are interpreted as phenocrysts. If assuming that this is true, it is not feasible to believe that the concentrically zoned crystals share the same relation to the melt. This as well is a reason behind the claim that these crystals formed earlier in the evolution, i.e. represents an older generation of clinopyroxenes, or in another level of the magmatic system. In both cases they would likely be referred to as antecrysts, indicating that they are genetically related to, but not formed from, the melt in question. Additionally, as with the primitive core, it is also possible that they are xenocrysts originating from another magmatic system and without any genetic re-

lation to the melt and the sector zoned phenocrysts. Whether they are to be called antecrysts or xenocrysts, the lack of disequilibrium textures in the concentric mantles and the rims suggest that they did not reside in a liquid with which they were in disequilibrium for an extended amount of time. Rather, they are interpreted to have been mixed with the melt close to the eruption event.

5.9.2 Eruption event and rim formation

Assuming that the concentrically zoned crystals and the sector zoned phenocrysts have different origins, genetically related or not, they were erupted at the same eruption event and therefore it is reasonable to believe that the rims of all crystals formed simultaneously, as supported by the similarity of the rim chemistries. This further constrains the timing of the magma mixing inferred above to have occurred before the rim formation. Similarly, all crystals display the light band which might be related to a pressure decrease. Considering the Teno massif was subject to at least two mass wasting events—The Masca Collapse and the Carrizales Collapse—both preceding eruption of ankaramite magmas (Longpré et al., 2009), it can be argued that the mass wasting acted as the trigger for the eruption. A load decrease as extensive as that from a mass wasting event would affect the underlying magmatic system by lowering the pressure exerted on it, which might explain the light band. In other words, the light band might have formed as a result of the pressure decrease caused by the mass wasting event, which might have triggered the eruption and subsequently

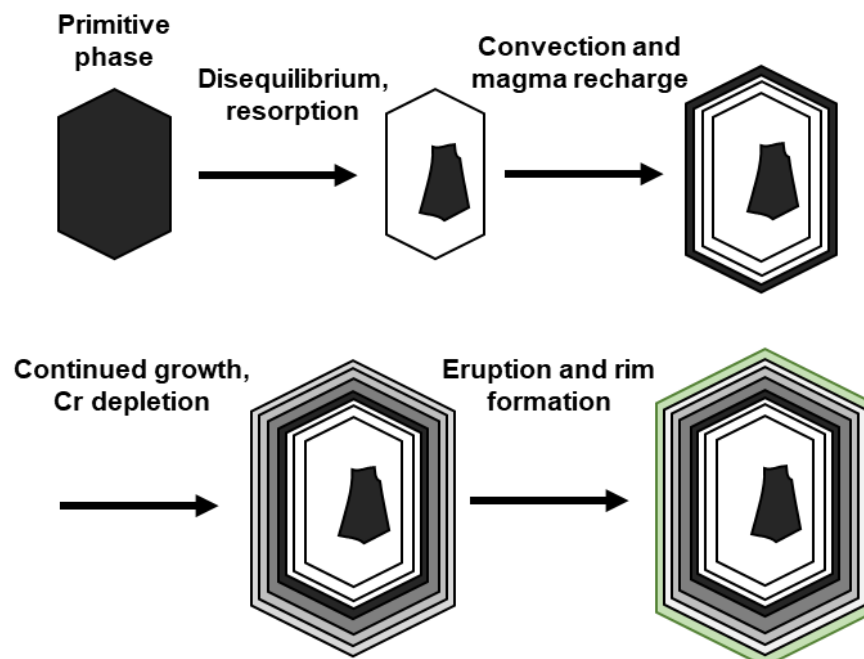


Fig 27: Simplified sketch of a possible growth history for the concentrically zoned crystals, specifically using crystal A1b as an example. A primitive Cr-rich phase (dark grey) in disequilibrium results in resorption and replacement of clinopyroxene with a new chemical composition (white). Concentric zoning starts to form, likely at least partly due to convection, and magma recharge occurs (dark grey band). The crystal continues to grow, successively depleting the system of Cr (lighter shades of grey), until eruption induced decompression and ascent and rim formation.

resulted in rim formation. If this is true, the “double rims” in A1b and the inferred higher frequency of two light bands in both concentrically zoned crystals could possibly indicate that these crystals have experienced two mass wasting events. Due to the dense nature of the deep ankaramite magmas, it is only natural to assume that as an eruption occurs, the magma chamber is not necessarily completely emptied. Relating this to the fact that the Teno massif experienced two mass wasting events, it is possible that the concentrically zoned crystals formed before the Masca Collapse but never left the magma chamber. Thus, they genetically belong to the older ankaramite formation. These crystals stayed in the magmatic system during the formation of the sector zoned phenocrysts, and both generations experienced the Carrizales Collapse and the same eruption event. Thus, the analysed sample would belong to the younger ankaramite formation. It is however important to note that this model is highly speculative and should not be taken to be the absolute truth. Another possible explanation is that the light band formed simply due to the eruption event, and the reason that the interval is different from the rest of the rim is that it lacks the compositional effects of the multiple saturation due to it being slightly delayed relative to the onset of the decompression and ascent. In this case, it is not possible to determine if the concentrically zoned crystals indeed belong to another generation or if they simply originate from another part of the magmatic system and formed around the same time as the sector zoned phenocrysts. However, since rim inclusions start to occur at the light band this is not considered likely, since it indicates that the system was multiply saturated already at the formation of the light band.

Finally, an additional discussion is needed for the magma recharge events recorded in the sector zoned phenocrysts. The location of the Cr spikes close before the formation of the light band and the Al-poor rim would suggest that the magma recharge and the onset of decompression and ascent, and therefore the mass wasting events, might be related. This creates three different possibilities: First of all, it cannot be ruled out that the position of the Cr spike in relation to the rim is a random occurrence and in fact not related, despite that this possibility can be regarded as implausible when taking into account previous research (e.g. Ubide & Kamber, 2018). Secondly, the process that caused the onset of the formation of the rims – in this case possibly interpreted to be the mass wasting event – may also have triggered the magma recharge event; and thirdly, the magma recharge event itself may have triggered the mass wasting event by destabilizing the system (see section 2.1.2). Which one of these alternatives that is true is however not possible to determine from these results; however, it can be argued that if considered possible that the mass wasting event caused the magma recharge, the Cr spikes in A1a are located too far from the edge of the phenocryst for it to be feasible, since it is interpreted that the mass wasting event caused the formation of the rim. Therefore, it would be considered more likely that the magma recharge triggered the mass wasting event. Although, relating the magma recharge to the eruption trigger is problematic due to the lack of Cr spikes in the rims of

the concentrically zoned crystals. However, this can be explained if assuming that these crystals were located in a different part or level of the magmatic system than the sector zoned phenocrysts. If the magma recharge occurred close to the location of the sector zoned phenocrysts, it is only natural that these would incorporate more Cr into their structure than crystals located in another part of the magmatic system. This is further supported by the fact that small increases in Cr concentration were seen in some rims of the concentrically zoned crystals. The question of location in relation to magma recharge boils down to the amount and rate of convection in the magma chamber, and whether this convection reaches beyond the level in which the recharge occurs. Also, it involves the question of when the previously mentioned magma mixing occurred that brought the two types of clinopyroxene crystals together. If assuming that the concentrically zoned crystals did not record the magma recharge due to being located in a different part of the magma chamber, the timing of the magma mixing can be constrained to have occurred after the magma recharge and before the actual eruption.

In conclusion, it is possible to relate the magma recharge to the eruption as done in Ubide & Kamber (2018); however, the discussion above is to a large extent speculations and more studies are required to confirm a connection.

6 Conclusions

While the results in this thesis cannot sufficiently support any interpretation regarding eruption or clinopyroxene growth history with confidence, the following can be regarded as certain: (1) the sector zoning consists of Al+Ti sectors (prism sectors) and Mg+Si sectors (hourglass sectors), controlled by the coupled substitution $[Mg+Si] \rightarrow [Al+Ti]$. Furthermore, trace elements generally have lower partition coefficients in the hourglass sectors. (2) The concentrically zoned crystals have experienced longer and more complicated growth histories than the sector zoned crystals, with stages of resorption and magma chamber convection. (3) The rims of all crystals likely grew simultaneously in the same eruption event, as suggested by the similarity of the chemical compositions. (4) Signs of at least two magma recharge events are recorded in the crystals in the form of Cr spikes, reflecting the addition of new Cr-rich primitive magma.

As for the interpretations, the four clinopyroxene crystals analysed in this thesis display widely different features, dividing them into two groups: sector zoned crystals and concentrically zoned crystals. The differences in zoning and, to a certain extent, chemistry, has led to the interpretation that the two groups either belong to two generations of clinopyroxene or have two different origins, since it is apparent that they were affected by different processes during growth. The primitive nature of the residual core of concentrically zoned A1b further supports this interpretation, indicating that the concentrically zoned crystals experienced longer and more complicated growth histories than the sector zoned crystals. While the sector zoned crystals are interpreted to have grown during a short time frame at a high growth rate, favouring the formation of sector zoning, the concentrically zoned crys-

tals likely grew in multiple stages of resorption and crystallisation in a convecting magma chamber. Thus, the sector zoned crystals are interpreted as phenocrysts, while the concentrically zoned crystals rather should be regarded as antecrysts or xenocrysts, highlighting that they either formed earlier in time, crystallized in another part of the magmatic system or originate from an entirely different magmatic system. This in turn points to instances of magma mixing in the system.

While the clinopyroxene crystals are contrasting in terms of zoning and suggested growth histories, the rims are similar in all four crystals, leading to the assumption that the rims formed simultaneously and that the magma mixing occurred before the rim formation. The Al-poor nature of the rim is interpreted to be caused by multiple saturation of the system as a response to decompression and ascent, resulting in plagioclase crystallization and Al depletion. If the Al-poor rim is to be interpreted as the decompression and ascent related to the eruption event, the light band inside of the rim can possibly be related to the eruption trigger. If this light band can indeed be interpreted to represent an instance of pressure decrease – as suggested by the contrasting chemistry to the rim and the occasional Al increase at the light band – it can be argued to be a recorder of the mass wasting event and the load decrease that followed. Furthermore, if continued research supports the observations that the concentrically zoned crystals tend to exhibit a higher frequency of sites with two light bands than the sector zoned phenocrysts, it would suggest that two instances of pressure decrease might have been recorded in the concentrically zoned crystals. As the Teno massif experienced at least two major mass wasting events, these pressure decreases could correspond to these two events, if the concentrically zoned crystals are regarded as part of an older ankaramite magma. However, this hypothesis cannot be proved with the results in this thesis, and the true cause for the light band is a subject of speculation.

The Cr spikes recorded during the LA-ICP-MS analyses are interpreted to represent events of magma recharge, i.e injection of primitive magma into the magma chamber, due to the high compatibility of Cr in clinopyroxene. Using the results in this thesis it can be argued that at least two different magma recharge events occurred during the crystallization of these clinopyroxene crystals, with one event recorded in the rims of the sector zoned phenocrysts and another in the interior of the concentrically zoned crystals. The fact that the two groups of crystals do not seem to have recorded the same magma recharge events further supports the interpretation that they belong to different generations or have different origins, and also further constrains the timing of the magma mixing to have occurred after the Cr spike and before the rim formation.

According to previous research, the two mass wasting events and subsequent load decrease resulted in the eruption of the deep and dense ankaramite magmas. If the mass wasting event is to be regarded as the eruption trigger, the location of the Cr spikes in the rims of the sector zoned phenocrysts would pose the question if the two are related. If any, the most likely

relation between the two is argued to be that the magma recharge event destabilized the system and therefore triggered the mass wasting event, which in turn triggered the eruption. However, it is important to note that this hypothesis cannot be fully supported solely based on the results in this thesis.

6.1 Recommended future research

The limitations regarding interpretations in this thesis can partly be attributed to the fact that only one sample was used, from which only four clinopyroxene crystals were analysed. This limitation was necessary due to time restrictions; however, a study focusing on a larger number of crystals would yield more reliable results. This is especially true for more inconsistent features, for example the light band inside of the rims. Additionally, a bigger study focusing on several samples would benefit from a more systematic sampling, specifically making sure to sample more than one ankaramite formation and compare the results between the formations.

There is also need for continued chemical analyses in order to validate the results presented here. For example, more LA-ICP-MS analyses are required to determine the actual location of the Cr spikes in A2b that appear to be located in the matrix. Furthermore, time restrictions inhibited additional EBSD analyses. Carrying out EBSD analyses on all crystals would be beneficial in order to constrain the orientation of the crystal and how it affects the appearance of the zoning.

In order to with more certainty constrain the eruption trigger, eruption history and clinopyroxene growth history it is suggested to perform geothermobarometry. Using this method would give insight into the crystallisation depth and temperature of the crystals, and could further be used to evaluate whether the crystals were formed in different locations of the magmatic system or simply belong to different generations or entirely different magmatic systems.

7 Acknowledgments

A big thank you to my supervisor Anders Scherstén for help and support during the course of this project. I also want to thank Paula Lindgren and Anders Plan for help with analyses and interpretations regarding the EBSD analyses, and Tomas Naeraa for the much needed help with LA-ICP-MS analyses and processing. Finally, I want to thank Ulf Söderlund for reading through the thesis and answering my questions.

8 References

- Adam, J. & Green, T. H., 1994: The effects of pressure and temperature on the partitioning of Ti, Sr and REE between amphibole, clinopyroxene and basanitic melts. *Chemical Geology* 117, 219-233.
- Ancochea, E., Fuster, J. M., Ibarrola, E., Cendrero, A., Coello, J., Hernan, F., Cantagrel, J. M. & Jamond, C., 1990: Volcanic evolution of the island of Tenerife (Canary Islands) in the light of new K-Ar data. *Journal of Volcanology and Geothermal Research* 44, 234-249.
- Anguita, F. & Hernán, F., 1975: A propagating fracture model versus a hot spot origin for the

- Canary islands. *Earth and Planetary Science Letters* 27, 11-19.
- Anguita, F. & Hernán, F., 2000: The Canary Islands origin: a unifying model. *Journal of Volcanology and Geothermal Research* 103, 1-26.
- Araña, V. & Ortiz, R., 1991: The Canary Islands: Tectonics, Magmatism and Geodynamic Framework. In: A. B. Kampunzu & L. R. T (eds.) *Magmatism in Extensional Structural Settings*. Berlin, Heidelberg, Springer. 209-249 pp.
- Arimenti, P., Tonarini, S., Innocenti, F. & D'orazio, M., 2007: Mount Etna pyroxene as tracer of petrogenetic processes and dynamics of the feeding system. In: L. Beccaluva, G. Bianchini & M. Wilson (eds.) *Cenozoic Volcanism in the Mediterranean Area*. Geological Society of America Special Paper 418. 265-276 pp.
- Baudouin, C., France, L., Boulanger, M., Dalou, C. & Devidal, J.-L., 2020: Trace element partitioning between clinopyroxene and alkaline magmas: parametrization and role of M1 site on HREE enrichment in clinopyroxenes. *Contrib Mineral Petrol* 175.
- Blundy, J. & Wood, B., 2003: Partitioning of trace elements between crystals and melts. *Earth and Planetary Science Letters* 210, 383-397.
- Bougault, H. & Hekinian, R., 1974: Rift valley in the Atlantic Ocean near 36 ° 50'N: Petrology and geochemistry of basaltic rocks. *Earth and Planetary Science Letters* 24, 249-261.
- Carracedo, J. C., Day, S., Guillou, H., Rodríguez-Badiola, E., Canas, J. A. & Pérez-Torrado, F. J., 1998: Hotspot volcanism close to a passive continental margin: the Canary Islands. *Geol. Mag.* 135, 591-604.
- Carracedo, J. C., Guillou, H., Nomade, S., Rodríguez-Badiola, E., Pérez-Torrado, F. J., Rodríguez-González, A., Paris, R., Troll, V. R., Wiesmaier, S., Delcamp, A. & Fernández-Turiel, J. L., 2011: Evolution of ocean-island rifts: The northeast rift zone of Tenerife, Canary Islands. *GSA Bulletin* 123, 562-584.
- Carracedo, J. C. & Troll, V. R., 2016: *The Geology of the Canary Islands*. Elsevier. 636 pp.
- Clauge, D. A. & Dalrymple, G. B., 1987: The Hawaiian-Emperor volcanic chain. Part 1. Geologic evolution. *US Geol Sur Prof Pap* 1350, 5-54.
- Downes, M. J., 1974: Sector and Oscillatory Zoning in Calcic Augites from M. Etna, Sicily. *Contrib. Mineral. Petrol.* 47, 187-196.
- Dunn, T., 1987: Partitioning of Hf, Lu, Ti, and Mn between olivine, clinopyroxene and basaltic liquid. *Contrib Mineral Petrol* 96, 476-484.
- Durrant, S. F., 1999: Laser ablation inductively coupled plasma mass spectrometry: achievements, problems, prospects. *J. Anal. At. Spectrom.* 14, 1385-1403.
- Foley, S. F., Jackson, S. E., Fryer, B. J., Greenough, J. D. & Jenner, G. A., 1996: Trace element partition coefficients for clinopyroxene and phlogopite in an alkaline lamprophyre from Newfoundland by LAM-ICP-MS. *Geochimica et Cosmochimica Acta* 60, 629-638.
- Forsythe, L. M., Nielsen, R. L. & Fisk, M. R., 1991: New experimentally determined clinopyroxene-melt high field strength element partition coefficients. *Eos (Trans. Am. Geophys. Union)* 72, 548.
- Freer, R., 1981: Diffusion in Silicate Minerals and Glasses: A Data Digest and Guide to the Literature. *Contrib Mineral Petrol* 76, 440-454.
- Ginibre, C., Kronz, A. & Wörner, G., 2002: High-resolution quantitative imaging of plagioclase composition using accumulated backscattered electron images: new constraints on oscillatory zoning. *Contrib Mineral Petrol* 142, 436-448.
- Goldschmidt, V. M., 1937: The Principles of Distribution of Chemical Elements in Minerals and Rocks. *Chem. Soc.*, 655-672.
- Goldstein, J. I., Newbury, D. E., Michael, J. R., Ritchie, N. W. M., Scott, J. H. J. & Joy, D. C., 2018: *Scanning Electron Microscopy and X-Ray Microanalysis*. Springer. 550 pp.
- Green, T. H., 1994: Experimental studies of trace-element partitioning applicable to igneous petrogenesis in Sedona 16 years later. *Chemical Geology* 117, 1-36.
- Guillou, H., Carracedo, J. C., Paris, R. & Pérez-Torrado, F. J., 2004: Implications for the early shield-stage evolution of Tenerife from K/Ar ages and magnetic stratigraphy. *Earth and Planetary Science Letters* 222, 599-614.
- Hack, P. J., Nielsen, R. L. & Johnston, A. D., 1994: Experimentally determined rare-earth element and Y partitioning behavior between clinopyroxene and basaltic liquids at pressures up to 20 kbar. *Chemical Geology* 117, 89-105.
- Hart, S. R. & Dunn, T., 1993: Experimental cpx/melt partitioning of 24 trace elements. *Contrib Mineral Petrol* 113, 1-8.
- Hauri, E. H., Wagner, T. P. & Grove, T. L., 1994: Experimental and natural partitioning of Th, U, Pb and other trace elements between garnet, clinopyroxene and basaltic melts. *Chemical Geology* 117, 149-166.
- Hollister, L. S. & Gancarz, A. J., 1971: Compositional sector-zoning in clinopyroxene from the Narce area, Italy. *The American Mineralogist* 56, 959-979.
- Honjo, S. & Berggren, W. A., 1967: Scanning Electron Microscope Studies of Planktonic Foraminifera. *Micropaleontology* 13, 393-406.
- King, S. D., 2007: Hotspots and edge-driven convection. *Geology* 35, 223-226.
- Klein, C. & Philpotts, A., 2013: *Earth Materials: Introduction to Mineralogy and Petrology*. Cambridge University Press, Cambridge. 536 pp.
- Klügel, A., Hoernle, K. A., Schmincke, H.-U. & White, J. D. L., 2000: The chemically zoned 1949 eruption on La Palma (Canary Islands): Petrologic evolution and magma supply dynamics of a rift zone eruption. *Journal of Geophysical Research* 105, 5997-6016.

- Kosler, J., 2007: Laser ablation ICP-MS - a new dating tool in Earth science. *Proceedings of the Geologists' Association* 118, 19-24.
- Kushiro, I., 1960: Si-Al relation in clinopyroxenes from igneous rocks. *American Journal of Science* 258, 548-554.
- Leonhardt, R. & Soffel, H. C., 2006: The growth, collapse and quiescence of Teno volcano, Tenerife: new constraints from paleomagnetic data. *Int J Earth Sci* 95, 1053-1064.
- Leung, I. S., 1974: Sector-Zoned Titanaugites: Morphology, Crystal Chemistry, and Growth. *American Mineralogist* 59, 127-138.
- Longpré, M.-A., Troll, V. R. & Hansteen, T. H., 2008: Upper mantle magma storage and transport under a Canarian shield-volcano, Teno, Tenerife (Spain). *Journal of Geophysical Research* 113.
- Longpré, M.-A., Troll, V. R., Walter, T. R. & Hansteen, T. H., 2009: Volcanic and geochemical evolution of the Teno massif, Tenerife, Canary Islands: Some repercussions of giant landslides on ocean island magmatism. *Geochem. Geophys. Geosyst.* 10.
- Matsui, Y., Onuma, N., Nagasawa, H., Higuchi, H. & Banno, S., 1977: Crystal structure control in trace element partition between crystal and magma. *Bulletin de la Société française de Minéralogie et de Cristallographie* 100, 315-324.
- Montelli, R., Nolet, G., Dahlen, F. A., Masters, G., Engdahl, E. R. & Hung, S.-H., 2003: Finite-Frequency Tomography Reveals a Variety of Plumes in the Mantle. *Science* 303, 338-343.
- Morimoto, N., 1988: Nomenclature of Pyroxenes. *Mineralogy and Petrology* 39, 55-76.
- Perinelli, C., Mollo, S., Gaeta, M., De Cristofaro, S.P., Palladino, D.M., Arimenti, P., Scarlato, P. & Putirka, K. D., 2016: An improved clinopyroxene-hygrometer for etnean magmas and implications for eruption triggering mechanisms. *American Mineralogist* 101, 2774-2777.
- Prior, D. J., Boyle, A. P., Brenker, F., Cheadle, M. C., Day, A., Lopez, G., Peruzzo, L., Potts, G. J., Reddy, S., Spiess, R., Timms, N. E., Trimby, P., Wheeler, J. & Zetterström, L., 1999: The application of electron backscatter diffraction and orientation contrast imaging in the SEM to textural problems in rocks. *American Mineralogist* 84, 1741-1759.
- Purton, J. A., Allan, N. L. & Blundy, J. D., 1997: Calculated solution energies of heterovalent cations in forsterite and diopside: Implications for trace element partitioning. *Geochimica et Cosmochimica Acta* 61, 3927-3936.
- Putirka, K. D., 2008: Thermometers and Barometers for Volcanic Systems. In: K. D. Putirka & F. J. Tepley III (eds.) *Minerals, Inclusions and Volcanic Processes*. Reviews in Mineralogy & Geochemistry 69. 61-120 pp.
- Rollinson, H., 1993: *Using geochemical data: evaluation, presentation, interpretation*. Longman Singapore Publishers, Harlow, England. 352 pp.
- Schmincke, H. U., 1969: Ignimbrite Sequence on Gran Canaria. *Bull Volcanol* 33, 1199-1219.
- Skulski, T., Minarik, W. & Watson, E. B., 1994: High-pressure experimental trace-element partitioning between clinopyroxene and basaltic melts. *Chemical Geology* 117, 127-147.
- Streck, M. J., 2008: Mineral Textures and Zoning as Evidence for Open System Processes. *Reviews in Mineralogy & Geochemistry* 69, 595-622.
- Thirlwall, M. F., Singer, B. S. & Marriner, G. F., 2000: $^{39}\text{Ar}\pm^{40}\text{Ar}$ ages and geochemistry of the basaltic shield stage of Tenerife, Canary Islands, Spain. *Journal of Volcanology and Geothermal Research* 103, 247-297.
- Ubide, T. & Kamber, B. S., 2018: Volcanic crystals as time capsules of eruption history. *Nature Communications* 9, 1-12.
- Ubide, T., Mollo, S., Zhao, J., Nazzari, M. & Scarlato, P., 2019: Sector-zoned clinopyroxene as a recorder of magma history, eruption triggers, and ascent rates. *Geochimica et Cosmochimica Acta* 251, 265-283.
- Van Orman, J. A., Grove, T. L. & Shimizu, N., 2001: Rare earth element diffusion in diopside: influence of temperature, pressure, and ionic radius, and an elastic model for diffusion in silicates. *Contrib Mineral Petrol* 141, 687-703.
- Verhoogen, J., 1962: Distribution of titanium between silicates and oxides in igneous rocks. *American Journal of Science* 260, 211-220.
- Wiesmaier, S., Troll, V. R., Carracedo, J. C., Ellam, R. M., Bindeman, I. & Wolff, J. A., 2012: Bimodality of Lavas in the Teide-Pico Viejo Succession in Tenerife - the Role of Crustal Melting in the Origin of Recent Phonolites. *Journal of Petrology* 53, 2465-2495.
- Villemant, B., Jaffrezic, H., Joron, J. L. & Treuil, M., 1981: Distribution coefficients of major and trace elements; fractional crystallization in the alkali basalt series of Chaîne des Puys (Massif Central, France). *Geochimica et Cosmochimica Acta* 45, 1997-2016.
- Wilson, J. T., 1963: A Possible Origin of the Hawaiian Islands. *Canadian Journal of Physics* 41, 863-870.
- Winter, J. D., 2014: *An Introduction to Igneous and Metamorphic Petrology*. Prentice-Hall Inc. 739 pp.

Fig 4: Reprinted from *Geochimica et Cosmochimica Acta*, Vol. 251, Ubide, T., Mollo, S., Zhao, J.-x., Nazzari, M., Scarlato, P., 265-283, 2019, with permission from Elsevier; as modified from *American Mineralogist*, vol. 59, Leung, I.S., 127-138, 1974, with permission from Mineralogical Society of America.

Appendix A - Index of element abbreviations and periodic table

Element abbreviations and atomic numbers for elements presented in table 1.

Major and minor elements

<i>Abbreviation</i>	<i>Name</i>	<i>Atomic number</i>
Na	Sodium	11
Mg	Magnesium	12
Al	Aluminium	13
Si	Silicon	14
Ca	Calcium	20
Ti	Titanium	22
Fe	Iron	26

Trace elements

Rare earth elements (REE)

<i>Abbreviation</i>	<i>Name</i>	<i>Atomic number</i>
La	Lanthanum	57
Ce	Cerium	58
Pr	Praseodymium	59
Nd	Neodymium	60
Pm	Promethium	61
Sm	Samarium	62
Eu	Europium	63
Gd	Gadolinium	64
Tb	Terbium	65
Dy	Dysprosium	66
Ho	Holmium	67
Er	Erbium	68
Tm	Thulium	69
Yb	Ytterbium	70
Lu	Lutetium	71

Transition metals

<i>Abbreviation</i>	<i>Name</i>	<i>Atomic number</i>
Sc	Scandium	21
V	Vanadium	23
Cr	Chromium	24
Co	Cobalt	27
Ni	Nickel	28

Other elements

<i>Abbreviation</i>	<i>Name</i>	<i>Atomic number</i>
Rb	Rubidium	37
Sr	Strontium	38
Y	Yttrium	39
Zr	Zirconium	40
Nb	Niobium	41
Ba	Barium	56
Hf	Hafnium	72
Ta	Tantalum	73
Th	Thorium	90
U	Uranium	92

Group →	1	2	3	4	5	6	7	8	9	10	11	12	13	14	15	16	17	18
↓ Period	1	2	3	4	5	6	7	8	9	10	11	12	13	14	15	16	17	18
1	1 H																	2 He
2	3 Li	4 Be											5 B	6 C	7 N	8 O	9 F	10 Ne
3	11 Na	12 Mg										13 Al	14 Si	15 P	16 S	17 Cl	18 Ar	
4	19 K	20 Ca	21 Sc	22 Ti	23 V	24 Cr	25 Mn	26 Fe	27 Co	28 Ni	29 Cu	30 Zn	31 Ga	32 Ge	33 As	34 Se	35 Br	36 Kr
5	37 Rb	38 Sr	39 Y	40 Zr	41 Nb	42 Mo	43 Tc	44 Ru	45 Rh	46 Pd	47 Ag	48 Cd	49 In	50 Sn	51 Sb	52 Te	53 I	54 Xe
6	55 Cs	56 Ba		72 Hf	73 Ta	74 W	75 Re	76 Os	77 Ir	78 Pt	79 Au	80 Hg	81 Tl	82 Pb	83 Bi	84 Po	85 At	86 Rn
7	87 Fr	88 Ra		104 Rf	105 Db	106 Sg	107 Bh	108 Hs	109 Mt	110 Ds	111 Rg	112 Cn	113 Nh	114 Fl	115 Mc	116 Lv	117 Ts	118 Og
Lanthanides	57 La	58 Ce	59 Pr	60 Nd	61 Pm	62 Sm	63 Eu	64 Gd	65 Tb	66 Dy	67 Ho	68 Er	69 Tm	70 Yb	71 Lu			
Actinides	89 Ac	90 Th	91 Pa	92 U	93 Np	94 Pu	95 Am	96 Cm	97 Bk	98 Cf	99 Es	100 Fm	101 Md	102 No	103 Lr			

Fig 1 : Periodic table. Figure by Cepheus, retrieved 27-05-2020 from https://commons.wikimedia.org/wiki/File:Periodic_table.svg

Appendix B – Analytical techniques

Below follows an explanation for the theory behind scanning electron microscopy (SEM) and laser ablation inductively coupled plasma mass spectrometry (LA-ICP-MS)

Scanning electron microscope (SEM)

When using a scanning electron microscope a beam of electrons strikes the sample, causing *secondary electrons* and *backscatter electrons* to be emitted. When analysing a sample using secondary electrons (SE), the instrument detects the electrons that are freed due to the discharge of the sample surface caused by the electron beam. When using backscatter electrons (BSE) for analysing, the instrument detects the electrons from the electron beam as they have been reflected on the sample surface (Honjo & Berggren, 1967). SE analyses provide information on the topography of the sample, while BSE analyses give information about the chemical composition using differences in contrast. A brighter contrast indicates presence and/or higher concentration of heavier elements, while a darker contrast indicates that the medium consists of lighter elements.

Energy dispersive spectrometry (EDS) is used to qualitatively and quantitatively analyse the chemical composition of the sample volume that is analysed. As the electron beam strikes the sample and electrons are emitted, x-ray photons are emitted as well. These photons can be divided into two types: the characteristic x-rays which are specific for certain elements, and the continuum x-rays which create a background to the characteristic x-rays. This method yields an x-ray spectrum which can be measured and the present elements and their concentration can be determined (Goldstein et al., 2018). The abbreviation SEM-EDS indicates that the EDS analyses were performed using a scanning electron microscope.

Electron backscatter diffraction (EBSD) is used when analysing the crystallographic orientations of minerals. As the electron beam strikes the sample, the electrons are diffracted and scattered at different angles depending on how close they pass to an atomic nucleus; the closer they pass, the larger the angle with which they scatter. Due to the relatively wide nature of the electron beam, this interaction will result in electrons being scattered in all trajectories possible. The electrons that are scattered, i.e. BSE, form a band pattern (Kikuchi pattern) that can be viewed on a phosphor screen, thus making it possible to identify zone axes (Prior et al., 1999).

Laser ablation inductively coupled plasma mass spectrometry (LA-ICP-MS)

Mass spectrometry utilizes the mass difference between atoms, using an electromagnet that sort the atoms according to mass as they are fired along a curved tube and deflected. The lighter ions are deflected less than the heavier ions, and as a result a mass spectrum is created. ICP-MS is commonly used for trace element and isotope analyses due to its good precision and accuracy and low detection limits (Rollinson, 1993). Furthermore, the use of laser ablation requires less sample preparation and allows for *in*

situ analyses. The laser beam is deflected at a mirror before it interacts with the sample in the ablation cell. An aerosol of particles is created that is transported to the ICP, in which the aerosol is heated and transformed into ions and atoms. Thereafter, the mass analyzer detects the amount of these ions and atoms (fig 1) (Durrant, 1999; Kosler, 2007). Different kinds of lasers can be used, for example ruby laser and Nd:YAG laser, but the laser used in this thesis is an *excimer laser*. This laser utilizes the creation of excimers, which are dimers that exist in an excited state due to a minimum of the potential energy curve, despite the species being repulsive, and therefore only monomer, in the ground state. Lasing can then be carried out between the higher energy levels of the excimer and the lower energy levels of the ground state monomer (Durrant, 1999).

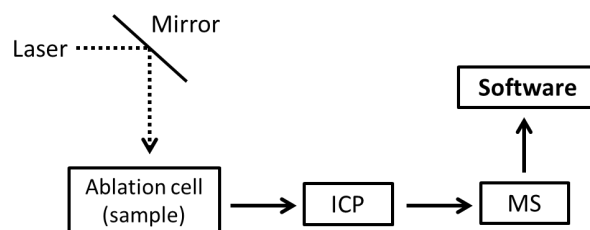


Fig 1: Schematic sketch of the LA-ICP-MS analytical technique. The laser interacts with the sample in the ablation cell, and the aerosol that is created is transported to the inductively coupled plasma (ICP), after which the ions and atoms are detected by the mass analyzer (MS). Finally, the results are analysed using software.

Appendix C – Additional figures and tables

Appendix B is devoted to figures that were not able to be included in the main text, and thus serve as additional information and data.

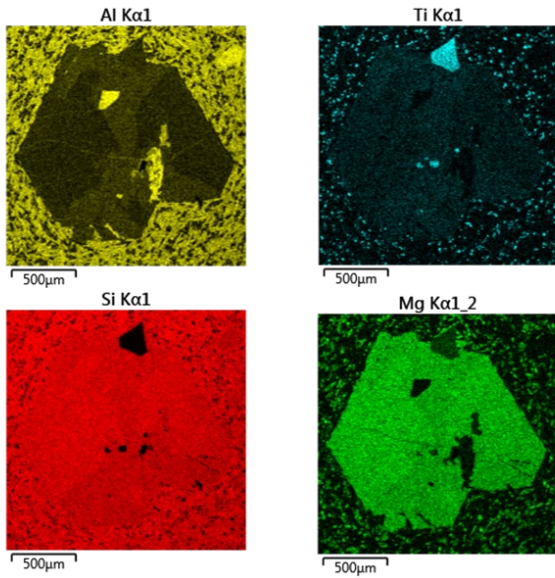


Fig 1: EDS-maps for Al, Ti, Si and Mg illustrating the sector zoning and the irregular zoning of these elements in the A2b crystal.

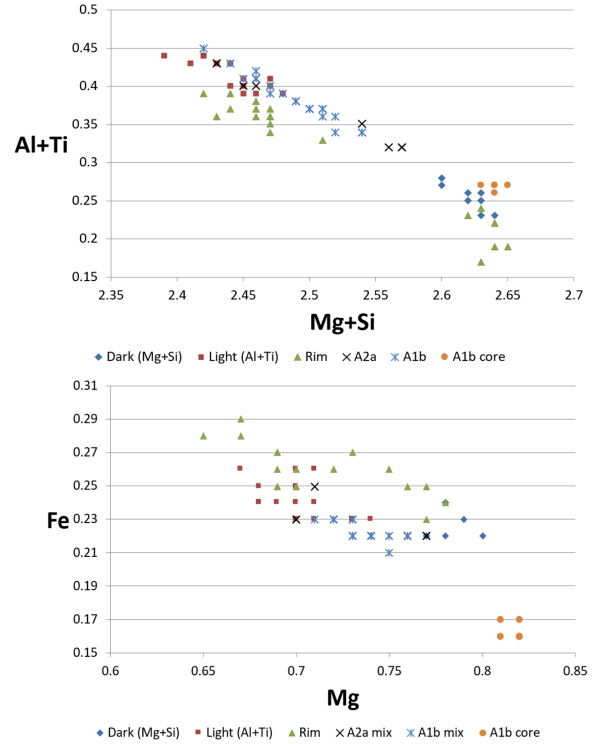


Fig 2: The different chemical compositions present in the four clinopyroxene crystals can be distinguished by plotting (Al+Ti) against (Mg+Si) (upper) and Fe against Mg (lower). Both are plotted in cations. Note the unique composition of the A1b core in the Fe-Mg plot.

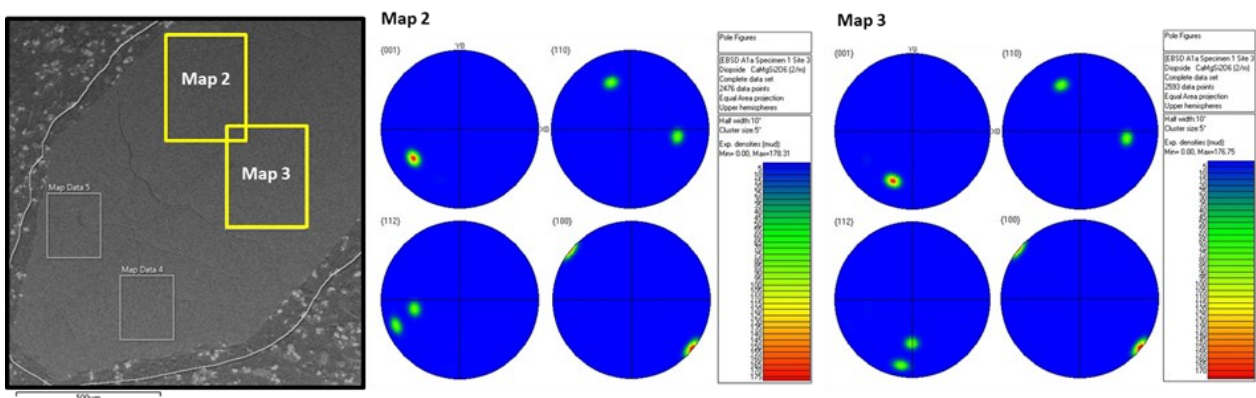


Fig 3: EDS-maps for Al, Ti, Si and Mg illustrating the sector zoning of these elements in the A2b crystal.

Table 1: The difference in trace element concentrations between the Al+Ti and the Mg+Si sector in A2b. The “visible change” column refers to the graphical estimation of the change. The concentrations are based on spot analyses of A2b-spot-4 (Al+Ti) and A2b-spot-5. The “difference” column to the right is colour coded, with green representing an increase and red a decrease, and refers to the difference in concentration between the sectors as calculated with $Difference = C(Al+Ti) - C(Mg+Si)$. As for A1a, most trace elements are enriched in the Al+Ti sector relative to the Mg+Si sector. The exception here is Co which decreases slightly. Cr, Ni and Ba are all below detection limits (LOD) and can therefore not be evaluated.

A2b				
Element	Visible change (graph)	Al+Ti sector (ppm)	Mg+Si sector (ppm)	Difference (ppm)
La	Increase	13.05	6.81	6.24
Ce	Increase	46.8	25.23	21.57
Pr	Increase	8.07	4.71	3.36
Nd	Increase	42	25.1	16.9
Sm	Increase	12.16	7.17	4.99
Eu	Increase	3.77	2.26	1.51
Gd	Increase	11.89	7.41	4.48
Dy	Increase	8.7	5.42	3.28
Er		3.67	2.18	1.49
Yb		2.35	1.31	1.04
Cr		<i>Below LOD</i>	<i>Below LOD</i>	
Ni		<i>Below LOD</i>	<i>Below LOD</i>	
Co		33.6	34.5	-0.9
Ti	Increase	17060	11150	5910
V	Increase	457	326	131
Sc	Increase	60.7	50.6	10.1
Zr	Increase	222	121.2	100.8
Sr	Increase	115.9	91.8	24.1
Y	Increase	36.2	22.6	13.6
Hf	Increase	8.78	4.91	3.87
Ba		<i>Below LOD</i>	<i>Below LOD</i>	
Nb	Increase	1.627	0.666	0.961

Table 2: Calculated relative partition coefficients for the Mg+Si sector used in fig 20, using the Al+Ti sector as standard. The partition coefficients illustrate possible differences in element preference between the sectors, and were calculated with the assumptions that the sector zoning is solely controlled by kinetic processes and that no extensive melt evolution and fractionation occurred during their growth.

Element	Line A1a-1 (average)	Line A1a-1 (median)	A1a spots
Sc	1.068	0.999	1.165
Ti	0.216	0.205	0.275
V	2.394	2.176	2.281
Cr	1.176	0.925	2.740
Co	1.267	1.136	1.087
Ni	2.500	1.890	1.055
Sr	0.118	0.108	0.109
Y	0.347	0.316	0.300
Zr	0.075	0.068	0.081
Nb	0.00357	0.00275	0.00369
Ba	0.00139	0.00022	<i>Below LOD</i>
La	0.037	0.034	0.030
Ce	0.064	0.057	0.054
Pr	0.095	0.087	0.085
Nd	0.143	0.132	0.119
Sm	0.259	0.215	0.181
Eu	0.502	0.394	0.396
Gd	0.385	0.223	0.205
Dy	0.337	0.276	0.271
Er	0.356	0.256	0.238
Yb	0.975	0.267	0.325
Hf	0.180	0.157	0.184

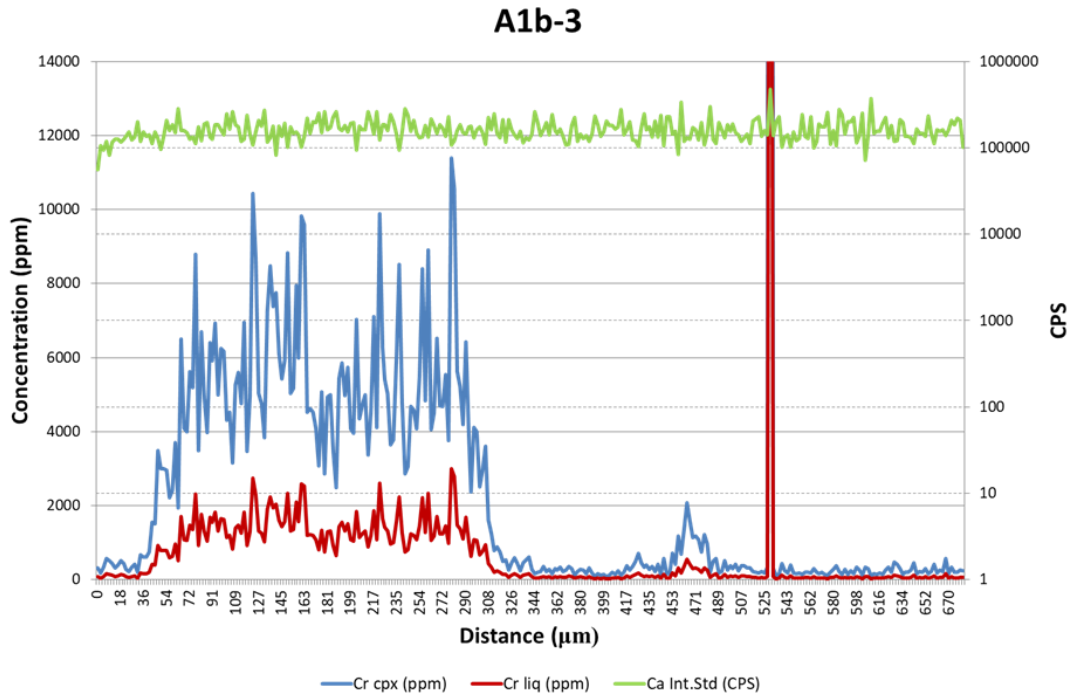


Fig 4: Graph of the Cr concentration along the A1b-3 line. The red line (lower) represents the calculated liquid composition using $D(\text{Cr}) = 3.8$. The blue line (middle) represents the Cr concentration in the clinopyroxene crystal, and lastly the green line (top) is Ca (internal standard) plotted in CPS (counts per second) at the right axis. Note the high Cr concentrations between approximately 40 and 320 μm , as well as the Cr spike at ~ 470 μm . Also observe the lower concentration of Cr in the liquid phase compared to the clinopyroxene crystal.

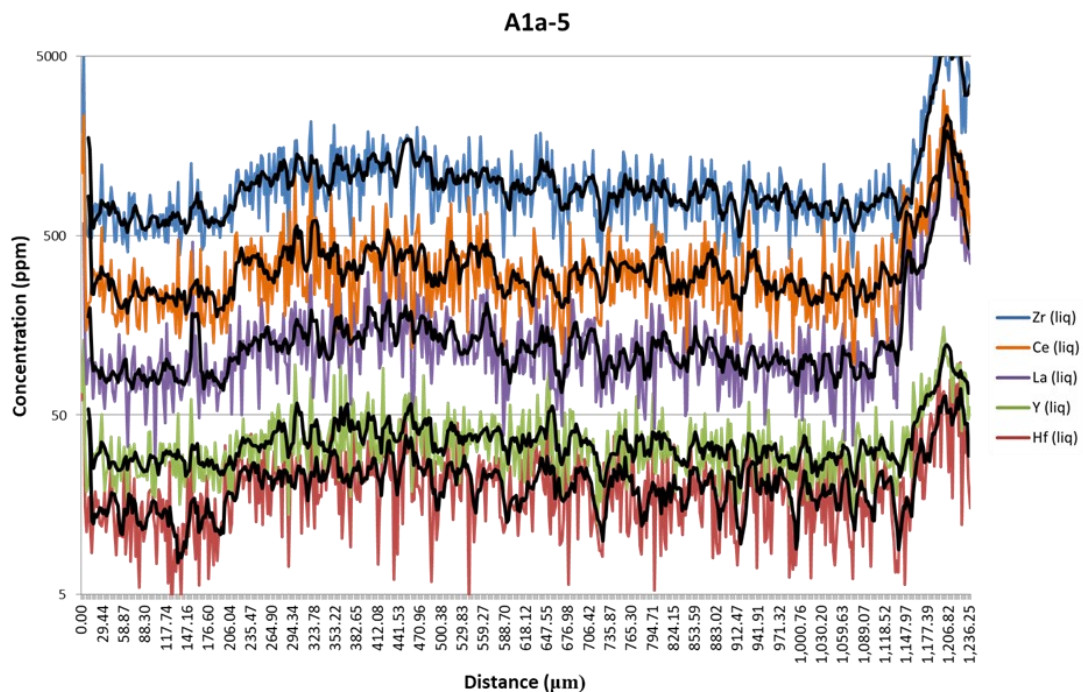


Fig 5: The REEs, Zr, Y and Hf display variation in the Al+Ti sector in line A1a-5. In this graph, the calculated liquid concentrations of a selected number of elements are plotted. In descending order: Zr (blue), Ce (orange), La (purple), Y (green) and Hf (red). All elements are plotted with a moving average of 5. The border between the Mg+Si and Al+Ti sectors is crossed at approx. 200 μm , and the edge of the crystal occurs at approx. 1190 μm . In between these borders, there is a clear decrease of the plotted elements towards the rim.

Appendix D - Results from SEM-EDS analyses

Representative values from SEM-EDS analyses. Cations based on 6 O.

Oxide-%

Analyzed object	Crystal	Al ₂ O ₃	TiO ₂	MgO	SiO ₂	FeOtot	CaO	Na ₂ O	Cr ₂ O ₃	Total
Mg+Si sector	A1a	4.47	2.05	14.21	48.33	7.05	22.38	0.35		98.83
Mg+Si sector	A1a	5.01	1.8	13.95	48.43	7.55	21.71	0.47		98.92
Mg+Si sector	A1a	4.94	2.22	13.64	48.48	7.13	22.01	0.38		98.8
Mg+Si sector	A2b	3.92	1.75	13.68	48.36	7.46	21.48	0.39		97.03
Mg+Si sector	A2b	4.4	1.93	13.65	47.48	7.1	21.12	0		95.69
Mg+Si sector	A2b	4.16	1.89	13.31	47.23	6.73	21.17	0.36		94.83
Al+Ti sector	A1a	7.84	3.14	11.76	44.82	8.06	22.13	0.53		98.28
Al+Ti sector	A1a	7.85	2.76	12.45	44.95	8.1	21.91	0.49		98.5
Al+Ti sector	A1a	7.06	2.66	12.02	43.93	7.35	21.46	0.51		94.99
Al+Ti sector	A2b	6.7	3.15	12.01	46.26	7.63	21.77	0.53		98.06
Al+Ti sector	A2b	6.92	3.08	12.24	45.03	7.99	21.6	0.5		97.36
Al+Ti sector	A2b	7.52	3.47	12.24	46.11	7.9	22.26	0.64		100.14
Al+Ti sector	A2b	7.75	3.6	12.22	46.8	7.55	21.81	0.6		100.33
Rim	A1a	6.44	3.66	11.94	46.03	9.01	21.81	0.6		99.48
Rim	A1a	5.74	3.41	12.19	46.98	8.03	22.09	0.7		99.14
Rim	A1a	3.05	1.97	13.55	50.28	7.94	21.74	0.56		99.2
Rim	A2b	3.85	2.5	13.84	49.55	7.47	21.58	0.43		99.22
Rim	A2b	2.5	2	13.03	50.35	8.54	21.99	0.57		98.98
Rim	A2b	6.05	3.46	12.46	46.88	7.87	21.81	0.5		99.02
Rim	A2b	5.51	3.29	12.31	47.18	8.52	21.88	0.65		99.35
Rim	A2a	5.88	3.7	11.91	46.63	8.8	21.82	0.63		99.37
Rim	A1b	5.6	3.43	12.13	46.36	8.17	21.55	0.58		97.82
Concentric zoning	A2a	7.23	2.72	12.44	45.66	7.73	22.13	0.49		98.39
Concentric zoning	A2a	7.58	3.11	12.57	46.1	7.44	22.67	0.44		99.9
Concentric zoning	A2a	5.47	2.13	13.47	47.24	7.05	22	0.51		98.13
Concentric zoning	A2a	5.71	2.39	13.98	48.72	7.04	22.59	0.42		100.85
Concentric zoning	A2a	6.34	2.48	13.54	47.35	7.03	22.24	0.46		99.45
Concentric zoning	A2a	5.62	2.19	12.74	46.32	7.37	21.66	0.54		96.44
Concentric zoning	A2a	6.55	2.64	12.36	44.28	6.81	21.46	0.46		94.55
Concentric zoning	A2a	7.18	2.85	12.11	44.21	7.16	21.51	0.53		95.56
Concentric zoning	A1b	6.85	2.85	13.13	46.78	7.19	22.3	0.45		99.56
Concentric zoning	A1b	6.06	2.54	13.41	47.07	6.98	22.29	0.46		98.8
Concentric zoning	A1b	8.13	3.11	12.59	45.38	7.22	22.35	0.46		99.24
Concentric zoning	A1b	6.5	2.85	13.22	46.85	7.1	22.46	0.48		99.46
Concentric zoning	A1b	7.22	2.96	12.66	45.05	6.91	22.1	0.45		97.35
Concentric zoning	A1b	6.23	2.64	13.07	46.29	7.02	22.04	0.46		97.73
Concentric zoning	A1b	7.51	3.17	12.53	44.92	7.22	21.88	0.5		97.72
Core	A1b	5.07	1.42	14.55	49.01	5.24	22.13	0.45	1.2	99.07
Core	A1b	5.33	1.54	14.77	49.37	5.37	22	0.49	1.24	100.11

Cations

Analysed object	Crystal	Al	Ti	Mg	Si	Fe	Ca	Na	Cr	Total
Mg+Si sector	A1a	0.2	0.06	0.8	1.82	0.22	0.9	0.03		4.03
Mg+Si sector	A1a	0.22	0.05	0.78	1.82	0.24	0.88	0.03		4.03
Mg+Si sector	A1a	0.22	0.06	0.77	1.83	0.22	0.89	0.03		4.02
Mg+Si sector	A2b	0.18	0.05	0.78	1.86	0.24	0.88	0.03		4.02
Mg+Si sector	A2b	0.2	0.06	0.79	1.84	0.23	0.88	0		4.00
Mg+Si sector	A2b	0.19	0.06	0.78	1.85	0.22	0.89	0.03		4.01
Al+Ti sector	A1a	0.35	0.09	0.67	1.72	0.26	0.91	0.04		4.04
Al+Ti sector	A1a	0.35	0.08	0.71	1.72	0.26	0.9	0.04		4.05
Al+Ti sector	A1a	0.33	0.08	0.71	1.74	0.24	0.91	0.04		4.04
Al+Ti sector	A2b	0.3	0.09	0.68	1.77	0.24	0.89	0.04		4.01
Al+Ti sector	A2b	0.31	0.09	0.7	1.74	0.26	0.89	0.04		4.03
Al+Ti sector	A2b	0.33	0.1	0.68	1.73	0.25	0.89	0.05		4.03
Al+Ti sector	A2b	0.34	0.1	0.68	1.74	0.24	0.87	0.04		4.01
Rim	A1a	0.29	0.1	0.67	1.75	0.29	0.89	0.1		4.03
Rim	A1a	0.26	0.1	0.69	1.78	0.25	0.9	0.05		4.02
Rim	A1a	0.13	0.06	0.76	1.89	0.25	0.87	0.04		4.00
Rim	A2b	0.17	0.07	0.77	1.86	0.23	0.87	0.03		4.00
Rim	A2b	0.11	0.06	0.73	1.9	0.27	0.89	0.04		4.01
Rim	A2b	0.27	0.1	0.7	1.77	0.25	0.88	0.04		4.01
Rim	A2b	0.25	0.09	0.69	1.78	0.27	0.89	0.05		4.02
Rim	A2a	0.26	0.11	0.67	1.77	0.28	0.89	0.05		4.02
Rim	A1b	0.25	0.1	0.69	1.78	0.26	0.89	0.04		4.02
Concentric zoning	A2a	0.32	0.08	0.71	1.74	0.25	0.9	0.04		4.04
Concentric zoning	A2a	0.34	0.09	0.7	1.73	0.23	0.91	0.03		4.03
Concentric zoning	A2a	0.26	0.06	0.76	1.8	0.22	0.9	0.04		4.03
Concentric zoning	A2a	0.25	0.07	0.77	1.8	0.22	0.89	0.03		4.03
Concentric zoning	A2a	0.28	0.07	0.76	1.78	0.22	0.89	0.03		4.03
Concentric zoning	A2a	0.26	0.06	0.74	1.8	0.24	0.9	0.04		4.03
Concentric zoning	A2a	0.31	0.08	0.73	1.75	0.23	0.91	0.04		4.03
Concentric zoning	A2a	0.33	0.08	0.71	1.73	0.23	0.9	0.04		4.04
Concentric zoning	A1b	0.3	0.08	0.73	1.76	0.23	0.9	0.03		4.03
Concentric zoning	A1b	0.27	0.07	0.76	1.78	0.22	0.9	0.03		4.03
Concentric zoning	A1b	0.36	0.09	0.71	1.71	0.23	0.9	0.03		4.04
Concentric zoning	A1b	0.29	0.08	0.74	1.76	0.22	0.9	0.03		4.03
Concentric zoning	A1b	0.33	0.09	0.73	1.73	0.22	0.91	0.03		4.04
Concentric zoning	A1b	0.28	0.08	0.74	1.77	0.22	0.9	0.03		4.03
Concentric zoning	A1b	0.34	0.09	0.72	1.72	0.23	0.9	0.04		4.04
Core	A1b	0.22	0.04	0.81	1.83	0.16	0.88	0.03	0.04	4.02
Core	A1b	0.23	0.04	0.81	1.82	0.17	0.87	0.04	0.04	4.02

338.32	2809.686	1492.646	7874.79	312.6525	372.87	2926.948	1364.998	7714.748	319.9992
338.78	2839.107	1418.953	8034.813	368.4888	373.33	2795.825	1360.088	8268.883	315.4473
339.23	2850.412	1487.193	7917.13	332.4551	373.78	2806.432	1312.005	8076.77	304.733
339.69	2873.931	1435.927	7957.598	324.1361	374.24	2931.014	1358.278	8186.034	254.0218
340.14	2764.179	1525.517	7645.012	311.2809	374.69	3037.697	1387.462	8128.885	284.5386
340.60	2700.944	1461.612	7919.362	277.7149	375.15	2959.225	1274.177	8373.928	276.8657
341.05	2867.12	1546.865	7691.916	364.0756	375.60	2834.685	1335.586	8275.01	268.6269
341.51	2715.704	1558.505	7748.496	330.1176	376.05	2901.1	1286.235	8060.041	284.9306
341.96	2707.327	1725.782	7907.772	383.2318	376.51	2981.056	1402.977	7854.187	263.1101
342.42	2630.806	1473.292	7441.117	300.842	376.96	2839.206	1369.493	7938.741	310.2498
342.87	2836.386	1487.659	7640.449	300.3122	377.42	2862.859	1225.907	8031.827	262.1951
343.32	2802.441	1549.135	8109.858	297.9748	377.87	2965.091	1367.688	7853.204	350.6314
343.78	2671.844	1597.216	8207.087	381.1485	378.33	2848.382	1342.417	8142.644	334.3347
344.23	2699.073	1457.396	8302.877	257.1357	378.78	2789.872	1446.68	7952.529	320.8257
344.69	2918	1610.044	7544.732	339.0244	379.24	2907.223	1369.185	7807.452	280.3714
345.14	2736.258	1528.667	8045.747	291.7974	379.69	2944.222	1189.882	7982.168	305.1904
345.60	2642.429	1461.159	7908.115	344.6574	380.15	2822.599	1416.497	8061.633	251.9383
346.05	2898.548	1403.397	8156.996	325.7041	380.60	2761.975	1257.051	8037.463	269.861
346.51	2930.908	1388.385	7656.374	349.9131	381.06	2778.618	1400.214	8116.712	366.9352
346.96	2627.018	1640.381	7926.807	372.1327	381.51	2737.634	1209.393	7794.315	321.2834
347.42	2691.044	1500.593	7989.214	284.4077	381.96	2544.165	1313.426	7914.573	279.1374
347.87	2842.321	1557.043	7918.885	340.7666	382.42	2541.471	1289.041	6916.046	289.5324
348.32	2664.895	1572.789	7829.457	302.7875	382.87	2234.239	1260.319	5994.724	159.2193
348.78	3014.833	1455.856	7770.214	327.069	383.33	2229.874	1563.769	6938.207	237.9718
349.23	2840.752	1585.116	7882.705	294.8679	383.78	2149.674	2013.648	7489.783	183.7618
349.69	2829.661	1386.232	7826.654	289.9245	384.24	1904.952	2429.885	7396.559	208.943
350.14	2940.151	1360.197	7844.653	309.6764	384.69	1551.679	2836.602	7334.371	228.8836
350.60	2776.818	1645.714	7745.921	378.949					
351.05	2831.079	1623.139	7989.534	350.3122					
351.51	2736.261	1455.555	7801.598	242.712					
351.96	2725.8	1761.455	7775.713	287.9719					
352.42	2676.827	1496.988	7906.97	338.4365					
352.87	2907.062	1544.414	7964.556	393.692					
353.33	2760.703	1674.054	7812.904	257.5929					
353.78	2964.327	1535.503	8106.044	296.1019					
354.23	2938.647	1531.202	8114.565	347.1255					
354.69	2969.976	1557.198	7981.178	297.59					
355.14	2854.277	1579.974	8030.315	300.4431					
355.60	2654.008	1436.118	7914.325	314.5979					
356.05	2800.088	1586.307	7933.102	364.5325					
356.51	2668.733	1585.12	7734.403	356.6057					
356.96	2855.852	1456.011	7703.354	322.9749					
357.42	2756.61	1398.098	7864.882	308.3699					
357.87	2943.568	1556.971	8134.283	369.7299					
358.33	2915.851	1587.309	8198.558	328.2881					
358.78	2784.376	1383.618	7769.122	306.5403					
359.23	2927.084	1404.556	7863.452	367.85					
359.69	2864.173	1484.162	8159.989	311.8032					
360.14	2920.391	1445.105	8023.067	357.7744					
360.60	2956.052	1476.591	7826.691	336.23					
361.05	2666.5	1578.168	7835.588	392.182					
361.51	3034.495	1526.825	7919.758	320.1873					
361.96	2772.074	1439.194	7922.331	355.9671					
362.42	2807.033	1350.634	8117.144	296.7408					
362.87	2898.299	1417.724	7922.598	302.8529					
363.33	2998.867	1382.588	7909.209	354.4064					
363.78	2769.97	1413.496	8027.034	334.4731					
364.24	2998.177	1364.922	7919.887	386.9412					
364.69	2884.308	1529.281	8053.904	308.3698					
365.14	2808.084	1488.577	7738.623	343.1694					
365.60	2785.343	1394.106	7974.344	313.1099					
366.05	2829.211	1482.622	7900.855	300.2396					
366.51	2784.027	1350.632	7979.165	353.4917					
366.96	3072.044	1352.904	8094.796	267.0733					
367.42	2912.24	1375.443	7923.319	321.8134					
367.87	2925.455	1329.323	7999.276	297.9749					
368.33	2769.222	1325.598	8161.639	305.5097					
368.78	2900.643	1370.144	8186.473	303.8837					
369.24	2815.579	1254.517	8025.763	313.5019					
369.69	2937.829	1367.649	7992.673	282.3168					
370.15	3012.89	1313.234	8125.475	363.0445					
370.60	2950.71	1575.597	8155	279.733					
371.05	3043.045	1337.501	8140.527	306.2864					
371.51	2938.285	1301.364	8199.829	329.5222					
371.96	2882.849	1255.82	8044.139	287.5144					
372.42	2735.473	1340.154	8151.583	293.5612					

407.08	2596.75	1115.038	7380.328	294.2625
407.98	2587.171	1146.807	7317.918	284.4187
408.88	2582.268	1082.216	7477.83	290.8419
409.77	2630.384	1155.631	7439.865	245.1935
410.67	2430.052	1146.623	7181.276	260.0289
411.56	2537.366	1180.476	7341.797	294.5177
412.46	2573.559	1216.355	7297.218	250.5454
413.35	2594.135	1182.736	7175.254	285.9598
414.25	2576.46	1224.751	7254.054	303.4016
415.15	2556.945	1184.093	7277.377	280.8727
416.04	2613.259	1264.915	7226.511	298.0093
416.94	2555.62	1266.812	7122.939	304.4921
417.83	2569.007	1235.195	7210.379	270.8633
418.73	2563.203	1286.671	6957.498	289.2106
419.63	2517.181	1300.098	7111.066	286.5498
420.52	2645.177	1258.326	7157.115	298.2443
421.42	2463.902	1328.063	7004.522	230.9778
422.31	2486.162	1329.998	7046.607	312.1703
423.21	2424.803	1458.281	6847.057	303.0062
424.10	2380.492	1464.881	6692.908	338.6406
425.00	2324.382	1512.351	6744.062	320.5037
425.90	2271.71	1588.059	6807.968	340.4114
426.79	2328.698	1652.672	6922.909	379.6719
427.69	2296.81	1585.715	6761.474	372.3842
428.58	2293.63	1569.898	6744.555	369.7534
429.48	2301.288	1541.11	6932.762	318.5025
430.38	2303.413	1522.691	6736.297	370.2383
431.27	2361.415	1514.446	6752.585	302.8062
432.17	2334.585	1472.604	6739.182	362.0198
433.06	2346.977	1573.252	6860.217	342.3672
433.96	2406.452	1477.925	6839.364	304.3116
434.85	2323.977	1443.292	6910.216	276.0458
435.75	2402.668	1414.87	6920.537	337.5703
436.65	2340.326	1483.702	6948.917	306.9631
437.54	2385.065	1504.134	7025.596	322.344
438.44	2488.98	1519.841	6877.265	347.1641
439.33	2381.886	1426.147	6910.559	319.0725
440.23	2472.825	1562.507	6944.938	303.0613
441.12	2438.993	1452.648	6800.741	319.1178
442.02	2291.079	1463.521	6928.852	298.1241
442.92	2350.484	1480.045	6985.177	322.4089
443.81	2460.837	1418.989	6864.79	277.026
444.71	2303.26	1399.248	6894.984	294.5782
445.60	2359.614	1469.071	6904.264	347.3492
446.50	2426.469	1471.396	6814.43	344.3536
447.40	2434.422	1391.708	7072.809	319.0679
448.29	2415.809	1391.469	6949.863	278.7872
449.19	2429.406	1367.715	6952.019	313.1155

13.28	3009.181	821.4877	8327.479	260.4961	14.98	2743.385	886.9989	8341.291	288.881
13.31	2737.517	806.8242	8255.038	257.3313	15.01	2758.676	708.5551	8775.564	286.5558
13.33	3034.415	718.1008	8929.422	250.8499	15.03	2673.381	859.7057	8377.11	270.3612
13.35	2884.449	860.6506	8336.603	259.1832					
13.37	2797.378	772.824	8422.605	278.6467					
13.40	2812.025	806.5465	8598.703	242.6783					
13.42	2719.226	897.931	8538.074	265.1922					
13.44	3006.734	789.8843	8579.299	288.2928					
13.46	2822.524	717.9899	8567.949	212.4527					
13.49	2917.825	849.1531	8719.912	243.9912					
13.51	2934.163	743.0477	8387.725	280.9614					
13.53	2892.664	910.9336	8375.396	273.8932					
13.55	2702.7	909.2076	8503.253	254.1193					
13.57	2871.391	820.0467	8422.319	322.0511					
13.60	2843.028	882.0448	8499.725	260.5532					
13.62	2942.849	837.9954	8662.32	243.4614					
13.64	2831.503	966.2109	8285.644	297.5808					
13.66	2983.638	879.3757	8513.961	310.1281					
13.69	2996.746	787.494	8422.09	228.532					
13.71	2994.479	849.6636	8345.065	285.0233					
13.73	2824.475	874.9363	8672.944	282.9186					
13.75	2786.34	832.8779	8468.363	297.5233					
13.78	2694.307	825.2186	8575.609	211.9229					
13.80	2907.992	723.7696	8267.894	285.0233					
13.82	3061.707	833.9972	8470.213	250.2155					
13.84	3060.076	796.7177	8326.054	272.5233					
13.87	2676.022	903.3285	8534.799	226.6322					
13.89	2758.811	863.4272	8145.567	315.5596					
13.91	3059.904	821.3777	8487.936	230.7989					
13.93	2792.437	788.3746	8324.967	202.797					
13.95	2756.033	792.2209	7857.917	283.344					
13.98	2975.95	691.7716	8338.673	243.7238					
14.00	2793.59	827.6544	8500.677	273.5834					
14.02	2896.589	764.657	8420.718	297.4652					
14.04	2777.67	736.5477	8628.17	282.389					
14.07	2919.821	800.8223	8821.331	312.453					
14.09	2755.736	792.9957	8752.199	287.8203					
14.11	2915.764	770.3253	8297.941	229.6495					
14.13	2746.54	822.0999	8871.533	304.7967					
14.16	2715.278	851.4913	8167.953	304.9592					
14.18	2661.196	842.6558	8412.938	277.2199					
14.20	2892.47	847.9373	8738.461	263.8225					
14.22	2945.599	779.7687	8494.271	267.4592					
14.25	2732.078	916.0967	8368.011	280.017					
14.27	2841.628	805.4336	8265.193	235.6581					
14.29	2838.475	749.4348	8511.059	269.7262					
14.31	2695.25	724.1523	8527.993	262.2901					
14.34	2844.13	863.8253	8417.583	242.9312					
14.36	2873.076	762.0402	8561.975	278.8986					
14.38	2855.496	814.9347	8485.009	208.8167					
14.40	2899.244	715.2069	8561.506	291.9288					
14.42	2774.624	776.1522	8382.102	372.9952					
14.45	2753.5	828.7172	8463.146	187.5581					
14.47	3003.68	802.4347	8289.878	278.2805					
14.49	2600.929	850.4818	8420.864	256.0196					
14.51	3009.027	893.5363	8288.881	254.0617					
14.54	2869.985	714.7721	8539.027	279.1197					
14.56	2982.824	755.0464	8306.984	260.0233					
14.58	2835.236	735.6628	8475.614	222.686					
14.60	2883.93	780.8213	8402.666	287.0857					
14.63	2772.479	827.1045	8908.304	231.9168					
14.65	2887.123	707.3708	8415.492	296.6837					
14.67	2935.601	841.2692	8577.172	249.953					
14.69	2833.674	827.8268	8290.228	252.22					
14.72	2852.034	858.3807	8562.878	263.9384					
14.74	2646.223	847.6553	8394.863	252.6343					
14.76	2832.928	781.931	8608.892	285.9207					
14.78	2676.854	720.9957	8321.709	355.4892					
14.80	2676.439	819.3785	8411.384	282.0635					
14.83	2792.899	826.9962	8328.141	274.3179					
14.85	2794.276	888.1548	8244.428	331.7538					
14.87	2808.47	910.8322	8314.085	256.8588					
14.89	2773.795	820.436	8308.221	191.6666					
14.92	2740.183	750.8281	8348.477	268.3564					
14.94	2888.56	854.7694	8411.096	304.6502					
14.96	2810.943	817.5468	8631.082	272.9952					

17.35	1966.915	1384.719	7734.323	295.781
17.38	1997.425	1594.216	7807.138	320.7192
17.41	1911.728	1522.986	7837.108	227.2683
17.44	1921.194	1503.354	7800.885	283.106

Appendix F – LA-ICP-MS spot data

Data acquired from the LA-ICP-MS spot analyses are presented in tables 1-3, including error margins and limit of detection (LOD) for each element.

Table 1: A1a-spot-1 – 4 and A2a-spot-1 – 4

Element	A1a-spot-1	A1a-spot-2	A1a-spot-3	A1a-spot-4	A2a-spot-1	A2a-spot-2	A2a-spot-3	A2a-spot-4
Na_ppm_m23	Below LOD	Below LOD	5.20E+03	Below LOD	3.60E+03	3.00E+03	3.30E+03	4.20E+03
Na_ppm_m23_Int2SE	Below LOD	Below LOD	1.80E+03	Below LOD	1.40E+03	1.50E+03	1.70E+03	1.70E+03
Na_ppm_m23_LOD	3100	3900	3100	2900	2900	2500	2600	2700
Si_ppm_m29	2.40E+05	2.06E+05	2.20E+05	2.21E+05	2.12E+05	2.17E+05	2.19E+05	2.15E+05
Si_ppm_m29_Int2SE	1.00E+04	6.60E+03	1.00E+04	9.10E+03	8.40E+03	8.10E+03	7.70E+03	7.70E+03
Si_ppm_m29_LOD	2200	2300	2000	2300	2000	1900	2100	2100
Sc_ppm_m45	98.6	110.9	95.6	106	50.6	75.2	73.3	64.7
Sc_ppm_m45_Int2SE	3	3.7	3.7	3.5	1.6	2.4	2.4	1.8
Sc_ppm_m45_LOD	0.5	0.58	0.54	0.48	0.56	0.64	0.61	0.6
Ti_ppm_m49	10240	14280	12850	13350	15470	13190	12950	15810
Ti_ppm_m49_Int2SE	390	460	560	500	460	510	480	500
Ti_ppm_m49_LOD	2	2.7	2.5	2.3	2.1	2.1	2.2	2.2
V_ppm_m51	287	390	336	332	276	269	272	303
V_ppm_m51_Int2SE	14	15	17	15	10	10	12	12
V_ppm_m51_LOD	0.22	0.27	0.24	0.23	0.22	0.21	0.22	0.23
Cr_ppm_m52	37.2	51.6	303	364	9.5	65.3	5.32	7.3
Cr_ppm_m52_Int2SE	1.6	2.2	19	16	1.2	2.6	0.94	1
Cr_ppm_m52_LOD	2.4	2.6	2.7	2.2	2	2	2.2	2.1
Co_ppm_m59	42	39.4	36.5	36.8	32.6	34.4	33.7	31.5
Co_ppm_m59_Int2SE	1.7	1.5	2.2	1.7	1.4	1.3	1.4	1.3
Co_ppm_m59_LOD	1.6	1.9	1.6	1.6	1.6	1.5	1.7	1.7
Ni_ppm_m60	126	121.8	150	155.9	51.6	84	42.9	42.5
Ni_ppm_m60_Int2SE	9.4	8.6	11	8.8	6	6.7	6.9	6.5
Ni_ppm_m60_LOD	14	14	13	13	12	12	14	13
Sr_ppm_m88	74.5	87.7	80.2	79.1	97.2	86.8	87.2	99.5
Sr_ppm_m88_Int2SE	2.7	3.3	3.1	3	3.1	3.1	3.1	3.2
Sr_ppm_m88_LOD	0.38	0.37	0.4	0.4	0.55	0.45	0.45	0.53
Y_ppm_m89	17.55	27.3	13.51	13.81	18.07	15.74	17.61	19.79
Y_ppm_m89_Int2SE	0.57	1.1	0.44	0.53	0.59	0.62	0.57	0.72
Y_ppm_m89_LOD	0.049	0.058	0.045	0.05	0.037	0.04	0.043	0.043
Zr_ppm_m90	109.9	167.5	81.5	87.1	125.3	95	113.4	137.2
Zr_ppm_m90_Int2SE	3.4	5.9	2.9	3	4	3.4	3.6	4.5
Zr_ppm_m90_LOD	0.077	0.075	0.076	0.077	0.088	0.094	0.092	0.1
Nb_ppm_m93	0.54	1.126	0.608	0.61	0.977	0.642	1.37	1.07
Nb_ppm_m93_Int2SE	0.043	0.07	0.051	0.047	0.056	0.06	0.37	0.055
Nb_ppm_m93_LOD	0.027	0.031	0.026	0.026	0.023	0.024	0.023	0.024
Ba_ppm_m137	Below LOD	Below LOD	Below LOD	Below LOD	Below LOD	Below LOD	Below LOD	Below LOD
Ba_ppm_m137_Int2SE	Below LOD	Below LOD	Below LOD	Below LOD	Below LOD	Below LOD	Below LOD	Below LOD
Ba_ppm_m137_LOD	0.88	0.93	0.76	0.84	0.7	0.84	0.67	0.79
La_ppm_m139	5.12	9.12	3.98	3.91	5.82	4.72	5.58	6.27
La_ppm_m139_Int2SE	0.28	0.42	0.23	0.19	0.29	0.23	0.3	0.26
La_ppm_m139_LOD	0.064	0.064	0.054	0.06	0.053	0.054	0.058	0.051

Ce_ppm_m140	19.4	30.7	15.33	15.13	22.79	18.14	20.17	24.42
Ce_ppm_m140_Int2SE	1.1	1.3	0.83	0.64	0.93	0.69	0.92	0.99
Ce_ppm_m140_LOD	0.042	0.046	0.039	0.037	0.047	0.04	0.041	0.049
Pr_ppm_m141	3.4	5.46	2.75	2.59	4.18	3.38	3.59	4.23
Pr_ppm_m141_Int2SE	0.15	0.18	0.18	0.12	0.19	0.15	0.16	0.2
Pr_ppm_m141_LOD	0.041	0.037	0.032	0.032	0.042	0.04	0.041	0.045
Nd_ppm_m146	18.31	28.7	14.21	13.86	21.09	17.51	19.76	22.83
Nd_ppm_m146_Int2SE	0.81	1.1	0.82	0.54	0.89	0.72	0.83	0.88
Nd_ppm_m146_LOD	0.18	0.24	0.17	0.17	0.19	0.15	0.15	0.16
Sm_ppm_m147	5.23	8.42	4.26	4.3	6.26	5	5.63	6.84
Sm_ppm_m147_Int2SE	0.35	0.57	0.34	0.35	0.45	0.36	0.35	0.46
Sm_ppm_m147_LOD	0.24	0.24	0.23	0.29	0.2	0.21	0.22	0.25
Eu_ppm_m153	1.71	2.72	1.47	1.53	2	1.8	1.97	2.28
Eu_ppm_m153_Int2SE	0.14	0.15	0.11	0.12	0.14	0.13	0.14	0.14
Eu_ppm_m153_LOD	0.085	0.095	0.076	0.082	0.069	0.069	0.073	0.081
Gd_ppm_m157	5.68	9.28	4.5	4.54	6.08	4.88	5.48	6.44
Gd_ppm_m157_Int2SE	0.51	0.56	0.44	0.4	0.5	0.4	0.46	0.43
Gd_ppm_m157_LOD	0.41	0.41	0.4	0.36	0.37	0.33	0.36	0.39
Dy_ppm_m163	4.21	6.87	3.36	3.3	4.42	3.77	4.1	4.88
Dy_ppm_m163_Int2SE	0.27	0.42	0.27	0.24	0.29	0.26	0.27	0.32
Dy_ppm_m163_LOD	0.15	0.14	0.14	0.17	0.32	0.11	0.14	0.13
Er_ppm_m166	1.74	2.83	1.35	1.54	1.74	1.6	1.76	1.87
Er_ppm_m166_Int2SE	0.14	0.19	0.15	0.14	0.16	0.16	0.15	0.16
Er_ppm_m166_LOD	0.11	0.13	0.093	0.1	0.1	0.1	0.093	0.1
Yb_ppm_m172	1.18	1.56	0.88	0.98	1.05	1.01	1.14	1.15
Yb_ppm_m172_Int2SE	0.2	0.22	0.15	0.15	0.15	0.14	0.15	0.15
Yb_ppm_m172_LOD	0.19	0.19	0.19	0.17	0.17	0.15	0.16	0.15
Hf_ppm_m178	4.97	6.91	4.07	3.98	5	4.12	4.83	5.95
Hf_ppm_m178_Int2SE	0.34	0.42	0.35	0.28	0.3	0.3	0.34	0.41
Hf_ppm_m178_LOD	0.15	0.12	0.12	0.13	0.18	0.2	0.18	0.17

Table 2: A1b-spot-1 – 6

Element	A1b-spot-1	A1b-spot-2	A1b-spot-3	A1b-spot-4	A1b-spot-5	A1b-spot-6
Na_ppm_m23	Below LOD	Below LOD	3.50E+03	4.80E+03	4.00E+03	3.80E+03
Na_ppm_m23_Int2SE	Below LOD	Below LOD	1.60E+03	1.40E+03	1.50E+03	1.50E+03
Na_ppm_m23_LOD	3400	2800	3400	2900	2900	3300
Si_ppm_m29	2.36E+05	2.11E+05	2.17E+05	2.25E+05	2.29E+05	2.24E+05
Si_ppm_m29_Int2SE	7.80E+03	8.20E+03	6.50E+03	7.70E+03	9.70E+03	8.50E+03
Si_ppm_m29_LOD	2200	2200	2500	2200	2000	2000
Sc_ppm_m45	81.6	84.9	100.4	88.4	88.4	95.6
Sc_ppm_m45_Int2SE	2.4	2.4	2.8	2.5	2.5	3.2
Sc_ppm_m45_LOD	0.58	0.72	0.72	0.59	0.62	0.61
Ti_ppm_m49	7620	16300	15530	14480	14090	16740
Ti_ppm_m49_Int2SE	280	520	480	470	440	530
Ti_ppm_m49_LOD	3.4	2.2	2.2	2.5	2.1	2.3
V_ppm_m51	245.4	349	352	323	328	357
V_ppm_m51_Int2SE	9.1	13	13	10	12	13
V_ppm_m51_LOD	0.24	0.22	0.28	0.22	0.22	0.23
Cr_ppm_m52	5390	301	123.8	226.1	170.1	165.4
Cr_ppm_m52_Int2SE	170	10	4.2	8.9	6.5	6.5
Cr_ppm_m52_LOD	1.9	2.2	2.1	1.9	2.3	2.6
Co_ppm_m59	35.8	34.6	37.2	35.9	37.6	38.2
Co_ppm_m59_Int2SE	1.5	1.7	1.6	1.4	1.5	1.7
Co_ppm_m59_LOD	1.7	1.6	1.8	1.5	1.5	1.8
Ni_ppm_m60	240.3	139.9	135.3	123.3	107.8	105.1
Ni_ppm_m60_Int2SE	9.8	8.4	8.3	7.8	7.2	8.1
Ni_ppm_m60_LOD	14	14	13	13	13	14
Sr_ppm_m88	74.8	94.4	85.3	87.8	84.1	92.7
Sr_ppm_m88_Int2SE	2.6	3.1	2.7	2.6	2.7	3
Sr_ppm_m88_LOD	0.55	0.6	0.59	0.51	0.52	0.46
Y_ppm_m89	7.96	15.53	15.67	15.44	15.12	19.19
Y_ppm_m89_Int2SE	0.31	0.57	0.41	0.47	0.54	0.57
Y_ppm_m89_LOD	0.041	0.044	0.048	0.048	0.046	0.049
Zr_ppm_m90	33.8	100.6	108.4	103.2	92.7	129.5
Zr_ppm_m90_Int2SE	1	3.1	2.6	2.9	2.7	4
Zr_ppm_m90_LOD	0.11	0.13	0.11	0.094	0.11	0.11
Nb_ppm_m93	0.282	0.779	0.723	0.739	0.726	1.071
Nb_ppm_m93_Int2SE	0.031	0.051	0.05	0.048	0.049	0.06
Nb_ppm_m93_LOD	0.027	0.029	0.024	0.024	0.02	0.025
Ba_ppm_m137	Below LOD	Below LOD	Below LOD	Below LOD	Below LOD	Below LOD
Ba_ppm_m137_Int2SE	Below LOD	Below LOD	Below LOD	Below LOD	Below LOD	Below LOD
Ba_ppm_m137_LOD	0.78	0.86	0.83	0.8	0.8	0.91
La_ppm_m139	2.12	4.62	4.53	4.51	4.76	6.2
La_ppm_m139_Int2SE	0.11	0.24	0.2	0.19	0.22	0.29
La_ppm_m139_LOD	0.061	0.056	0.057	0.057	0.061	0.062
Ce_ppm_m140	8.49	18.06	16.92	17.97	17.87	22.35
Ce_ppm_m140_Int2SE	0.33	0.68	0.53	0.68	0.69	0.92
Ce_ppm_m140_LOD	0.049	0.052	0.046	0.042	0.04	0.052

Pr_ppm_m141	1.566	3.13	3.02	3.24	3.11	4.18
Pr_ppm_m141_Int2SE	0.083	0.13	0.12	0.12	0.13	0.16
Pr_ppm_m141_LOD	0.045	0.058	0.048	0.04	0.035	0.043
Nd_ppm_m146	7.87	16.56	16.16	16.84	16.31	21.19
Nd_ppm_m146_Int2SE	0.43	0.65	0.64	0.64	0.8	0.84
Nd_ppm_m146_LOD	0.17	0.2	0.16	0.19	0.17	0.15
Sm_ppm_m147	2.4	5.08	5.08	5.18	4.79	6.13
Sm_ppm_m147_Int2SE	0.26	0.37	0.36	0.33	0.36	0.4
Sm_ppm_m147_LOD	0.24	0.21	0.21	0.21	0.27	0.25
Eu_ppm_m153	0.905	1.86	1.72	1.78	1.67	2
Eu_ppm_m153_Int2SE	0.077	0.15	0.11	0.13	0.12	0.13
Eu_ppm_m153_LOD	0.077	0.079	0.085	0.08	0.076	0.085
Gd_ppm_m157	2.56	4.84	4.99	4.46	4.92	5.93
Gd_ppm_m157_Int2SE	0.33	0.42	0.37	0.34	0.44	0.46
Gd_ppm_m157_LOD	0.36	0.39	0.43	0.41	0.37	0.42
Dy_ppm_m163	1.88	3.53	4.03	3.84	3.65	4.91
Dy_ppm_m163_Int2SE	0.18	0.25	0.3	0.25	0.25	0.32
Dy_ppm_m163_LOD	0.12	0.16	0.14	0.11	0.15	0.14
Er_ppm_m166	0.69	1.31	1.48	1.57	1.5	1.8
Er_ppm_m166_Int2SE	0.1	0.14	0.13	0.16	0.13	0.15
Er_ppm_m166_LOD	0.11	0.12	0.12	0.11	0.11	0.12
Yb_ppm_m172	0.43	0.89	0.95	0.98	0.99	1.23
Yb_ppm_m172_Int2SE	0.11	0.14	0.16	0.12	0.16	0.19
Yb_ppm_m172_LOD	0.2	0.27	0.18	0.19	0.17	0.18
Hf_ppm_m178	1.78	4.75	5.2	4.33	3.84	5.97
Hf_ppm_m178_Int2SE	0.19	0.3	0.36	0.26	0.26	0.39
Hf_ppm_m178_LOD	0.15	0.2	0.18	0.17	0.14	0.14

Table 3: A2b-spot-1 – 5

Element	A2b-spot-1	A2b-spot-2	A2b-spot-3	A2b-spot-4	A2b-spot-5
Na_ppm_m23	3.70E+03	4.60E+03	Below LOD	4.60E+03	4.50E+03
Na_ppm_m23_Int2SE	1.30E+03	1.50E+03	Below LOD	1.50E+03	1.40E+03
Na_ppm_m23_LOD	2900	2900	3000	2900	2700
Si_ppm_m29	2.37E+05	2.16E+05	2.16E+05	2.18E+05	2.33E+05
Si_ppm_m29_Int2SE	9.00E+03	7.30E+03	7.90E+03	7.20E+03	8.50E+03
Si_ppm_m29_LOD	2100	2100	2100	2000	1900
Sc_ppm_m45	57.1	68.7	65	60.7	50.6
Sc_ppm_m45_Int2SE	1.9	1.9	2.2	2	1.6
Sc_ppm_m45_LOD	0.46	0.4	0.55	0.64	0.59
Ti_ppm_m49	9900	18240	18870	17060	11150
Ti_ppm_m49_Int2SE	320	580	730	600	370
Ti_ppm_m49_LOD	2	2.2	2.2	2	2.1
V_ppm_m51	325	453	438	457	326
V_ppm_m51_Int2SE	12	16	19	18	11
V_ppm_m51_LOD	0.22	0.24	0.2	0.22	0.2
Cr_ppm_m52	Below LOD	Below LOD	Below LOD	Below LOD	Below LOD
Cr_ppm_m52_Int2SE	Below LOD	Below LOD	Below LOD	Below LOD	Below LOD
Cr_ppm_m52_LOD	1.9	2	1.8	2.1	1.9
Co_ppm_m59	35.4	32.9	34.7	33.6	34.5
Co_ppm_m59_Int2SE	1.6	1.5	1.6	1.3	1.2
Co_ppm_m59_LOD	1.6	1.5	1.6	1.3	1.3
Ni_ppm_m60	Below LOD	Below LOD	Below LOD	Below LOD	Below LOD
Ni_ppm_m60_Int2SE	Below LOD	Below LOD	Below LOD	Below LOD	Below LOD
Ni_ppm_m60_LOD	11	13	13	13	12
Sr_ppm_m88	95.8	108.7	107.3	115.9	91.8
Sr_ppm_m88_Int2SE	3.1	3.4	3.6	4.1	3.2
Sr_ppm_m88_LOD	0.35	0.4	0.42	0.51	0.47
Y_ppm_m89	20.09	29.49	27.4	36.2	22.6
Y_ppm_m89_Int2SE	0.7	0.97	1	1.1	0.8
Y_ppm_m89_LOD	0.046	0.049	0.041	0.041	0.046
Zr_ppm_m90	108.3	222.2	185.4	222	121.2
Zr_ppm_m90_Int2SE	3.6	6.5	6.9	7.1	3.5
Zr_ppm_m90_LOD	0.07	0.06	0.082	0.084	0.092
Nb_ppm_m93	0.69	1.9	1.614	1.627	0.666
Nb_ppm_m93_Int2SE	0.047	0.086	0.088	0.076	0.038
Nb_ppm_m93_LOD	0.023	0.024	0.024	0.023	0.021
Ba_ppm_m137	Below LOD	Below LOD	Below LOD	Below LOD	Below LOD
Ba_ppm_m137_Int2SE	Below LOD	Below LOD	Below LOD	Below LOD	Below LOD
Ba_ppm_m137_LOD	0.88	0.79	0.86	0.71	0.72
La_ppm_m139	6.34	10.55	10.01	13.05	6.81
La_ppm_m139_Int2SE	0.3	0.44	0.48	0.56	0.27
La_ppm_m139_LOD	0.053	0.061	0.058	0.051	0.054
Ce_ppm_m140	24.5	37.8	37.4	46.8	25.23
Ce_ppm_m140_Int2SE	1.1	1.3	1.5	1.7	0.93
Ce_ppm_m140_LOD	0.034	0.034	0.037	0.047	0.048

Pr_ppm_m141	4.16	6.72	6.39	8.07	4.71
Pr_ppm_m141_Int2SE	0.18	0.26	0.29	0.33	0.22
Pr_ppm_m141_LOD	0.03	0.031	0.04	0.036	0.037
Nd_ppm_m146	22.46	34.1	32.6	42	25.1
Nd_ppm_m146_Int2SE	0.82	1.2	1.3	1.4	1
Nd_ppm_m146_LOD	0.19	0.2	0.16	0.18	0.16
Sm_ppm_m147	6.94	9.9	9	12.16	7.17
Sm_ppm_m147_Int2SE	0.44	0.38	0.45	0.59	0.43
Sm_ppm_m147_LOD	0.2	0.22	0.19	0.19	0.22
Eu_ppm_m153	2.04	3.04	3.04	3.77	2.26
Eu_ppm_m153_Int2SE	0.12	0.15	0.17	0.2	0.13
Eu_ppm_m153_LOD	0.076	0.08	0.077	0.083	0.062
Gd_ppm_m157	6.52	9.36	9.19	11.89	7.41
Gd_ppm_m157_Int2SE	0.47	0.56	0.57	0.63	0.51
Gd_ppm_m157_LOD	0.34	0.33	0.33	0.39	0.36
Dy_ppm_m163	4.98	7.46	6.49	8.7	5.42
Dy_ppm_m163_Int2SE	0.32	0.41	0.44	0.45	0.36
Dy_ppm_m163_LOD	0.11	0.13	0.13	0.15	0.097
Er_ppm_m166	2.03	2.74	2.55	3.67	2.18
Er_ppm_m166_Int2SE	0.17	0.2	0.2	0.26	0.16
Er_ppm_m166_LOD	0.11	0.1	0.11	0.11	0.092
Yb_ppm_m172	1.16	1.97	1.62	2.35	1.31
Yb_ppm_m172_Int2SE	0.15	0.19	0.16	0.22	0.17
Yb_ppm_m172_LOD	0.16	0.19	0.16	0.16	0.17
Hf_ppm_m178	4.75	9.32	7.7	8.78	4.91
Hf_ppm_m178_Int2SE	0.3	0.47	0.46	0.5	0.27
Hf_ppm_m178_LOD	0.12	0.12	0.13	0.17	0.16

**Tidigare skrifter i serien
”Examensarbeten i Geologi vid Lunds
universitet”:**

541. Staahlnacke, Simon, 2018: En sammanställning av norra Skånes prekambrika berggrund. (15 hp)
542. Martell, Josefin, 2018: Shock metamorphic features in zircon grains from the Mien impact structure - clues to conditions during impact. (45 hp)
543. Chitindingu, Tawonga, 2018: Petrological characterization of the Cambrian sandstone reservoirs in the Baltic Basin, Sweden. (45 hp)
544. Chonewicz, Julia, 2018: Dimensionerande vattenförbrukning och alternativa vattenkvaliteter. (15 hp)
545. Adeen, Lina, 2018: Hur lämpliga är de geofysiska metoderna resistivitet och IP för kartläggning av PFOS? (15 hp)
546. Nilsson Brunlid, Anette, 2018: Impact of southern Baltic sea-level changes on landscape development in the Verkeån River valley at Haväng, southern Sweden, during the early and mid Holocene. (45 hp)
547. Perälä, Jesper, 2018: Dynamic Recrystallization in the Sveconorwegian Frontal Wedge, Småland, southern Sweden. (45 hp)
548. Artursson, Christopher, 2018: Stratigraphy, sedimentology and geophysical assessment of the early Silurian Halla and Klinteberg formations, Altajme core, Gotland, Sweden. (45 hp)
549. Kempengren, Henrik, 2018: Att välja den mest hållbara efterbehandlingsmetoden vid sanering: Applicering av beslutsstödsverktyget SAMLA. (45 hp)
550. Andreasson, Dagnija, 2018: Assessment of using liquidity index for the approximation of undrained shear strength of clay tills in Scania. (45 hp)
551. Ahrenstedt, Viktor, 2018: The Neoproterozoic Visingsö Group of southern Sweden: Lithology, sequence stratigraphy and provenance of the Middle Formation. (45 hp)
552. Berglund, Marie, 2018: Basaltkuppen - ett spel om mineralogi och petrologi. (15 hp)
553. Hernäs, Tove, 2018: Garnet amphibolite in the internal Eastern Segment, Sveconorwegian Province: monitors of metamorphic recrystallization at high temperature and pressure during Sveconorwegian orogeny. (45 hp)
554. Halling, Jenny, 2019: Characterization of black rust in reinforced concrete structures: analyses of field samples from southern Sweden. (45 hp)
555. Stevic, Marijana, 2019: Stratigraphy and dating of a lake sediment record from Lyngsjön, eastern Scania - human impact and aeolian sand deposition during the last millennium. (45 hp)
556. Rabanser, Monika, 2019: Processes of Lateral Moraine Formation at a Debris-covered Glacier, Suldenferner (Vedretta di Solda), Italy. (45 hp)
557. Nilsson, Hanna, 2019: Records of environmental change and sedimentation processes over the last century in a Baltic coastal inlet. (45 hp)
558. Ingered, Mimmi, 2019: Zircon U-Pb constraints on the timing of Sveconorwegian migmatite formation in the Western and Median Segments of the Idefjorden terrane, SW Sweden. (45 hp)
559. Hjorth, Ingeborg, 2019: Paleomagnetisk undersökning av vulkanen Rangitoto, Nya Zeeland, för att bestämma dess utbrotthistoria. (15 hp)
560. Westberg, Märta, 2019: Enigmatic worm-like fossils from the Silurian Waukesha Lagerstätte, Wisconsin, USA. (15 hp)
561. Björn, Julia, 2019: Undersökning av påverkan på hydraulisk konduktivitet i förorenat område efter in situ-saneringsförsök. (15 hp)
562. Faraj, Haider, 2019: Tolkning av georadarprofiler över grundvattenmagasinet Verveln - Gullringen i Kalmar län. (15 hp)
563. Bjeremo, Tim, 2019: Eoliska avlagringar och vindriktningar under holocen i och kring Store Mosse, södra Sverige. (15 hp)
564. Langkjaer, Henrik, 2019: Analys av Östergötlands kommande grundvattenresurser ur ett klimtperspektiv - med fokus på förstärkt grundvattenbildning. (15 hp)
565. Johansson, Marcus, 2019: Hur öppet var landskapet i södra Sverige under Atlantisk tid? (15 hp)
566. Molin, Emmy, 2019: Litologi, sedimentologi och kolisotopstratigrafi över krita-paleogen-gränsintervallet i bormningen Limhamn-2018. (15 hp)
567. Schroeder, Mimmi, 2019: The history of European hemp cultivation. (15 hp)
568. Damber, Maja, 2019: Granens invandring i sydvästa Sverige, belyst genom polle-nanalys från Skottenesjön. (15 hp)
569. Lundgren Sassner, Lykke, 2019: Strandmorfologi, stranderosion och stranddeposition, med en fallstudie på Tylösand sandstrand, Halland. (15 hp)
570. Greiff, Johannes, 2019: Mesozoiska konglomerat och Skånes tektoniska utveckling. (15 hp)
571. Persson, Eric, 2019: An Enigmatic Cerapodian Dentary from the Cretaceous of southern Sweden. (15 hp)
572. Aldenius, Erik, 2019: Subsurface charac-

- terization of the Lund Sandstone – 3D model of the sandstone reservoir and evaluation of the geoenery storage potential, SW Skåne, South Sweden. (45 hp)
573. Juliusson, Oscar, 2019: Impacts of subglacial processes on underlying bedrock. (15 hp)
574. Sartell, Anna, 2019: Metamorphic paragenesis and P-T conditions in garnet amphibolite from the Median Segment of the Idefjorden Terrane, Lilla Edet. (15 hp)
575. Végvári, Fanni, 2019: Vulkanisk inverkan på klimatet och atmorsfärcirkulationen: En litteraturstudie som jämför vulkanism på låg respektive hög latitud. (15 hp)
576. Gustafsson, Jon, 2019: Petrology of platinum-group element mineralization in the Koillismaa intrusion, Finland. (45 hp)
577. Wahlquist, Per, 2019: Undersökning av mindre förkastningar för vattenuttag i sedimentärt berg kring Kingelstad och Tjutebro. (15 hp)
578. Gaitan Valencia, Camilo Esteban, 2019: Unravelling the timing and distribution of Paleoproterozoic dyke swarms in the eastern Kaapvaal Craton, South Africa. (45 hp)
579. Eggert, David, 2019: Using Very-Low-Frequency Electromagnetics (VLF-EM) for geophysical exploration at the Albertine Graben, Uganda - A new CAD approach for 3D data blending. (45 hp)
580. Plan, Anders, 2020: Resolving temporal links between the Högberget granite and the Wigström tungsten skarn deposit in Bergslagen (Sweden) using trace elements and U-Pb LA-ICPMS on complex zircons. (45 hp)
581. Pilser, Hannes, 2020: A geophysical survey in the Chocaya Basin in the central Valley of Cochabamba, Bolivia, using ERT and TEM. (45 hp)
582. Leopardi, Dino, 2020: Temporal and genetical constraints of the Cu-Co Vena-Dampetorp deposit, Bergslagen, Sweden. (45 hp)
583. Lagerstam Lorien, Clarence, 2020: Neck mobility versus mode of locomotion – in what way did neck length affect swimming performance among Mesozoic plesiosaurs (Reptilia, Sauropterygia)? (45 hp)
584. Davies, James, 2020: Geochronology of gneisses adjacent to the Mylonite Zone in southwestern Sweden: evidence of a tectonic window? (45 hp)
585. Foyn, Alex, 2020: Foreland evolution of Blåisen, Norway, over the course of an ablation season. (45 hp)
586. van Wees, Roos, 2020: Combining luminescence dating and sedimentary analysis to derive the landscape dynamics of the Velická Valley in the High Tatra Mountains, Slovakia. (45 hp)
587. Rettig, Lukas, 2020: Implications of a rapidly thinning ice-margin for annual moraine formation at Gornergletscher, Switzerland. (45 hp)
588. Bejarano Arias, Ingrid, 2020: Determination of depositional environment and luminescence dating of Pleistocene deposits in the Biely Váh valley, southern foothills of the Tatra Mountains, Slovakia. (45 hp)
589. Olla, Daniel, 2020: Petrografisk beskrivning av Prekambriska ortognejser i den undre delen av Särsvskollan, mellersta delen av Skollenheten, Kaledonska orogenen. (15 hp)
590. Friberg, Nils, 2020: Är den sydatlantiska magnetiska anomalien ett återkommande fenomen? (15 hp)
591. Brakebusch, Linus, 2020: Klimat och väder i Nordatlanten-regionen under det senaste årtusendet. (15 hp)
592. Boestam, Max, 2020: Stränder med erosion och ackumulation längs kuststräckan Trelleborg - Abbekås under perioden 2007-2018. (15 hp)
593. Agudelo Motta, Catalina, 2020: Methods for rockfall risk assessment and estimation of runout zones: A case study in Gothenburg, SW Sweden. (45 hp)
594. Johansson, Jonna, 2020: Potentiella nedslagskratrar i Sverige med fokus på Östersjön och östkusten. (15 hp)
595. Haag, Vendela, 2020: Studying magmatic systems through chemical analyses on clinopyroxene - a look into the history of the Teno ankaramites, Tenerife. (45 hp)



LUNDS UNIVERSITET

Geologiska institutionen
Lunds universitet
Sölvegatan 12, 223 62 Lund